

**STUDIES ON ATMOSPHERIC PLASMA SPRAYED
Mn_{1.0}Co_{1.9}Fe_{0.1}O₄ COATING ON CROFER 22 APU
INTERCONNECT FOR SOLID OXIDE FUEL
CELLS APPLICATIONS**

THESIS

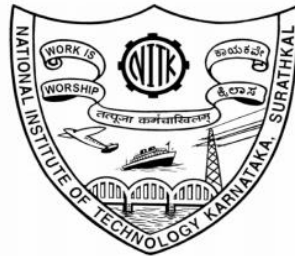
Submitted in partial fulfilment of the requirements for the degree of

DOCTOR OF PHILOSOPHY

by

MANJUNATH

(197059MT004)



**DEPARTMENT OF METALLURGICAL AND MATERIALS
ENGINEERING**

**NATIONAL INSTITUTE OF TECHNOLOGY KARNATAKA,
SURATHKAL, MANGALURU – 575025**

APRIL 2023

**STUDIES ON ATMOSPHERIC PLASMA SPRAYED $Mn_{1.0}Co_{1.9}Fe_{0.1}O_4$
COATING ON CROFER 22 APU INTERCONNECT FOR
SOLID OXIDE FUEL CELLS APPLICATIONS**

THESIS

Submitted in partial fulfilment of the requirements for the degree of

DOCTOR OF PHILOSOPHY

by

MANJUNATH

(197059MT004)

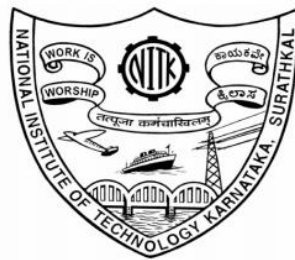
Under the guidance of

Dr. B. Rajasekaran

Assistant Professor

Dept. of Metallurgical and Materials Engineering

NITK Surathkal



**DEPARTMENT OF METALLURGICAL AND MATERIALS
ENGINEERING**

**NATIONAL INSTITUTE OF TECHNOLOGY KARNATAKA
SURATHKAL, MANGALURU – 575025**

DECLARATION

I hereby declare that the Research Thesis entitled “**Studies on atmospheric plasma sprayed $Mn_{1.0}Co_{1.9}Fe_{0.1}O_4$ coating on Crofer 22 APU interconnect for solid oxide fuel cells applications**” which is being submitted to the **National Institute of Technology Karnataka, Surathkal** in partial fulfilment of the requirements for the award of the **Degree of Doctor of Philosophy in Metallurgical and Materials Engineering**, is a bonafide report of the research work carried out by me. The material contained in this Research Synopsis has not been submitted to any other universities for the award of any degree.

Registration Number: **197059MT004**

Name of the Research Scholar: **Manjunath**

Signature of the Research Scholar:



Department of Metallurgical and Materials Engineering

Place: **NITK-Surathkal**

Date: **03-05-2023**

CERTIFICATE

This is to certify that the Research Thesis titled “**Studies on atmospheric plasma sprayed $Mn_{1.0}Co_{1.9}Fe_{0.1}O_4$ coating on Crofer 22 APU interconnect for solid oxide fuel cells applications**” submitted by **Mr. Manjunath (Registration Number: 197059MT004)** as the record of the research work carried out by him, is accepted as the Research Thesis submission in partial fulfilment of the requirements for the award of the **Degree of Doctor of Philosophy**.



Research Guide

Dr. B. Rajasekaran

Assistant Professor



Chairman-DRPC

Department of Metallurgical and
Materials Engineering

Date: **03-05-2023**

Chairman - DRPC
Dept. of Metallurgical and Materials Engineering
National Institute of Technology Karnataka, Surathkal
Post Srinivasnagar, Mangaluru - 575 025
Karnataka, India

ACKNOWLEDGEMENTS

I want to thank everyone who has contributed in part to this thesis. First and foremost, I would like to thank my respected teacher and research supervisor, **Dr. B. Rajasekaran**, Assistant Professor, Department of Metallurgical and Materials Engineering, NITK, whose worthy guidance and professional expertise have helped me complete this dissertation. His passion for quality experimental work and constant supervision in scientific writing has set the bar high at this level of my educational career.

I would also like to express sincere gratitude to **Prof. Dr. Robert Vassen**, Deputy Director, and colleagues in IEK-1: Materials Synthesis and Processing, Institute of Energy and Climate Research, Forschungszentrum, Jülich, GERMANY, for support and sharing the MCF coating Crofer 22 APU samples.

A special thanks to my HOD, **Dr. Ravishankar K S**, who always provided financial support and required facilities to successfully carry out all the research work. I would also like to thank **Dr. Jagannathan T K** for reviewing all my progress and providing valuable input. I sincerely thank **Dr. Sumanth Govindarajan** for providing his laboratory facilities whenever required for completing my work. I would also like to thank **Dr. K. Santhy**, Indus University, for her contribution to DFT and Thermocalc simulation and her help in the discussion for publications.

Thanks to my research group for contributing and inspiring me in many ways. I would also thank all the staff, lab technicians, and equipment operators for all the help in different ways over the years in completing my project.

Last but not least, I would like to thank my parents for always supporting and encouraging me in all my choices for my career. To my wife, Archana, it isn't easy to say how grateful I am to you. Without the support and sacrifices that you made, completing this thesis would not have been possible.

In the last three and half years of my Ph.D. journey, I have learned that achieving this work is by no means a one-person venture, and I owe it to my research supervisor, my parents, and my supporting wife.

ABSTRACT

Atmospheric plasma sprayed (APS) $\text{Mn}_{1.0}\text{Co}_{1.9}\text{Fe}_{0.1}\text{O}_4$ (MCF) coating is regarded as one of the excellent materials in mitigating Cr-evaporation in Crofer 22 APU ferritic stainless steel during high-temperature operation ($> 600\text{ }^\circ\text{C}$) in solid oxide fuel cell (SOFC) conditions. The aim of the present study is to characterize the structural integrity using a correlative scratch indentation test, physio-thermal integrity using in-situ high temperature X-ray diffraction (HT-XRD), and thermal integrity using a long-term thermal oxidation test of MCF coated Crofer steel for SOFC applications.

A network of micro-cracks and globular pores were seen in the cross-section analysis. The porosity of the as-sprayed MCF coating was $10.93 \pm 1.323\%$. XRD data revealed α -Fe as the major phase in as-received Crofer steel and CoO as the major phase in MCF coating. The micro-hardness measurements revealed strong metallic interlocking between the coating and substrate. The adhesion strength of MCF coating deposited on Crofer 22 APU ferritic steel was found to be in the range between 30 to 36 N, evaluated by scratch indentation test under progressive and constant loading conditions.

Initial stage oxidation of Crofer 22 APU steel carried out in an in-situ HT-XRD stage at $950\text{ }^\circ\text{C}$ and subsequent GD-OES characterization revealed the formation of two-layer oxides: Top layer spinel MnCr_2O_4 and fine-grained inner layer Cr_2O_3 . The Cr_2O_3 formed initially led to the formation of MnCr_2O_4 spinel during the initial stage. The rapid diffusion of Mn through the fine-grained Cr_2O_3 layer results in an increased growth rate of MnCr_2O_4 spinel on the top of the fine-grained Cr_2O_3 layer.

The thermal expansion mismatch of MCF coated Crofer steel interconnect has been investigated by in-situ HT-XRD from $25\text{-}900\text{ }^\circ\text{C}$. The results showed that the coefficient of thermal expansion of MCF coating was slightly higher than the steel substrate and showed no considerable thermal expansion mismatch as a function of temperature. The increase in lattice strain indicated the strain-induced phase transformation of MCF coating, supporting the phase transformation-induced self-healing phenomenon of MCF coating.

The oxidation kinetics of plasma sprayed MCF spinel coating on the Crofer 22 APU substrate at $850\text{ }^\circ\text{C}$ revealed phase transformation-induced crack healing and densification of the coating. MCF coating effectively acts as a Cr diffusion barrier and alters the kinetics of the two-layer oxide scale of the substrate. The UV-vis-NIR affirmed the reduction in band gap energy of the MCF coating, a beneficial effect to sustain the electrical conductivity at high temperatures.

CONTENTS

1. INTRODUCTION.....	1
1.1. Working principle of solid oxide fuel cell (SOFC).....	1
1.2. Role of interconnects	4
2. LITERATURE SURVEY	13
2.1. Basics of thermal spray coating	14
2.2. Thermal spray coating processes and techniques.....	15
2.3. Plasma arc (air or atmosphere).....	15
2.4. Comparison of coating techniques	16
2.5. Cross-section of thermally sprayed layer	17
2.6. Bonding mechanisms	18
2.7. MCF coating obtained by air plasma spray (APS) coating process.....	18
2.8. Various interconnect materials and coatings	24
2.9. Area-specific resistance	29
2.10. The adhesion strength of MCF coating.....	29
2.11. Early-stage oxidation of Crofer 22 APU steel	30
2.12. Thermal expansion induced thermal mismatch of MCF coated Crofer 22 APU metallic interconnect	32
2.13. Effect of MCF coating on the oxidation resistance of Crofer 22 APU steel	34
3. SCOPE AND OBJECTIVES OF PRESENT WORK	37
3.1. Research gap	37
3.2. Proposed objectives.....	38
4. MATERIALS AND METHODS	39
4.1. Materials and coating process	40
4.2. Methodology	40
4.2.1. Characterization of MCF coating on Crofer 22 APU steel.....	40
4.2.2. Scratch adhesion testing.....	41
4.2.3. Early oxidation of Crofer 22 APU steel.....	42
4.2.4. Thermal expansion mismatch of MCF coated Crofer 22 APU metallic interconnect	43

4.2.5. Long-term oxidation and characterization of oxidized specimens	44
5. RESULTS AND DISCUSSION	47
5.1. Characterization of plasma sprayed $Mn_{1.0}Co_{1.9}Fe_{0.1}O_4$ coating on Crofer 22 APU ferritic stainless steel used for solid oxide fuel cell interconnect.....	47
5.1.1. FESEM and XRD analysis.....	47
5.1.2. Micro-hardness	51
5.1.3. Resistance of as-sprayed MCF coating as a function of temperature.....	52
5.2. Mechanical integrity of the $Mn_{1.0}Co_{1.9}Fe_{0.1}O_4$ coating using scratch indentation testing	54
5.2.1. Surface analysis of as-deposited MCF coating using a 3D non-contact profilometer.....	54
5.2.2. Scratch test.....	56
5.2.3. Post-test failure analysis by FESEM.....	59
5.2.4. 3D noncontact profilometer analysis	62
5.3. Early oxidation of Crofer 22 APU steel.....	63
5.3.1. Surface morphology under scanning electron microscope (SEM)	63
5.3.2. X-Ray diffraction.....	64
5.3.3. Atomic force microscopy (AFM)	66
5.3.4. Raman spectroscopy	68
5.3.5. Glow discharge optical emission spectroscopy (GD-OES).....	69
5.4. Thermal expansion induced thermal mismatch of $Mn_{1.0}Co_{1.9}Fe_{0.1}O_4$ coated Crofer 22 APU metallic interconnect used for SOFC – an experimental approach using in-situ high temperature X-ray diffraction	72
5.4.1. Phase analysis and thermal expansion mismatch.....	72
5.4.2. Discussions	78
5.5. Effect of plasma sprayed $Mn_{1.0}Co_{1.9}Fe_{0.1}O_4$ protective coating on the oxidation resistance of Crofer 22 APU SOFC interconnect.....	82
5.5.1. Microstructure analysis.....	82
5.5.2. GDOES depth profiling of oxidized Crofer substrate.....	87
5.5.3. X-ray diffraction	89
5.5.4. Raman spectroscopy	92
5.5.5. Optical analysis of MCF coating using UV-vis-NIR.....	93
5.5.6. Oxidation kinetics	94

5.5.7. Discussion.....	97
5.5.7.2 Effect of MCF coating on the oxidation resistance of Crofer 22 APU.....	100
6. CONCLUSIONS.....	105
6.1. Scope for future work	106
REFERENCES	107

LIST OF FIGURES

Figure 1: Working Principle of SOFC (Mah et al. 2017)	2
Figure 2 (a) Schematic configuration of a planar SOFC stack (b) schematic cross-section showing means of contact between interconnect and electrodes (Singheiser et al. 2010) ..	3
Figure 3: Monolithic Design SOFC (Yamamoto 2000)	4
Figure 4: Tubular Design SOFC (Singhal 2000)	4
Figure 5 Schematic diagram of Cr-poisoning in SOFC (Wu and Liu 2010).....	9
Figure 6: Representation of a Three-Phase Boundary (TPB) (Bastidas 2006).....	10
Figure 7: (a) Wire or Rod type, (b) Powder type thermal spraying (Davis 2004).....	13
Figure 8: Basics of Thermal Spraying (Espallargas 2015)	14
Figure 9: Thermal Spray Coating Techniques (Davis 2004)	15
Figure 10: Plasma Arc Thermal Spray Process (Singhal 2000)	16
Figure 11: Comparison of different coating techniques (Espallargas 2015).	17
Figure 12: Schematic cross section of thermally sprayed layer (Kandeva-Ivanova et al. 2016)	17
Figure 13: Bonding Mechanisms (Kandeva-Ivanova et al. 2016)	18
Figure 14: Schematic drawing of crack-healing process. Annealing of as sprayed APS-MCF in air, the MeO (Me = $Mn_{1.0}Co_{1.9}Fe_{0.1}$) rock salt phase is transformed into the spinel configuration Me_3O_4 . This results in volume expansion, which takes place at the MCF surfaces (c). Oxygen cannot penetrate to the bulk over the gas phase after the cracks are closed (d) (Grünwald et al. 2017).	22
Figure 15: Phase relations in the system cobalt oxide - manganese oxide in air (Aukrust and Muan 1963)	23
Figure 16: Flow chart showing the proposed methodology.....	39
Figure 17: (a) Macro image of MCF coating on Crofer 22 APU steel interconnect with rectangular gas flow channels, (b), (c) Surface morphology of coating, (d), (e), (f) cross-section image of the MCF-coated Crofer steel at different magnifications.	47
Figure 18: EDS spot and area analysis of a cross-section of MCF-coated Crofer steel ...	49
Figure 19: XRD patterns of as-received Crofer 22 APU steel (top) and as-sprayed MCF coating (bottom).....	50
Figure 20: Schematic showing locations for micro-hardness measurements	51
Figure 21: Graph of resistance of as-sprayed MCF coating as a function of temperature	52
Figure 22: 3D profile of the specimen displaying the surface of the ridges and grooves..	54

Figure 23: (a) Surface profile of coating depicting depth characteristics, (b) Primary surface profile in 3D for estimating average surface roughness55

Figure 24: Coating analysis area using a confocal profilometer, (a) selected area of the investigated coating for measuring surface roughness, (b) photo simulation of the coated surface, (c) 3D view of the selected coating area showing variation in roughness55

Figure 25: (a) Scratch curve plotted for progressive scratch testing, (b) Acoustic Emission v/s Normal Load (dotted red rectangular box indicating failure of coating)57

Figure 26: Scratch curves of constant loads, (a) 20 N, (b) 30 N, (d) 40 N, (c) Acoustic Emission vs. Stroke (dotted red rectangular box indicating failure of coating)59

Figure 27: FE-SEM image of progressive load scratch (a) Image covering the overall scratch length (b) magnified image of the area of failure (c) magnified image of the cracks formed before failure 60

Figure 28: FE-SEM images of constant load scratch (a) 20 N, (b) 30 N, (c) magnified image of 30 N at the area of failure, (d) 40 N.....61

Figure 29: (a) Confocal profilometer images of progressive load scratch test (a) and constant load test (b) 20N, (c) 30N, (d) 40N62

Figure 30: Surface morphology of Crofer 22 APU steel (a) before in-situ oxidation (b) after in-situ oxidation63

Figure 31: X-Ray Diffraction pattern of Crofer 22 APU (a) before oxidation at room temperature (b) at 950 °C in-situ oxidation (c) after in-situ oxidation at room temperature (d) GIXRD after in-situ oxidation.....64

Figure 32: AFM images of Crofer 22 APU before in-situ oxidation (a) 2D image, (b) 3D image, (c) line profile 1, (d) line profile 2, (e) roughness profile across line 1, (f) roughness profile across line 2.....66

Figure 33: AFM images of Crofer 22 APU after in-situ oxidation (a) 2D image, (b) 3D image (red dotted line indicated high structures), (c) line profile 1, (d) line profile 2, (e) roughness profile across line 1, (f) roughness profile across line 2.....67

Figure 34: Confocal Raman Spectra of Crofer 22 APU after in-situ oxidation.....68

Figure 35: Depth Profile elemental composition by GD-OES (a) before oxidation (b & c) magnified view (d) after oxidation (e & f) magnified view, (line 1 – the intersection of all elements with O, line 2 – the intersection of elements with O, line 3 – the intersection of Cr with O, dotted square – enrichment of Ti) 70

Figure 36: In-situ high-temperature XRD stack (a) Crofer 22 APU (b) MCF coating.....72

Figure 37: Peak shift after in-situ (a) Crofer 22 APU (b) MCF coating.....74

Figure 38: Crystallite size & lattice strain vs. temperature, Scherrer Equation - (a) Crofer 22 APU, (b) MCF, Williamson-Hall Plot - (c) Crofer 22 APU, (d) MCF.....	78
Figure 39: Variation of Lattice Parameter vs. Temperature (a), Coefficient of Thermal Expansion (CTE) (α) vs. temperature (b), Thermal mismatch between Crofer steel and MCF coating upon heating from room temperature (c), Thermal stress vs. temperature $T_d = 0$ & (d) $T_d = 200$ °C (e).....	80
Figure 40: FE-SEM analysis after 50 h oxidation at 850 °C of Crofer 22 APU and MCF coating respectively, (a), (e) surface morphology, (b), (f) back scattered cross-section, (c), (g) elemental mapping, (d), (h) line scan.....	84
Figure 41: FE-SEM analysis after 200 h oxidation at 850 °C of Crofer 22 APU and MCF coating respectively, (a), (e) surface morphology, (b), (f) back scattered cross-section, (c), (g) elemental mapping, (d), (h) line scan.....	85
Figure 42: FE-SEM analysis after 400 h oxidation at 850 °C of Crofer 22 APU and MCF coating respectively, (a), (e) surface morphology, (b), (f) back scattered cross-section, (c), (g) elemental mapping, (d), (h) line scan.....	86
Figure 43: GD-OES depth profiles of Crofer 22 APU, (a) & (b) after 50 h, (c) & (d) after 200 h, (e) & (f) after 400 h [lines A, B, C, D, E, F represents the oxide layer thickness].	88
Figure 44: XRD of (a) Crofer 22 APU (b) MCF coating after oxidation at 850 °C.....	90
Figure 45: Raman Spectra of (a) Crofer 22 APU (b) MCF coating after oxidation	92
Figure 46: UV-vis-NIR absorbance spectra MCF coating after oxidation at 850 °C mentioning the band gap energy	94
Figure 47: Oxidation kinetics of the MCF-coated Crofer 22 APU composite oxidized at 850 °C in air.....	95
Figure 48: Graphs depicting (a) oxide layer thickness v/s oxidation time and, (b) Oxide growth kinetics v/s oxidation time.....	96
Figure 49: GD-OES Cr-concentration profiles of Crofer 22 APU from the surface after oxidation at 850 °C in air.....	98
Figure 50: Proposed mechanism of two-layer oxide formation during oxidation in uncoated Crofer steel.....	100
Figure 51: Proposed mechanism of oxidation in MCF-coated Crofer steel	102

LIST OF TABLES

Table 1: Composition of Crofer 22 APU	40
Table 2: Testing conditions of progressive load scratch test	41
Table 3: Testing conditions of constant load scratch test	42
Table 4: EDS spot and area analysis from Fig. 18.....	49
Table 5: Lattice parameter, crystallite size, and micro-strain of as-received Crofer 22 APU steel and as-sprayed MCF coating	50
Table 6: Hardness values of Crofer 22 APU, coating-substrate interface, and MCF coating in as-sprayed conditions.....	52
Table 7: Surface profile parameters obtained from a 3D noncontact profilometer before the scratch test.....	56
Table 8: Area EDS data of Crofer steel before and after in-situ oxidation.....	64
Table 9: Crystallite size of Oxides from GIXRD	65
Table 10: Roughness values of Crofer 22 APU from AFM	68
Table 11: Lattice Parameter, Crystallite size, and Coefficient of thermal expansion (CTE) of Crofer 22 APU after in-situ oxidation	75
Table 12: Lattice Parameter, Crystallite size, and Coefficient of thermal expansion (CTE) of MCF coated steel after in-situ oxidation	76
Table 13: Thermal stress between Crofer 22 APU and MCF, Thermal expansion mismatch (%) between Crofer steel and MCF coating upon heating from room temperature in MCF coated Crofer steel	77
Table 14: EDS analysis results of Crofer steel and MCF coating after oxidation at 850 °C as shown in Figures 40, 41 and 42.....	87
Table 15: Results of Rietveld Refinement made on the XRD patterns of Crofer 22 APU shown in Fig. 44a.....	91
Table 16: Results of Rietveld Refinement made on the XRD patterns of MCF coating shown in Fig. 44b.....	91
Table 17: Crystallite size variation with oxidation time at 850 °C.....	91
Table 18: Raman spectra observed on the Crofer 22 APU and MCF coating after oxidation for 50, 200, and 400 h at 850 °C.....	93
Table 19: Change in oxide layer thickness and growth kinetics with oxidation time	96
Table 20: Energy of formation of oxides at 0 K and 1200 K	97

NOMENCLATURE

SOFC – Solid Oxide Fuel Cell

APS – Atmospheric/Air Plasma Spray

MCF - $\text{Mn}_{1.0}\text{Co}_{1.9}\text{Fe}_{0.1}\text{O}_4$

YSZ – Yttria Stabilized Zirconia

LSM – Lanthanum Strontium Manganite (LaSrMnO_3)

LSCF - Lanthanum Strontium Cobalt Ferrite ($\text{La}_x\text{Sr}_{1-x}\text{Co}_y\text{Fe}_{1-y}\text{O}_3$)

ASR – Area Specific Resistance

FE-SEM – Field Emission Scanning Electron Microscope

COF – Coefficient of Friction

AFM – Atomic Force Microscopy

GIXRD – Grazing Incidence X-Ray Diffraction

GD-OES – Glow Discharge Optical Emission Spectroscopy

DFT – Density Functional Theory

1. INTRODUCTION

Fuel cells are all solid devices which generate electricity by an electrochemical reaction between the fuel and an oxidant. Because of its low emissions, flexible fuel, and higher efficiency than traditional energy-conversion systems, solid oxide fuel cell (SOFC) technology is gaining popularity as a power generation method. Stationary power production unit, auxiliary power units (APU), and military requirements are among the major applications for SOFCs. SOFCs are designed for stationary high-power generation (100 kW up to megawatt), small-power system applications (1-20 kW), and portable electronic devices (20-250 W) (Bianco et al. 2017; Hui et al. 2007; Mah et al. 2017; Niewolak et al. 2016; Singheiser et al. 2010; Wu and Liu 2010).

The basic mechanism of SOFC is the potential difference between the anode and cathode, caused by fuel oxidation at the anode and the oxygen reduction reaction at the cathode. The reaction compounds are H₂O and CO₂, and due to polarization and ohmic losses, the chemical energy of the reaction is released as electricity and heat (Singheiser et al. 2010). High-temperature SOFCs can provide clean, pollution-free technology for electrochemically producing electricity at high conversion efficiency. (Wu and Liu 2010). A single cell of SOFC stack comprises an anode, cathode, and electrolyte. A solid, non-porous ceramic, generally Y₂O₃-stabilized ZrO₂ (YSZ), is used as an electrolyte. The operating temperature of a SOFC is 600–1000 °C, which enables the conductive nature of the ceramic electrolyte to oxygen, but non-conductive to electrons. The advantage of high working temperatures is in reducing polarisation losses and the effects of fuel impurity tolerance. The anode is made of Nickel/yttria-stabilized zirconia (Ni/YSZ) cermet, and the cathode is electronically conductive perovskite Sr-doped LaMnO₃ (LSM) or other perovskite materials (Bianco et al. 2017; Hui et al. 2007; Niewolak et al. 2016; Singheiser et al. 2010; Wu and Liu 2010). These SOFCs have numerous advantages over conventional energy-conversion systems, including high efficiency, dependability, modularity, fuel adaptability, and extremely low NO_x and SO_x emissions. SOFCs' quiet, vibration-free operation eliminates the noise generally associated with conventional power-generation systems (Singhal 2000).

1.1. Working principle of solid oxide fuel cell (SOFC)

SOFCs consist of two porous electrodes separated by a dense, oxygen-ion-conducting electrolyte. Fuels, specifically hydrogen, is supplied to the anode and oxidized to liberate

electrons. Oxygen used as an oxidant is supplied to the cathode and reduced to oxygen ions. The O_2 ions pass through the electrolyte at the anode and react with hydrogen forming water. The liberated electrons will move through an external circuit, known as interconnects, to generate electricity. The difference in oxygen partial pressure between the anode and the cathode is the driving force for oxygen diffusion through the dense electrolyte (Bianco et al. 2017; Hui et al. 2007; Mah et al. 2017; Niewolak et al. 2016; Singheiser et al. 2010; Wu and Liu 2010).

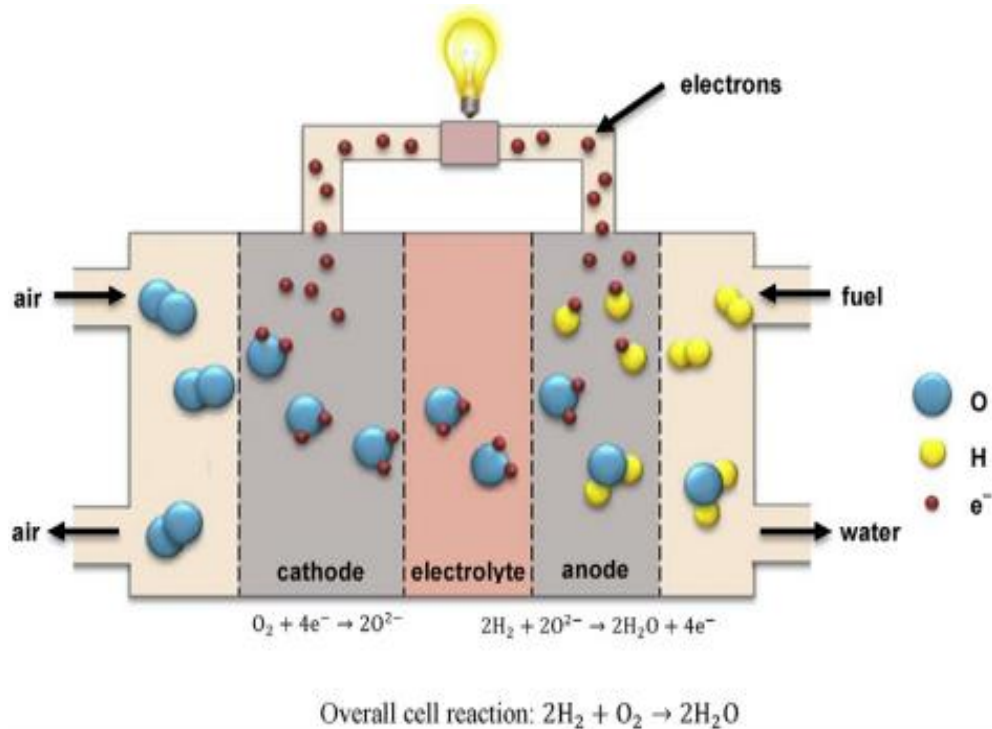


Figure 1: Working Principle of SOFC (Mah et al. 2017)

SOFCs of several different designs have been investigated; these include planar, monolithic, and tubular geometries.

The planar design configures the cell components as thin, flat plates. The interconnection, ribbed on both sides, forms gas-flow channels and serves as a bipolar gas separator contacting the anode and the cathode of adjoining cells (Niewolak et al. 2016; Singhal 2000). The dense electrolyte and interconnection are fabricated by tape casting, powder sintering, or chemical vapor deposition (CVD), whereas slurry methods, screen printing, or plasma spraying apply the porous electrodes. The planar cell design offers high power density but requires high-temperature gas seals at the edges of the plates to isolate the oxidant from the fuel (Bianco et al. 2019; Niewolak et al. 2016; Singhal 2000; Yamamoto 2000).

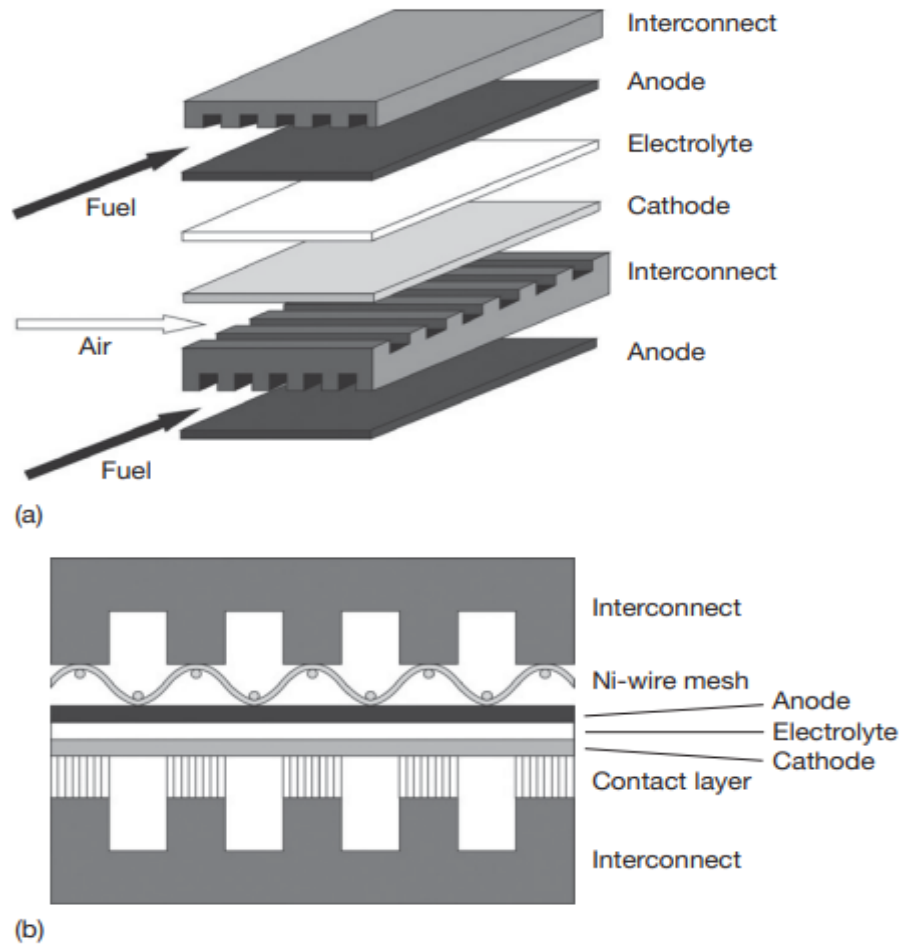


Figure 2 (a) Schematic configuration of a planar SOFC stack (b) schematic cross-section showing means of contact between interconnect and electrodes (Singheiser et al. 2010)

In the monolithic design, the different cell components are fabricated as thin layers. In the co-flow monolithic SOFC, the cell comprises a honeycomb-like array of adjacent fuel and oxidant channels. Such a cell consists of two laminated structures: anode/electrolyte/cathode and anode/interconnect/cathode. The anode/ electrolyte/cathode composite is corrugated and stacked alternately between flat anode/interconnect/cathode composites (Niewolak et al. 2016; Singhal 2000; Yamamoto 2000).

In tubular design, the cell components are deposited as thin layers on a ceramic cathode (air electrode) tube. Each tube is manufactured like a large test tube, sealed at one end. The fuel flows along the outside of the tube towards the open end. Air is fed through a thin alumina air supply tube located centrally inside each tubular fuel cell. The heat generated within the cell brings the air up to the operating temperature. Then the airflow is channeled through the fuel cell back up to the open end. One significant advantage of the tubular SOFC design is the elimination of high-temperature gas-tight seals (Niewolak et al. 2016; Singhal 2000; Yamamoto 2000).

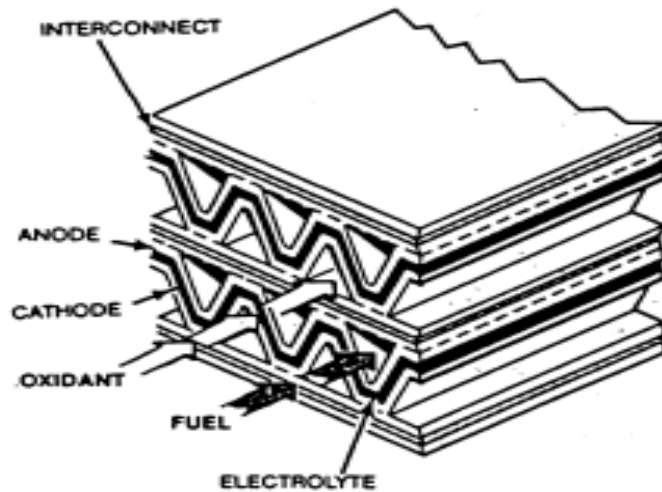


Figure 3: Monolithic Design SOFC (Yamamoto 2000)

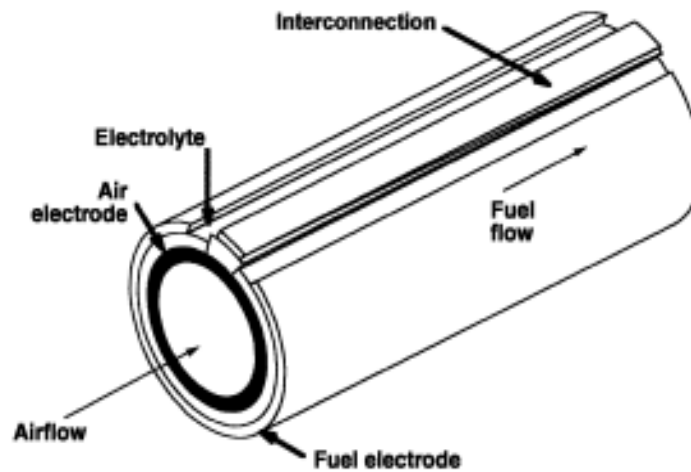


Figure 4: Tubular Design SOFC (Singhal 2000)

In comparison to tubular cells, the anode-supported planar SOFCs have higher power densities and lower fabrication costs. The interconnect materials are selected based on different conditions. The materials must exhibit the following (Singhal 2000):

- a. Electrical conductive properties which allow the cells to function without losses incurred.
- b. Good chemical and structural stability at high temperatures
- c. Reactivity and inter-diffusion among different cell components should be minimized.
- d. Thermal expansion coefficients should match the other elements of the cell.

1.2. Role of interconnects

An essential part of the SOFC stack is the interconnect, which segregates the fuel at the anode from the air or oxygen at the cathode and offers an electrical network between

independent cell stacks. Hence, the interconnect material must effectively conduct electricity, be stable in oxidizing and reducing environments, and have a thermal expansion coefficient that complements other components of SOFC. (Wang et al. 2011).

SOFCs are not operated as single units but as an array of units or “stack,” with interconnects joining the anodes and cathodes of adjacent units. Interconnects provide an electrical connection between the anode of one individual cell to the cathode of the neighboring one and act as a physical barrier to avoid any contact between the reducing and the oxidizing atmospheres (Bianco et al., 2017; Hui et al., 2007; Niewolak et al. 2016; Singheiser et al. 2010; Wu and Liu 2010).

In general terms, the interconnect has to meet the following demands (Bastidas 2006; Niewolak et al. 2016; Singheiser et al. 2010; Wu and Liu 2010):

- Excellent electrical conductivity: Suitable area-specific resistance (ASR) $< 0.1 \Omega\text{cm}^2$
- Excellent oxidation resistance in air and $\text{H}_2/\text{H}_2\text{O}$ atmosphere
- Excellent imperviousness for oxygen and hydrogen to prevent the direct combination of oxidant and fuel during operation
- Coefficient of thermal expansion (CTE) matching those of electrodes and electrolyte, around $10.5 \times 10^{-6} \text{ K}^{-1}$ at 25°C - 1000°C , in order to reduce the thermal stresses created during start-up and shutdown
- Good thermal conductivity (minimum value of $5 \text{ Wm}^{-1}\text{K}^{-1}$)
- No reaction or inter-diffusion between interconnect and its adjoining components
- Adequate strength and creep resistance at elevated temperatures
- Low cost, as well as ease of fabrication and shaping

The formation of the Cr_2O_3 scale on the steel surface provides corrosion protection. At high temperatures, chromium oxide has a low electrical resistivity ($1 \times 10^2 \Omega/\text{cm}$ at 800°C). The corrosion of SOFC interconnectors is similar to that of heat exchangers in gasifiers, where the metal temperatures are relatively high, and the gas has very low oxygen activity but high carbon and sulfur activities. Because the deposits on the metal surface are typically less aggressive, the environment is less severe (Horita 2021; Niewolak et al. 2016; Singheiser et al. 2010). For SOFC interconnect, corrosion and mechanical deformation are the most known degradation phenomena. Corrosion increases the electrical resistivity of the interconnect due to poorer electrical conductivity of the thermally grown oxide layer,

and the deformation of the interconnect potentially reduces the contact area with the cell (Bianco et al. 2017).

Lanthanum Chromite (LaCrO_3) was the conventional material used for the high-temperature ($\sim 1000^\circ\text{C}$) SOFC interconnect applications. Compared to typical ceramics, this material exhibits an exceptionally high electric conductivity when used in SOFCs, and the enhancement in the conductivity can be achieved by doping with Mg, Sr, or Ca. The melting point of LaCrO_3 is $2783 \pm 20 \text{ K}$ (Zhuiykov 2018). The material stability was seen in both the cathode and anode environments. The average coefficient of thermal expansion (CTE) of LaCrO_3 is $9.5 \times 10^{-6} \text{ K}^{-1}$, which is rather close to the CTE of YSZ ($10.5 \times 10^{-6} \text{ K}^{-1}$) (Niewolak et al. 2016; Singheiser et al. 2010; Wu and Liu 2010).

Doped lanthanum chromites (LaCrO_3) were chosen for high-temperature SOFCs (about 1000°C). LaCrO_3 shows excellent electrical conductivity, stability under both reducing and oxidizing atmospheres, and a compatible thermal expansion coefficient (TEC) match to adjacent material (Mah et al. 2017). LaCrO_3 , a p-type semiconductor, becomes oxygen deficient with decreasing oxygen partial pressure, which results in reduced conductivity. Lanthanum is also expensive as it is a rare-earth element (Wu and Liu 2010).

At a high temperature of $900\text{-}1000^\circ\text{C}$, chromium-based oxide dispersion strengthened (ODS) alloys were mainly used to replace LaCrO_3 . Cr-based oxide dispersed strengthened alloy, particularly Ducrolloy ($\text{Cr-5Fe-1Y}_2\text{O}_3$, designed by Plansee Company), can replace LaCrO_3 for SOFCs operating nearly around 1000°C (Mah et al. 2017). Ducrolloy shows exceptional oxidation resistance and excellent TEC compatibility with other SOFC components. Due to the good conductin behavior of chromia compared to other oxides, chromia-forming alloys are highly preferred. But the limitation lies in chromium poisoning of the cathode due to unavoidable excessive chromia growth in high Cr-containing alloys. After thermal cycles, an excessively grown chromia layer will lead to spallation and produce an unacceptably high area-specific resistance (ASR) after oxidation at 1000°C for 75 h (Wu and Liu 2010).

The substrate alloy needs to contain enough Cr to produce a continuous chromia layer. According to a literature summary, a protective, continuous chromia scale is formed with a minimum of 20-25 wt.% Cr in the alloy. Using alloys with a Cr content of 5-10 wt.%) in interconnect has reduced the oxidation resistance remarkably (Zhuiykov 2018). Very low chromium (<5 wt.%), regarded as almost pure Fe oxide, contained internal oxide

precipitates of Cr_2O_3 and/or FeCr_2O_4 spinels (Niewolak et al. 2016; Singheiser et al. 2010; Wu and Liu 2010).

Stainless steels are usually divided into four groups: (i) ferritic steels, (ii) austenitic steels, (iii) martensitic steels, and (iv) precipitation-hardening steels. Due to their body-centered cubic structure, which brings the CTE quite close to other SOFC materials, ferritic stainless steels are typically the most promising candidates among them for SOFC interconnect applications. But the effect of substrate impurities like Si and Al on the performance of the interconnect could not be neglected, especially silicon, which could form a continuous layer between substrate and scale. Interconnect will function in a reducing environment on the anode side of the SOFC stack and an oxidizing environment on the cathode side (Wu and Liu 2010).

The oxidation resistance and electrical conductivity of Ni-Cr-based alloys are significantly better. A 15 wt.% Cr is sufficient for forming a continuous chromia layer to resist hot corrosion, less than Fe-Cr-based alloys, where the optimal content was 18-19 wt.%. The potential CTE mismatch to cell components is the main issue with Ni-Cr-base alloys (Wu and Liu 2010).

Compared to ceramic interconnects, metallic interconnects have higher electrical and thermal conductivity, better mechanical strength, and manufacturability. A suitable metallic interconnects naturally forms a continuous scale of alumina (Al_2O_3) or chromia (Cr_2O_3) oxide layer, which prevents oxidation under SOFC working conditions. Hence, the insulating nature of Al_2O_3 scales is suited, which is observed in Cr-forming alloys. All Cr-containing alloys, including Cr, Fe-Cr, and Ni-Cr-based alloys, are considered probable metallic candidates (Mah et al. 2017).

Metallic materials can be used instead of LaCrO_3 as interconnects due to its improved advantages compared with its high-temperature counterpart:

- i. Metallic interconnects possess high mechanical strength. The interconnect not only guides the flow of fuel or air, but also provides mechanical support to the other components of cell stack in SOFC.
- ii. Metallic materials exhibit high thermal conductivity. The elimination of temperature gradient can be achieved both along the interconnect plane and across the components.
- iii. Metallic materials show high electronic conductivity, decreasing the cell's resistance and increasing output.

iv. Ease of production, reduced expenditure, and availability of material.

Ferritic stainless steels that form chromia are the most promising and widely used metallic alloys. When combined with significant growth stresses, the formation and growth of chromia scales, mainly in oxidizing environments, can induce porosity at the alloy-scale interface and result in scale cracking and spallation. Additionally, in the presence of oxygen or water, chromium-rich scales react to produce volatile chromium oxyhydroxides and oxides under SOFC operating conditions. At the cathode/electrolyte interface, volatile Cr species can accumulate and seriously impair cell performance. The vaporization of Cr species and the development of chromia scales are mitigated by coating the alloy surface with a protective coating.

The primary problems of metallic interconnect used in SOFC operated at high temperatures at around 850 °C are (Yang et al. 2017):

- Evaporation of chromium species and subsequent corrosion of steel, which reduces the lifespan of stacks
- Deposition of Cr (III)-species (CrO_3 , or $\text{Cr}(\text{OH})_2\text{O}_2$) in the functional layer of the cathode blocking the active sites, especially at the three-phase boundary (electrolyte-cathode-oxygen) and worsening cell performance
- Occurrence of buckling and oxide scale spalling from the interconnect due to exposure to thermal cycling

After thousands of hours of exposure to the SOFC environment at intermediate temperatures, an assessment of oxidation behavior shows that chromia layer on ferritic steels grow up to tens of micrometers. ASR would increase due to this scale growth, and stack performance would deteriorate as a result. Increase in the thermal stress in the coating-substrate interface will lead to spallation. The electrical properties of SOFC may significantly deteriorate due to chromium vaporization from the metallic interconnect. This has been observed by various groups at the cathode side of SOFC using Y_2O_3 -doped ZrO_2 as the solid electrolyte and LSM as the cathode, along with Cr_2O_3 -forming alloys as interconnects. The vaporization of Cr_2O_3 from interconnect surfaces as $\text{CrO}_3(\text{g})$ or $\text{CrO}_2(\text{OH})_2(\text{g})$ as major gaseous species with chromium in the 6+ oxidation state is the basis of the reaction. When the oxygen partial pressure is higher, the vapor pressure rises. When operating at temperatures between 800 and 1000 °C, the $\text{CrO}_2(\text{OH})_2(\text{g})$ exhibits the highest vapor pressure (Wu and Liu 2010).



The three-phase boundary (electrolyte/cathode/oxidant) will electrochemically or chemically reduce chromium-containing vapor species formed from the interconnect material. This form of poisoning is most likely to arise at the cathode because the vapor pressures in the air are higher. A reduction in cell voltage or a surge (i.e., more negative) in cell overvoltage can be used to illustrate this degradation. The schematic diagram of the Cr poisoning process is displayed below:

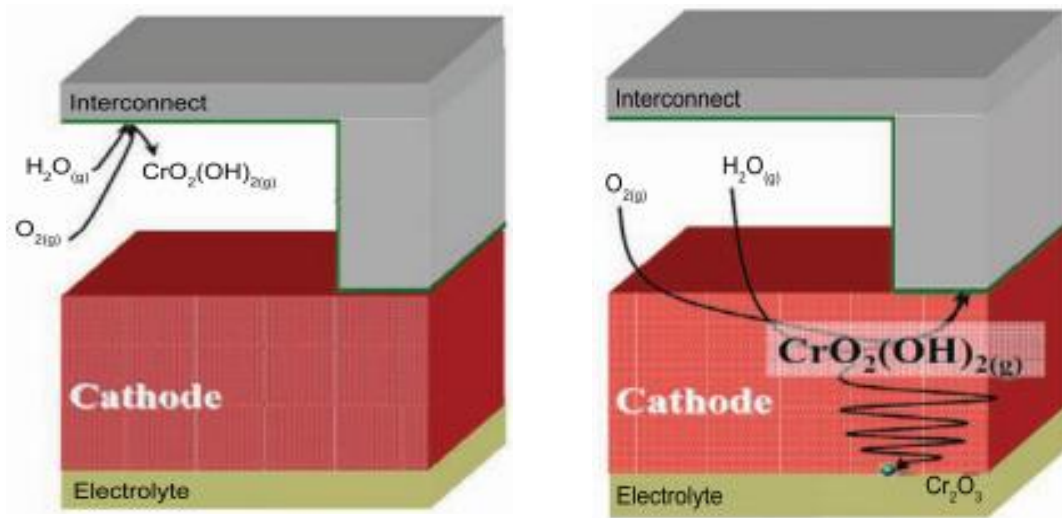
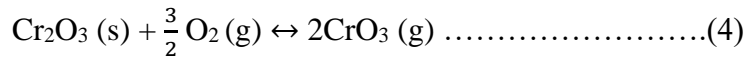
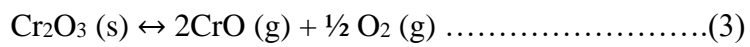
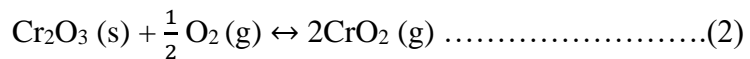
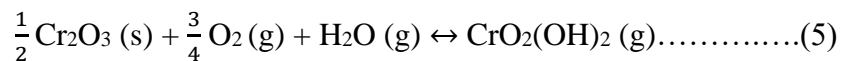


Figure 5 Schematic diagram of Cr-poisoning in SOFC (Wu and Liu 2010)

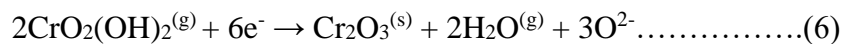
At high temperatures in dry air, the Cr₂O₃ surface scale present on Cr or Cr-based alloys evaporates according to the following reactions, forming volatile CrO, CrO₂, and CrO₃ (Machkova et al. 2008; Wu and Liu 2010; Yang et al. 2017):



It has been demonstrated through experimentation that the reaction that produces volatile CrO₂(OH)₂ in wet air by the reaction:



At the cathode–electrolyte interface, the oxyhydroxides react according to the:



Depending on the cathode side inlet atmosphere, using high chromium alloyed steels poses a risk of chromium trioxide (CrO_3) and chromium hydroxides ($\text{CrO}_2(\text{OH})_2$) formation and evaporating from the steel. The transport of CrO_3 and $\text{CrO}_2(\text{OH})_2$ occurs in the possible region of oxygen ionization, which is called as active cathode area (triple phase boundary, TPB). The reduction of the compounds to Cr_2O_3 diminishing the size of active region which reduces the efficiency of the SOFC stack (Bastidas 2006).

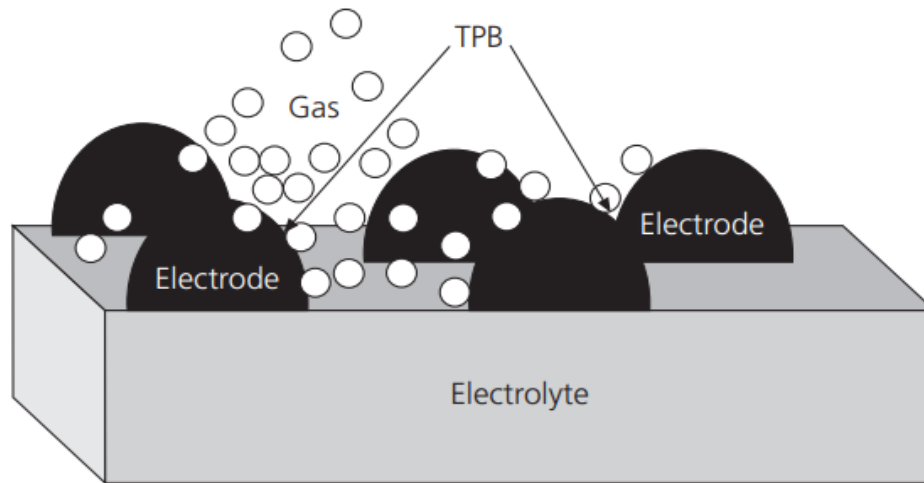


Figure 6: Representation of a Three-Phase Boundary (TPB) (Bastidas 2006)

The major disadvantage of these materials is the water vapor-induced Cr-evaporation from the chromia-containing scale formed on the ferritic steels at high temperatures under oxidative atmospheres. This evaporation leads to a poisoning of the cathode by either blocking active electrochemical sites by chromia deposition and further on reaction to chromium–manganese spinel (e.g., in the case of $\text{La}_{1-x}\text{Sr}_x\text{MnO}_{3-\delta}$ based cathodes (LSM)) or by secondary phase formation like Sr-chromate (e.g., in case of using $\text{La}_{1-x}\text{Sr}_x\text{Fe}_{1-y}\text{Co}_y\text{O}_{3-\delta}$ based cathodes (LSCF)) (Vaßen et al. 2016).

Surface modification is the most effective way to reduce Cr evaporation in the interconnect material. Thermal spray coatings have the best-achieved chromium retention in the metallic interconnect. The appropriate coatings must have adequate conductivity, match thermal expansion and chemical compatibility with adjacent components, and have good stability in reducing and oxidizing atmospheres. Reasons for Atmospheric plasma sprayed (APS) $\text{Mn}_{1.0}\text{Co}_{1.9}\text{Fe}_{0.1}\text{O}_4$ (MCF) coating is the best possible option to tackle the Cr evaporation (Grünwald et al. 2017):

- The chromium evaporation can be decreased by providing a chromium protection layer between the interconnect and cathode, reducing the cathode degradation.
- Atmospheric plasma sprayed (APS) $\text{Mn}_{1.0}\text{Co}_{1.9}\text{Fe}_{0.1}\text{O}_4$ (MCF) exhibited its long-term stability and low chromium poisoning within actual SOFC operation conditions.
- APS-MCF layers are relatively dense.
- APS-MCF coatings are favourable coating for chromium protection layers (it is assumed that maximum of the additional degradation is generated from contact between chromium and cathode).

2. LITERATURE SURVEY

Surface coating has been a reliable and inexpensive process for a very long time to secure the product from corrosion, wear resistance and erosion, and adhesion. A coating material is applied to a moving web of a flexible substrate during the coating process. The coating delivers enhanced aesthetic and physical properties to the substrate derived from the coating material. Surface coating is employed in numerous processes for producing materials, tools, and machine parts. Several surface coating methods can also be used for functional and decorative purposes, such as adhesion, corrosion, wear resistance, and erosion, or for both purposes to enhance the product's appeal (Davis 2004; Espallargas 2015).

Thermal spraying is an advanced materials processing method that has gained wide acceptance in many high-technology industries. In this process, the material is heated, melted, and sprayed into a high-temperature, high-velocity flame using either chemical or electrical energy. The feedstock injected into the flame is typically a powder, but it can also take the form of wire or rod. Thus, molten droplets are transported to an object to create overlay coatings for protection or performance purposes (Davis 2004; Espallargas 2015).

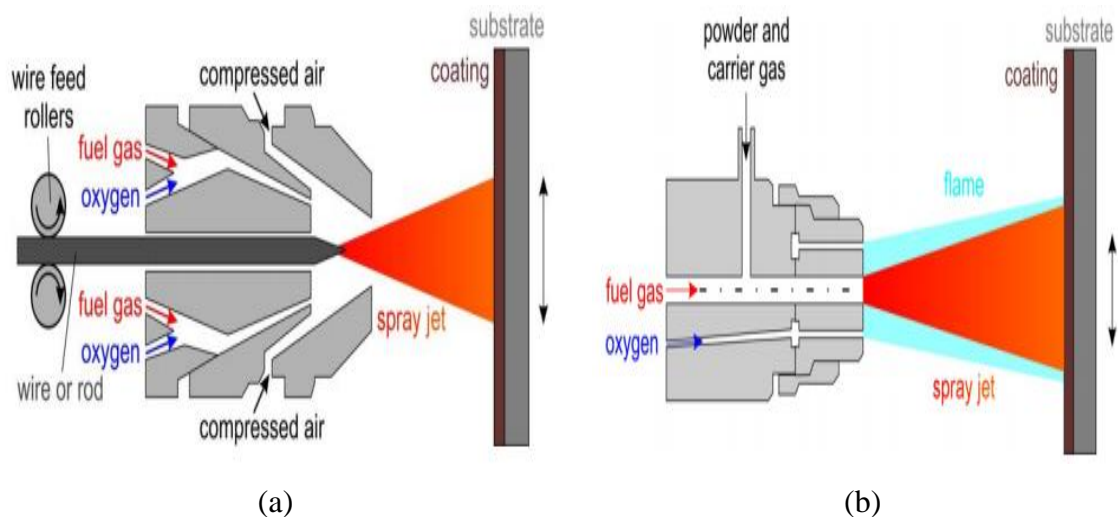


Figure 7: (a) Wire or Rod type, (b) Powder type thermal spraying (Davis 2004)

The performance of engineering materials and their surface properties are extensively improved by using thermal spray coatings as overlays. Fine molten or semi-molten particles are sprayed during the process onto substrates to generate a coating layer. The common processes include arc, flame, plasma, detonation spray, and high-velocity oxy-fuel spraying. The microstructure of coatings is composed of lamella structure and additional

characteristic features such as porosity and oxides. To create distinctive coating microstructures, various substrate materials can be coated with metals, alloys, metal oxides, metal/ceramic blends, carbides, wires, and rods. Thermal spray coatings provide a functional surface to protect or modify the behavior of substrate material and/or component (Davis 2004; Espallargas 2015).

Depending on the spraying process, the particle speed and size distribution, and the spray distance, thermal spray coatings may have varying porosity levels. Porosity may be beneficial in tribological applications through the retention of lubricating oil films. Porosity also is beneficial in coatings on biomedical implants. Due to the lubricity of some oxides, lamellar oxide layers may also result in reduced wear and friction. The porosity of thermal spray coatings is typically <5% by volume (Davis 2004; Espallargas 2015).

2.1. Basics of thermal spray coating

The initial step is to clean and prepare the sample's surface before coating. Small softened particles are sprayed onto the prepared surface, where they adhere to form a continuous coating. Due to the combination of thermal and kinetic energy, the sprayed particles flatten or splat onto the surface to be coated, resulting in a cohesive coating. This method of spraying can be repeated for successive layer formation (Davis 2004; Espallargas 2015; Hui et al. 2007).

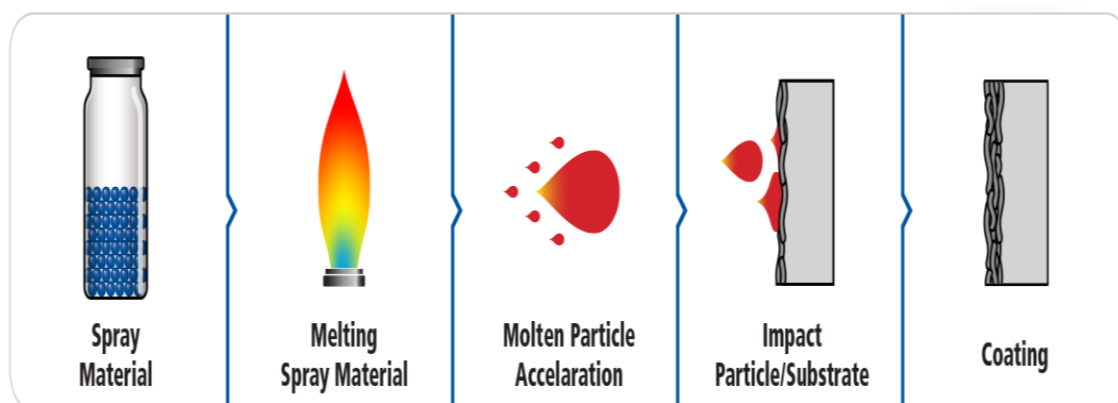


Figure 8: Basics of Thermal Spraying (Espallargas 2015)

The materials used in thermal spraying are principally powders, rods, and wires. Based on their intrinsic characteristics, materials used in industrial applications are selected for designing and manufacturing the component of the required specifications. Structural components, where strength or fracture resistance is critical, are a good example. Furthermore, any designed component will be exposed to a specific environment during

the service operation. This interaction can significantly shorten the lifetime or change the properties to the point where they no longer meet the expected requirements. The two typical examples are components exposed to corrosive environments, where the combined effect of salt and humidity corrodes the component's surface, and high-temperature applications, like turbine blades, where the unprotected component would be damaged due to exposure to elevated temperature (Davis 2004; Espallargas 2015).

2.2. Thermal spray coating processes and techniques

These processes are grouped into three major categories: flame spray, electric arc spray, and plasma arc spray.

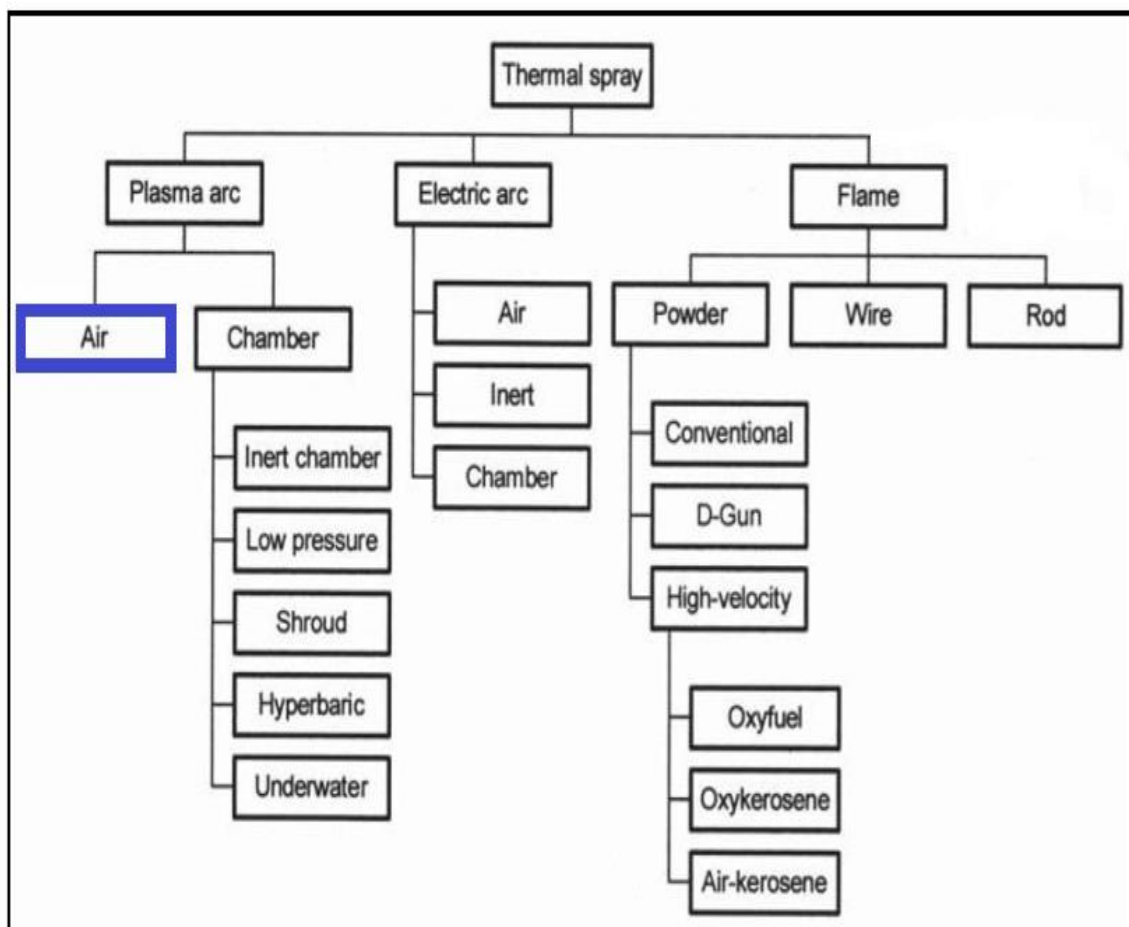


Figure 9: Thermal Spray Coating Techniques (Davis 2004)

2.3. Plasma arc (air or atmosphere)

Plasma, often called the fourth state of matter, consists of neutral atoms, positive ions, and free electrons. Plasma is created by transferring energy into gas until the energy level is high enough to ionize the gas, allowing electrons and ions to act independently. The plasma state is attained in an electric field when currents can be sustained as free electrons move

through the ionized gas. When the energy input is removed, the electrons and ions recombine, releasing heat and light energy (Davis 2004; Espallargas 2015; Lech Pawlowski 2008). The plasma generator consists of a circular anode, usually copper, and a tungsten cathode. The cathode is made of graphite in a water-stabilized torch. The electric arc discharge powered by a generator via the connector heats the working gases, which expand in the atmosphere and form a jet. The powder suspended in a carrier gas is injected into the jet. After the powder is melted and accelerated in the jet, the particles impact the substrate and form the coating (Davis 2004; Espallargas 2015; Hui et al. 2007).

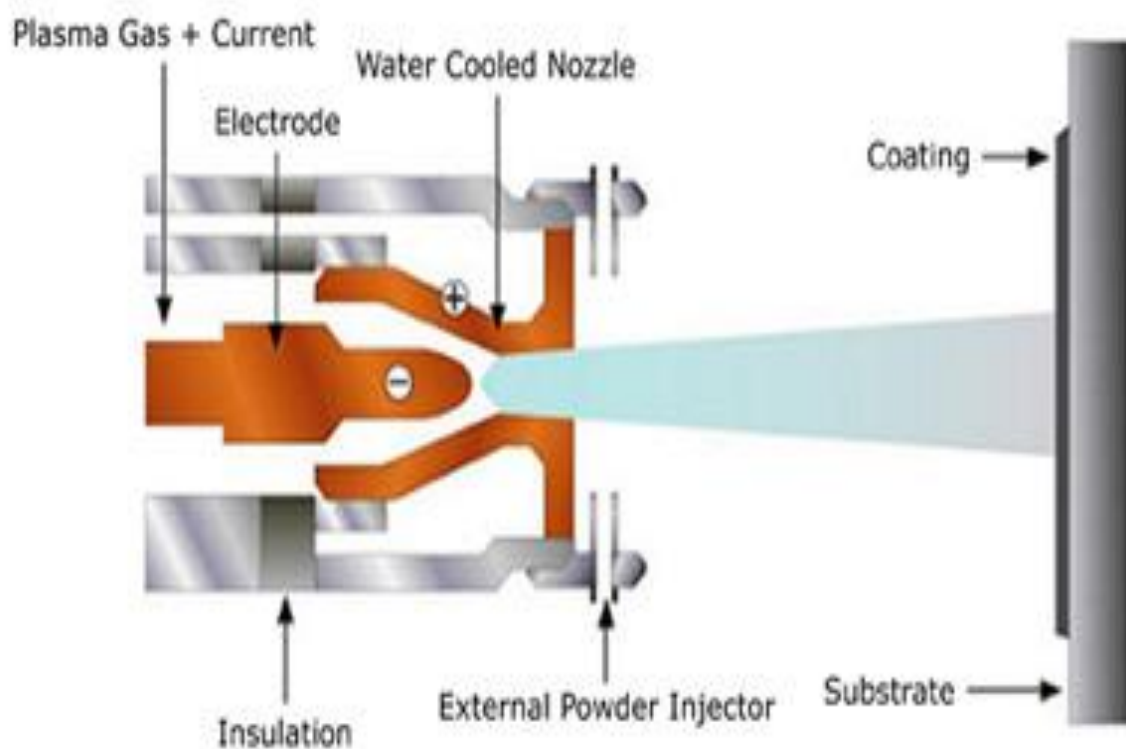


Figure 10: Plasma Arc Thermal Spray Process (Singhal 2000)

2.4. Comparison of coating techniques

There are a variety of coating techniques and coating materials available in the market. The figure below shows the processes' differences based on coating thickness and substrate temperature. Based on the application, a suitable process is chosen with appropriate parameters. The figure implies that the thermal spray coating process is versatile as it covers an extensive range of coating thicknesses and substrate temperatures (Espallargas 2015).

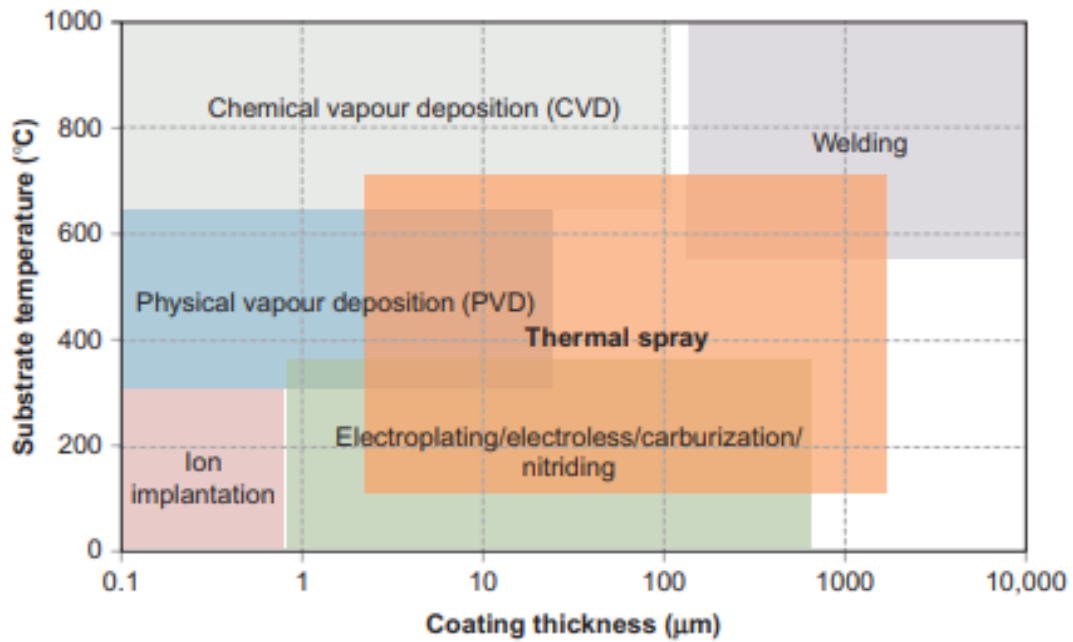


Figure 11: Comparison of different coating techniques (Espallargas 2015).

2.5. Cross-section of thermally sprayed layer

A cold-sprayed layer's structure is lamellar, somewhat similar to a cast iron structure. Micro-pores and oxide inclusions contribute to the low frictional coefficient and high hardness of some sprayed metal layers. Micro porous sprayed layers are also excellent at retaining lubricants, preventing wear caused by metal/metal contact.

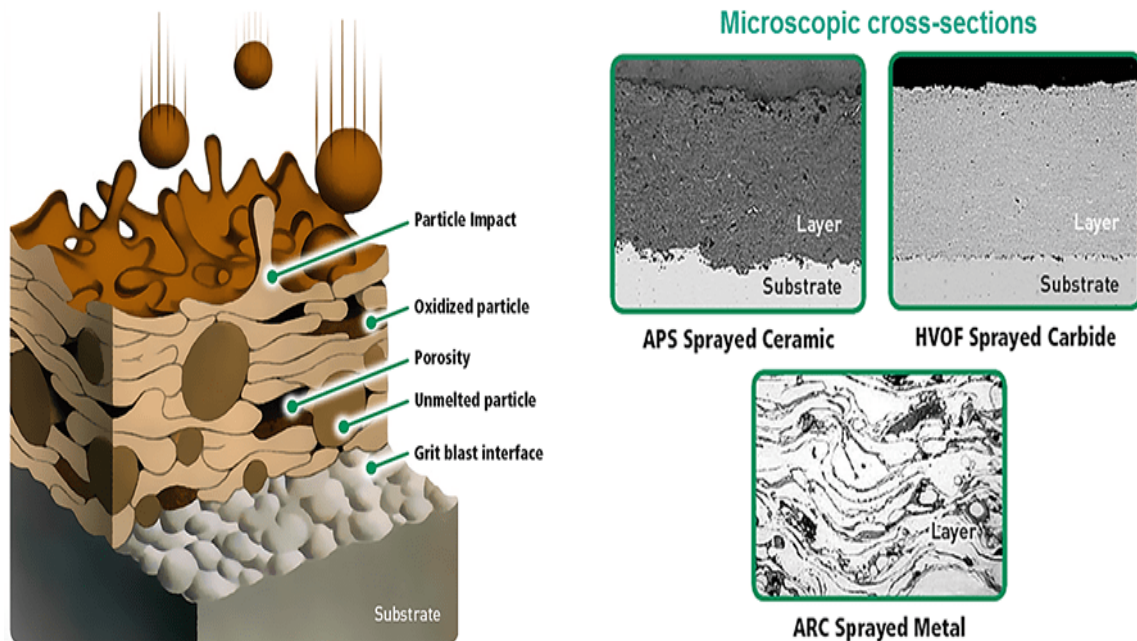


Figure 12: Schematic cross section of thermally sprayed layer (Kandeva-Ivanova et al. 2016)

2.6. Bonding mechanisms

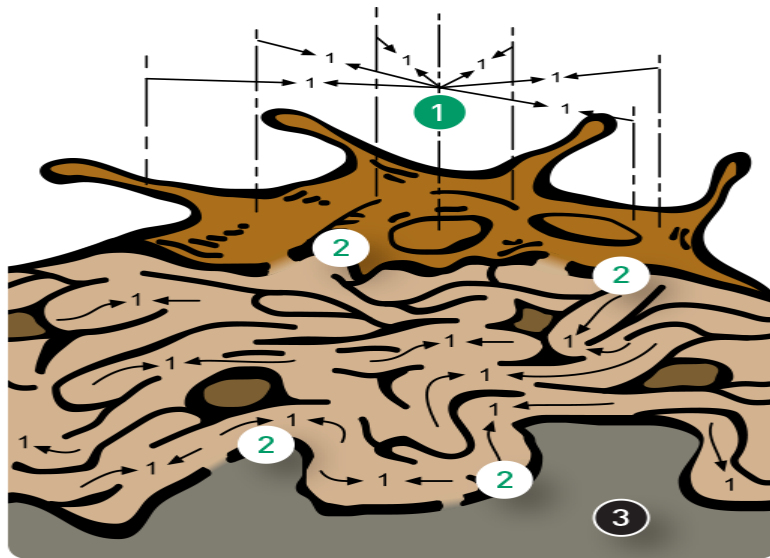


Figure 13: Bonding Mechanisms (Kandeva-Ivanova et al. 2016)

At the coating/substrate interface and between the particles

1. Mechanical Keying: Interlocking/anchoring
2. Diffusion bonding: Metallurgical bonding
3. Other adhesive: Chemical and physical bonding mechanisms – oxide films, Van der Waals forces, etc.

2.7. MCF coating obtained by air plasma spray (APS) coating process

For a feasible coating material, it should possess the following characteristics (Wu and Liu 2010)(Vaßen et al. 2016)(Puranen et al. 2011):

- i. A minimal value of diffusion coefficients of Cr and O is necessary for the coating to effectively inhibit chromium and oxygen transport.
- ii. Chemically compatible and stable with the substrate, electrodes, seal materials, and contact pastes are required.
- iii. Over the applied temperature range, it should exhibit thermodynamic stability in both oxidizing and reducing atmospheres.
- iv. It must have low ohmic resistance to maximize electrical efficiency.
- v. An excellent CTE match with substrate, thus reducing the coating spallation during thermal cycling.
- vi. Thermal conductivity at the lowest limit of 5 W/m/K, when generated heat from the cathode, is transferred to the anode for endothermic fuel reformation reactions.

- vii. When used as a stationary and auxiliary power unit under external stresses and vibrations, the coatings with the metallic substrate should have high-temperature strength, creep resistance, and structural support.

Perovskite coating: The perovskite coatings mitigate inward oxygen movement and outward Cr diffusion from the substrate, but depositing dense perovskite coatings is challenging (Yang et al. 2017). The diffusion of Cr from Plansee Ducrolloy was significantly reduced by Mn–Co–O spinel coating. Deposition of MnCo₂O₄ coating on SS430 was done by slurry coating followed by mechanical compaction and air-heating. Densification of this spinel hindered Cr₂O₃ sub-scale growth, with a reduction in the electrical resistance across the scale. The Mn_{1.5}Co_{1.5}O₄ spinel coating deposited on Crofer 22 APU substrate showed an effective reduction in contact resistance between the cathode and the steel and hindered Cr outward diffusion. Crofer 22 APU steel coated with MnCo_{1.9}Fe_{0.1}O₄ spinel improved the electronic conductivity of the substrate and effectively mitigated the Cr outward migration (Wu and Liu 2010; Yang et al. 2017).

Nitride coatings: Nitride coating have superior wear resistance and has been widely used in tool coatings. The low resistance and high-temperature stability of nitride coating could be an alternate coating for SOFC interconnect. Physical Vapour Deposition (PVD) has been widely used to produce nitride coatings for SOFCs interconnect. According to the findings, incorporating oxide into nitride coatings reduces Fe and Cr migration from the substrate as nitride coatings could remain stable at 700 °C. The limitations include high capital cost, low deposition rate, and unstable nitride at temperatures higher than 600 °C (Mah et al. 2017; Wu and Liu 2010; Yang et al. 2017).

Perovskite coatings: The structure of perovskite has a general formula, ABO₃, where A is a lanthanide (such as La in most cases but sometimes Ce, Pr, or Nd) and B a transition metal such as Co, Mn, Fe, Cr, Cu or V. Sites A are usually substituted by alkaline earth metals such as Sr, Ca or and transition metal for site B. LaCrO₃ deposited by Radio Frequency sputtering showed a two-step phase transformation from the as-deposited amorphous phase. The first step is transforming the amorphous state to a significant intermediate phase: monoclinic LaCrO₄ monazite. A limited amount of La₂CrO₆ phase was also formed. The LaCrO₄ getting transformed into the LaCrO₃ perovskite phase is the second step. During this transition, the appearance of nanostructures has excellent potential for use as SOFC interconnect coating. Due to the high electrical conductivity, thermal

compatibility, and stability in the oxidizing environment, LSM is widely used as SOFC cathode material (Mah et al. 2017; Wu and Liu 2010; Yang et al. 2017).

Reactive element oxides: The reduction of high-temperature oxidation rate and contact resistance and restricted oxide-scale spallation was observed by with addition of reactive elements, such as Y, La, Ce, or their oxides as dispersed particles in the coating. The REO coatings were ineffective in mitigating chromium diffusion to surface as the coating is usually thin (less than 1 mm) and highly porous. Sol-gel and metal-organic chemical vapor deposition are the most desired techniques for depositing REO coatings (Mah et al. 2017; Wu and Liu 2010; Yang et al. 2017).

Spinel: Spinel coatings have shown better results preventing oxygen inward and Cr outward diffusion than perovskite coatings. The reaction of chromium oxide and diffusion of Mn from the Crofer 22 APU steel leads to the formation of MnCr_2O_4 . Spinel conduct by hopping charges between cations in the octahedral sites. $(\text{Mn}, \text{Co})_3\text{O}_4$ spinel was considered the most promising coating material for SOFC interconnect. Chromium migration was remarkably reduced due to the $(\text{Mn}, \text{Co})_3\text{O}_4$ spinel layer and had a close CTE match with the substrate. The ASR predicted at 10000 h was $0.024 \text{ m}\Omega \cdot \text{cm}^2$ (Mah et al. 2017; Wu and Liu 2010; Yang et al. 2007, 2017).

A closely packed oxygen lattice with cations in tetrahedral and octahedral positions constitutes the spinel structure. The lattice parameters are observed in the range of 0.805-0.850 nm. Among the various $\text{Mn}_{1+\delta}\text{Co}_{2-\delta}\text{O}_4$ spinel compositions, $\text{Mn}_{0.5}\text{Co}_{2.5}\text{O}_4$ ($\delta=-0.5$) and MnCo_2O_4 ($\delta=0$) that exhibited a cubic spinel structure displayed Mn on octahedral interstitial sites and Co on both tetrahedral and octahedral interstitial sites in the face-centered cubic oxygen ion lattice. $\text{Mn}_{2.5}\text{Co}_{0.5}\text{O}_4$ ($\delta=1.5$) and Mn_2CoO_4 ($\delta=1.0$) demonstrated a tetragonal spinel structure. A cubic and tetragonal phase were found in dual-phase material $\text{Mn}_{1.5}\text{Co}_{1.5}\text{O}_4$ ($\delta=0.5$) spinel. A cubic to tetragonal phase transformation occurred in $\text{Mn}_{1.5}\text{Co}_{1.5}\text{O}_4$ around 400°C , revealed by high-temperature XRD analysis. The reaction rate between the spinel material and chromia decreased significantly with the addition of Ti and Fe, improving the interconnect's long-term stability and cell performance (Wang et al. 2011).

The doping of iron (Fe) in manganese-cobalt oxide spinel improved the electrical and mechanical properties of the coating. The appropriate amount of doping in $\text{MnCo}_{2-x}\text{Fe}_x\text{O}_4$ ranges from 0.1-0.25. Plasma-sprayed coatings typically exhibit pores, cracks, and large

pull-outs. The as-sprayed MCF coating showed a FeO (wuestite) structure with a cubic configuration formed due to the melting and rapid cooling of the coating material. The spinel structure can be restored by using separate annealing, according to the XRD results of annealed samples. The peaks of a FeO kind of structure and Co_3O_4 spinel were also present in all the coatings. The selective evaporation of the component leads to Co_3O_4 spinel peaks. The plasma-sprayed $\text{MnCo}_{1.8}\text{Fe}_{0.2}\text{O}_4$ crystal structure decomposes during the transformation (solid-liquid-solid), leading to metastatic compounds. Hence, the metastable phases are formed by the transformation through diffusion and grain size development to form stable compositions, eg., Co_3O_4 (Back et al. 2020; Grünwald et al. 2019; Vaßen et al. 2016).

Thin plates of Crofer 22 APU ferritic steel were coated with $\text{Mn}_{1.05}\text{Co}_{1.86}\text{Fe}_{0.11}\text{O}_{3.98}$ by the APS process. A Lanthanum–Copper–Cobalt oxide (LCC) contact was applied by wet powder spraying (WPS) on the APS diffusion barrier coating. The rapid cooling of the coating material from the molten state to the substrate temperature during thermal spray generates tensile stresses typically observed between 340 and 430 °C. The XRD of the as-sprayed coating revealed a simple cubic CoO phase. A considerable amount of $\text{Fe}_{3-x}\text{O}_4$ phase (about 40%), a high-temperature phase, was also seen. These two phases are quenched from high temperatures by fast cooling during the spray process. A sealing heat treatment performed at 850 °C for 10 h revealed four different spinel lattices with a minor amount of wuestite. Hence, a significant recovery of the spinel structure was observed after annealing. From the SEM and XRD results, a dark matrix of spinel phase similar to Co_3O_4 , primary phase, and minor phase consisted of impurity phase of wuestite, magnetite, or MnCo_2O_4 spinel. At the interface of $\text{Mn}_{1.05}\text{Co}_{1.86}\text{Fe}_{0.11}\text{O}_{3.98}$ coating and Crofer 22 APU, Co diffuses into the steel (assuming the concentration reduction close to the interface) and Cr out of the steel.

The $\text{Mn}_{1.0}\text{Co}_{1.9}\text{Fe}_{0.1}\text{O}_4$ (MCF) coated by the APS process revealed its long-term stability and reduced chromium poisoning in actual operating conditions. During the annealing of the coating, a crack-healing effect plays an essential role in mitigating chromium evaporation in stack operation. The elevated temperature of the substrate during the plasma spraying may cause the bending of the SOFC interconnectors. $\text{Mn}_{1.00}\text{Co}_{1.89}\text{Fe}_{0.10}\text{O}_{3.88}$ coating on Crofer 22 APU ferritic steel by APS were heat treated under atmospheric condition for 3h at 500 °C, 100 h at 850 °C and 10000 h at 700 °C. Annealing at 850 °C simulates the stack sealing process, and the long-term annealing at 700 °C simulates typical

SOFC operating conditions in Jülich SOFCs. Short-term annealing for 3h at 500 °C was to study the crack-healing phenomenon (Back et al. 2020; Grünwald et al. 2019; Vaßen et al. 2016).

The primary microstructural features of an as-sprayed coating are micro-cracks and porosity. The porosity measurements determined $12.4 \pm 0.8\%$ porosity in the as-sprayed condition. The short-term annealing of 3h at 500 °C showed micro-cracks at higher magnifications, but the porosity decreased to $2.4 \pm 0.8\%$. The samples annealed for 100 h at 850 °C revealed the absence of micro-cracks even at higher magnification, but the porosity increased to $6.3 \pm 0.6\%$. Annealing the sample at 700 °C for 10000 h showed a porosity of $7.1 \pm 1.3\%$. The X-ray diffraction of the as-sprayed and 3 h annealed samples revealed the occurrence of cubic rock salt phase (Mn, Co, Fe)O. In 3h annealing at 500 °C, a spinel phase close to powder’s diffraction pattern was detected, and a cobalt-containing cubic spinel phase Co_3O_4 . After 100 h annealing at 850 °C, cobalt-rich spinel Co_3O_4 was observed. The initial spinel $(\text{Mn,Co,Fe})_3\text{O}_4$ phase was retrieved after 10000 h annealing at 700 °C (Back et al. 2020; Grünwald et al. 2019; Vaßen et al. 2016).

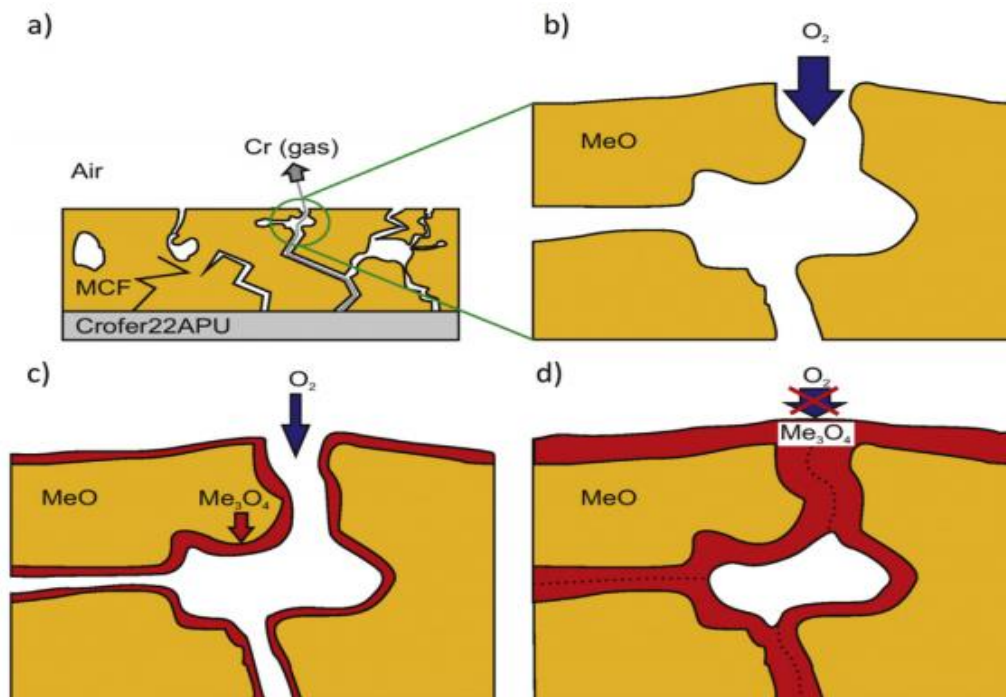
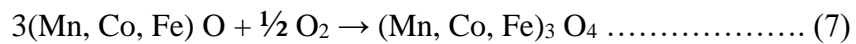


Figure 14: Schematic drawing of crack-healing process. Annealing of as sprayed APS-MCF in air, the MeO (Me = $\text{Mn}_{1.0}\text{Co}_{1.9}\text{Fe}_{0.1}$) rock salt phase is transformed into the spinel configuration Me_3O_4 . This results in volume expansion, which takes place at the MCF surfaces (c). Oxygen cannot penetrate to the bulk over the gas phase after the cracks are closed (d) (Grünwald et al. 2017).

The rock salt phase of (Mn, Co, Fe)O is only stable at high temperatures, as seen in the phase diagram of manganese-cobalt oxide (Fig. 15). The spinel-configured powder (Mn, Co, Fe)₃O₄ transforms to a rock salt configuration (Mn, Co, Fe)O in the as-sprayed coating. The method of diffusion to transform to the low-temperature stable spinel configuration is initiated by annealing the MCF coating in air. The chemical reaction of this phase transformation is described as follows:



The above reaction shows that oxygen uptake occurs during annealing in the regions of high oxygen partial pressure leading to a volume expansion in the coating. The areas where oxygen uptake is observed are the coating's surface, pores, and micro-cracks. Volume expansion induced by the phase transformation of rock salt configuration to spinel is called crack-healing (Back et al. 2020; Grünwald et al. 2017, 2019; Vaßen et al. 2016). The annealing, which leads to micro-cracks closure, restricts the diffusion of the gas phase through the coating, thereby reducing the oxidation rate.

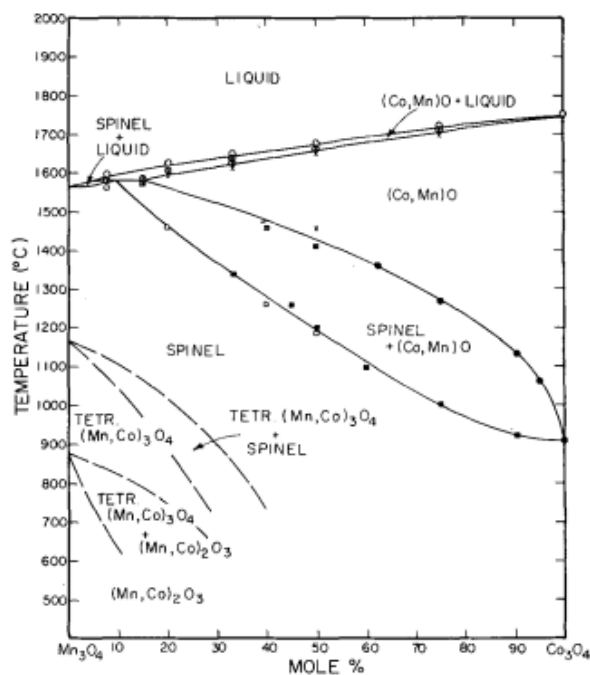


Figure 15: Phase relations in the system cobalt oxide - manganese oxide in air (Aukrust and Muan 1963)

The crack-healing of the coating leads to densification of the coating diminishing the total chromium reaching the cathode through the gas phase. This has been beneficial in mitigating the chromium evaporation in SOFCs interconnect. The ability of the coating for a crack-healing mechanism to occur depends on the amount of rock salt phase present in the coating's bulk. The major part of the oxidation is completed after the cracks are closed.

The velocity of the diffusion process is strongly dependent on temperature. By lowering the annealing temperature, the self-healing capability of APS-MCF can be prolonged over time (Grünwald et al. 2017).

2.8. Various interconnect materials and coatings

Ferritic stainless steel (FSS) coated with Co-W to reduce oxidation and Cr poisoning has been used as interconnect in SOFCs. The oxidation property and area-specific resistance (ASR) evaluated at 800 °C showed ASR values of 102 and 97 mΩ.cm² with LSM and LSCF cathodes. The combination of Co-W-coated FSS steel as the cathode material and LSM as the anode material demonstrated the optimal combination of electrical conductivity and microstructural stability. (Gan et al., 2021). In the surface modification of Crofer 22 APU steel, gadolinium oxide nanoparticles were deposited by dip-coating, and a protective-conducting layer consisting of the MnCo₂O₄ spinel was deposited electrophoretically. The unmodified steel, steel coated with a manganese-cobalt spinel layer, steel modified with gadolinium oxide nanoparticles, and a system consisting of steel after both modifications were considered for the study. The oxidation of all samples at 1073 K for 1000 and 2260 h in air showed an improvement in adhesion of the chromia scale on the Crofer substrate was improved due to the segregation of gadolinium at the grain boundaries in Cr₂O₃ scale between the substrate and spinel, reducing the oxidation rate of the coated steel. The surface modification was also beneficial in reducing chromium evaporation and improving the electrical properties of the interconnect (Brylewski et al., 2021).

The oxide formation on Crofer 22 APU metallic interconnect (fuel side) in SOFC stack operation up to 20000 h was investigated. When the Crofer interconnects are exposed to the fuel stream, a Cr-rich thermally grown oxide (TGO) is seen at the interface with the metal. A prominent Mn_xO_y presence was seen on top of the Cr-rich scale, which supports the theory of the continued reaction of TGO with selective Cr depletion. But the oxides of manganese may pose problems due to lower electrical conductivity (Ghiara et al. 2021). A two-stage oxidation behavior was explored in the oxidation study of Crofer 22 APU at 800, 825, 850, and 875 °C in air. Due to the fast diffusion of Mn ions, chromia and Mn-rich spinel phases were initially formed. In the first oxidation stage, the atmospheric oxygen and the oxygen in chromia favor the growth of chromia and Mn-Cr oxide. The second stage involves the diffusion of oxygen penetrating the Mn-Cr spinel oxide layer, which increases the growth rate of chromia. The growth of chromium-manganese spinel oxide governed by

the available atmospheric oxygen did not influence the parabolic rate constant (Park et al. 2018).

The purpose of developing a coating to increase the performance of Crofer 22 APU and other ferritic stainless steel for SOFC interconnect has led to the development of various coating materials and processes. Few coatings investigated for their characteristics and required properties in SOFC applications have been summarized. The plasma spray (PS) technique was used to spray protective Mn_2CuO_4 coating on Crofer 22 APU metallic interconnect. The deposition of molten Mn_2CuO_4 on the Crofer interconnect substrate forms a high-density coating without needing post-heat treatment. The Mn_2CuO_4 was coated by optimizing the parameter, which led to a coating with high adhesion strength and impervious to the diffusion of gases on to the substrate. The Chromia layer was not formed at the coating-substrate interface. Due to this, the Mn_2CuO_4 -coated Crofer 22 APU interconnect shows an area-specific resistance below $10 \text{ m}\Omega\text{-cm}^2$ at $800 \text{ }^\circ\text{C}$ in air. The coating performed well in continuous stack operation and repeated thermal cycling (Waluyo et al. 2018).

The $\text{Cu}_{1.3}\text{Mn}_{1.7}\text{O}_4$ coating on Crofer 22 APU stainless steel by electrophoretic deposition was found to be uniform and adherent. The coated steel was exposed to a thermomechanical densification treatment which included pre-reduction uniaxial compression at 10 ksi, a reduction annealing for 1h at $850 \text{ }^\circ\text{C}$ in forming gas that phase-separated the spinel into Cu and MnO, a post-reduction uniaxial compression at 100 ksi, followed by a densification annealing in air at $850 \text{ }^\circ\text{C}$ for 100 h. A dense chromium-rich thermally grown oxide layer near the coating-substrate interface and an outer CuO scale with small porosity on the coating surface was seen. The coating reduced the oxidation rate of uncoated Crofer steel from $1.36 \times 10^{-7} \text{ mg}^2 \text{ cm}^{-4} \text{ s}^{-1}$ to $6.25 \times 10^{-8} \text{ mg}^2 \text{ cm}^{-4} \text{ s}^{-1}$ with $\text{Cu}_{1.3}\text{Mn}_{1.7}\text{O}_4$ coating (Sun et al. 2017).

Magnetron sputtering was used to deposit Mn-Cu metallic coatings (1:1 atomic ratio) on bare and pre-oxidized SUS 430 steel. The uncoated and coated samples thermally exposed to air at $800 \text{ }^\circ\text{C}$ showed a two-layer oxide structure. The outer oxide layer formed was $(\text{Mn}, \text{Cu})_3\text{O}_4$ spinel, which consists of a distinct CuO, whereas the inner layer is a protective Cr-rich oxide. The chromium-rich layer is believed to develop from the steel substrate. The outer $(\text{Mn}, \text{Cu})_3\text{O}_4$ spinel effectively mitigated the Cr outward migration and improved the electrical performance of the surface oxide scale (Geng et al. 2017). Thin metallic Co- and

Ce/Co-coated steels considered to be used as the interconnect material in Intermediate Temperature Solid Oxide Fuel Cells (IT-SOFC) were investigated for Cr-species volatilization, oxide scale growth, and electrical performance at 650 °C and 750 °C. The study demonstrated that a decrease in temperature causes a substantial variation in the chemical composition of the oxide layer as well as thinner oxide scales and less Cr vaporization. Both Co- and Ce/Co-coated steel exhibited very low ASR values below 10 mΩ·cm² at 650 °C and 750 °C. The chemical composition change did not have a noticeable impact on the ASR. Even at low temperatures (650 °C), the Cr₂O₃ oxide layer is predicted to be the primary contributor to the ASR (Falk-Windisch et al. 2017).

MnCo_{1.7}Fe_{0.3}O₄ coating on Crofer 22 APU was assessed for its coating density effect on oxidation kinetics and Cr evaporation rate. Compared to the heat treatment in air, denser coatings were obtained by a two-step reduction and re-oxidation heat treatment process. Though initial coating density did not influence long-term oxidation behavior at 800 °C, assessing the Cr-depletion criterion in air sintered MnCo_{1.7}Fe_{0.3}O₄ spinel coating provided an effective barrier to Crofer steel substrate in its service time of 40000 h at 800 °C (Talic et al. 2017a). Corrosion protection layers of MnCo₂O₄, MnCo_{1.7}Cu_{0.3}O₄, and MnCo_{1.7}Fe_{0.3}O₄ were deposited electrophoretically on Crofer 22 APU alloy used as metallic interconnects in solid oxide fuel cell stacks. The oxidation rate of the Crofer interconnect was reduced by the coating at 800 °C and 900 °C. After 4370 h aging, all coated samples exhibited three-time lower ASR than bare Crofer 22 APU steel. The MnCo₂O₄ showed the lowest increase in ASR with time, which was followed by MnCo_{1.7}Fe_{0.3}O₄ and MnCo_{1.7}Cu_{0.3}O₄ coatings. Though the doping of Fe and Cu in the coatings showed an insignificant effect at 800 °C, a decrease in the development of a Cr-rich reaction layer at 900 °C was observed (Talic et al. 2017b).

Hosseini et al. investigated the CuFe₂O₄ spinel coating deposited on bare and pre-oxidized Crofer 22 APU steel via screen-printing. A reactive sintering process achieved good adhesion between the coating and substrate. The deposition of spinel coating on the Crofer steel significantly decreased the ASR. It also acts as a diffusion barrier for the inward flow of oxygen by hindering subscale growth. The uncoated Crofer substrate showed an ASR of 48 mΩ·cm², whereas the bare and pre-oxidized CuFe₂O₄ spinel coated Crofer steel showed an ASR of 13.8 and 26.7 mΩ·cm² at 800 °C after 400 h oxidation (Hosseini et al. 2016).

In order to diminish the degradation of cathode performance by Cr poisoning, SUS 430 alloy used as metallic interconnect was coated with spinel oxides with difference stoichiometric compositions of $\text{MnCu}_x\text{Co}_{2-x}\text{O}_4$ ($x = 0.1, 0.3, 0.5, 0.7$). In this study, the determination of oxidation characteristics and effectiveness of protective coating was investigated by evaluating the effect of Cu doping of spinel on electrical conductivity and CTE. In a comparison of all coating, $\text{MnCu}_{0.5}\text{Co}_{1.5}\text{O}_4$ spinel showed the highest electrical conductivity of $105.46 \text{ S}\cdot\text{cm}^{-1}$ at $750 \text{ }^\circ\text{C}$ in air and an average CTE value of $12.27 \times 10^{-6} \text{ K}^{-1}$ at a temperature range of $20\text{-}960 \text{ }^\circ\text{C}$. $\text{MnCu}_{0.5}\text{Co}_{1.5}\text{O}_4$ spinel coating has effectively suppressed the growth of chromia and the Mn-Cr spinel layer. The oxidation rate constant was as low as $2.76 \times 10^{-15} \text{ g}^2\cdot\text{cm}^{-4}\cdot\text{s}^{-1}$, and the ASR contributed by the oxide scale is $8.04 \text{ m}\Omega\cdot\text{cm}^2$ at $750 \text{ }^\circ\text{C}$ (Xiao et al. 2016). The electrodeposition process was used to coat five different CoFe coatings ($\text{Co}_{0.9}\text{Fe}_{0.1}$, $\text{Co}_{0.8}\text{Fe}_{0.2}$, $\text{Co}_{0.7}\text{Fe}_{0.3}$, $\text{Co}_{0.6}\text{Fe}_{0.4}$, and $\text{Co}_{0.5}\text{Fe}_{0.5}$) on AISI 441 substrate. The coated specimens were oxidized at $800 \text{ }^\circ\text{C}$ for 5 h. Lower content of Fe, about $\leq 30 \text{ at.}\%$, showed lesser ASR and effective coating in restricting the chromia scale growth. The electrochemical performance of the cathode was improved with the low Fe coating than the bare interconnect (Shen and Lu 2016).

The Crofer 22 APU steel coated with MnCo_2O_4 and $\text{MnCo}_{1.8}\text{Fe}_{0.2}\text{O}_4$ was investigated for SOFC interconnect application at $750 \text{ }^\circ\text{C}$. ASR of the coating was evaluated for 5300 h, which included several thermal cycles. The coated samples exhibited approximately four times slowed ASR increase than the uncoated samples. The average rate of increase in the ASR of the spinel coated sample was $0.3 \text{ m}\Omega\cdot\text{cm}^2/1000 \text{ h}$. The composition of the coating and the coating thickness showed no influence on the electrical conductivity. The prediction of ASR up to 40000 h operation would result in an ASR of $30 \text{ m}\Omega\cdot\text{cm}^2$. The outcome showed the use of porous Mn-Co spinel coating as a protective barrier for steel in SOFC interconnect, which can hinder the chromia scale growth rate and enhance electrical properties (Molin et al. 2016).

The oxide scale formed on AISI 430 ferritic stainless steel was investigated for its protective characteristics from chromium poisoning and enhancement in the ASR. The $\text{Cu}_{1.3}\text{Mn}_{1.7}\text{O}_4$ spinel coating was deposited on AISI 430 steel by screen printing. The oxygen diffusivity between coating and substrate was substantially decreased after 500 h oxidation at $750 \text{ }^\circ\text{C}$, decreasing the sub-scale oxide growth rate. The uncoated sample had a ASR of $63.5 \text{ m}\Omega\cdot\text{cm}^2$ after 500 h oxidation, while the spinel coated sample had a ASR of $19.3 \text{ m}\Omega\cdot\text{cm}^2$. A 70% reduction in the ASR of the $\text{Cu}_{1.3}\text{Mn}_{1.7}\text{O}_4$ coating not only enhanced

the electrical conductivity but also effectively reduced sub-scale growth and prevented the diffusion of chromium from the steel substrate to the cathode (Hosseini et al. 2015).

Doping of Cu in Mn-Co spinel has shown improved electrical properties, and CTE match with Crofer steel interconnect. A $\text{Mn}_{1.4}\text{Co}_{1.4}\text{Cu}_{0.2}\text{O}_4$ spinel coating was deposited on Crofer 22 APU steel substrate by powder reduction technique. A reactive sintering process was employed to achieve good adhesion between the coating and the substrate. The oxidation of the spinel coated steel at 800 °C for 530 h showed an ASR less than $4 \text{ m}\Omega\cdot\text{cm}^2$ (Chen et al. 2015). A Co-Mn alloy was electro-deposited on 430 stainless steel and heat treated at 750 °C in argon and at 800 °C in the air to attain Co-Mn spinel coating. The heat treatment resulted in forming of an outer MnCo_2O_4 layer and an inner Cr-rich oxide layer on 430SS. The spinel coating has improved the oxidation resistance of the steel with reduced contact resistance (Zhang and Zeng 2014).

A Cu and Ni-doped $\text{Mn}_{1.5}\text{Co}_{1.5}\text{O}_4$ (MCO) spinel coating were deposited as a protective coating on Crofer 22 APU metallic interconnect slurry coating process, followed by heat-treatment. An improvement in the sintering characteristics, electrical conductivity, and CTE match with Crofer interconnect due to the doping of Cu and Ni. The ASR of the coated samples at 800 °C was as low as $13.9\text{-}17.6 \text{ m}\Omega \text{ cm}^2$. The Cu doped $\text{Mn}_{1.5}\text{Co}_{1.5}\text{O}_4$ spinel coating mitigated the Cr-species migrating from the steel interconnect, thereby decreasing the Cr poisoning of a cathode (Park et al. 2013).

A thin film of CoMn coating ($\sim 2 \mu\text{m}$) was deposited on as-received and pre-oxidized (100 h at 800 °C in the air) Crofer 22 APU ferritic steel via magnetron sputtering. The samples were exposed to single atmosphere (moist air) and dual atmosphere environments (moist air/moist hydrogen) for 200 h at 800 °C. The pre-oxidation of the Crofer substrate inhibited the outward transport of iron from the steel to the surface, reducing the oxide layer thickness for both bare and CoMn coated steel (Amendola et al. 2012).

The surface of ferritic stainless steel was modified by coating Cu-Mn-Co spinel powder via slurry dip-coating, followed by the sintering process. Adding Cu to Mn-Co spinel was advantageous in altering the thermal expansion behaviour to be more compatible with metallic interconnect material and reduce the sintering temperature. Excellent anti-oxidation performance was achieved by the Cu-Mn-Co spinel coating and acted as a mass barrier to the outward diffusion of Cr (Xu et al. 2011). The spin coating technique was employed in depositing three lanthanum-based perovskite ceramic compounds,

La_{0.8}Ca_{0.2}CrO₃, La_{0.8}Sr_{0.2}CrO₃, and La_{0.8}Sr_{0.2}MnO₃ on ferritic stainless steel. The aging of the coated samples at 800 °C in the air for 1600 h enabled the growth of (Mn, Cr)₃O₄ spinel phases with coarser crystalline structures and higher levels of Mn content. The coated samples exhibited an ASR of ~3 mΩ cm² after aging for 1600 h, which was one-third of the uncoated sample. The Mn content and the crystallite size of the spinel phase played an important role in the ASR difference (Shong et al., 2011).

The surface modification of SUS 430 ferritic stainless steel was done by coating NiCo₂O₄ spinel coating using the sol-gel process. The cyclic oxidation of the uncoated and coated steel in the air at 800 °C for 200 h resulted in a significant enhancement in oxidation resistance with a rate constant of $8.1 \times 10^{-15} \text{ g}^2 \text{ cm}^{-4} \text{ s}^{-1}$. The inhibition of the resistive Cr₂O₃ growth and conductive spinel phase formed improved the electrical conductivity of the steel (Hua et al. 2010b).

2.9. Area-specific resistance

The area-specific resistance (ASR) was measured by analyzing the impedance spectra using Nyquist or Bode plots (Pan et al. 1998). The ASR value of about 0.1 Ω cm² has been generally accepted upper limit for SOFC interconnect (Morán-Ruiz et al. 2015; Zhu and Deevi 2003). The coatings like MnCo₂O₄ and MnCo_{1.8}Fe_{0.2}O₄ on Crofer 22 APU at 750 °C for 5000 h exhibited a four times lower ASR of coated samples compared to uncoated steel (Molin et al. 2016). The observation of the impedance data of cobalt-coated Crofer 22 APU showed oxide layers of chromia, chromium containing cobalt oxide, and spinel of cobalt chromium (Velraj et al. 2014). The oxidation of Mn-Co-O spinel coated 430SS at 850 °C predicted an ASR of approximately 0.5 Ω.cm² after 50000 h in the air (Chen et al. 2005). Impedance spectroscopy of AISI 304 steel after oxidation at 800 °C for 200 h revealed the oxide layers of thin outer MnCr₂O₄ and thick inner Cr₂O₃ with an experimentally determined activation energy of about 0.45 and 0.35 eV for respective oxides (Song SH and Xiao P 2003).

2.10. The adhesion strength of MCF coating

Atmospheric plasma spray is known to be an overlay coating on a substrate. The coating is said to have strong adherence in the as-sprayed condition due to mechanical interlocking between the coating particles and the roughened substrate. Evaluating the adhesion strength of these coatings is of interest and can vary due to the difference in physical properties and thermal mismatch.

The quality of adhesion between the substrate and the coating can impact the interconnect lifespan of SOFCs. There is a wide range of methods for assessing adhesion/cohesion bond strength in coatings, but none is considered ideal. Every test method has its advantages and disadvantages. The scratch test method has proven to be reasonably reliable, wherein its advantages lie in the ease of use and no special requirement for specimen preparation (Das et al. 2019; Sekler et al. 1988; Vencl et al. 2011). The scratch tests can be performed under constant or variable loading conditions. This test has proven beneficial for many years for determining the adhesion between coating and substrate and evaluating various mechanical failure modes in coatings (Vencl et al. 2011).

Researchers employed different methodologies to assess the adhesion strength of plasma sprayed coatings, with a scratch indentation test utilized in a few investigations. M. Hadad et al. (Hadad et al. 2007) showed that the interfacial indentation test is very effective in studying the impact of interfacial roughness and coating adhesion. S Hazra et al. (Hazra and Bandyopadhyay 2012) used a scratch indentation test to study the failure mechanism of plasma-sprayed alumina topcoats from crushed, agglomerated, nanostructured powders and two bond coats, nickel aluminum and nickel-chromium. Large area spallation was observed as a prominent failure mode in all coatings, and in most cases, tensile cracks were noticed. The scratch test was also used on different thermal sprayed ceramic, cermet, and metal coatings to analyze the intra-lamellar quality and long-range cohesion of the coatings (Nohava et al. 2010). The reliability and reproducibility of cross-sectional scratch test on plasma-sprayed yttria-stabilized zirconia (YSZ) and TiO₂ coatings with Ni-Cr bond coat were studied by E. Byon et al. (Byon et al. 2013). They emphasized that a scratch test on the cross-section of the plasma spray-coated specimen can be used as an effective way of quantifying the adhesion or cohesion strength. Even though the scratch indentation test is rarely utilized, the results suggest that it can be useful for measuring the coating's adhesion strength. A study on the scratch test using progressive and constant load on composite coatings deposited on Fe430B substrates was attempted, and their results were discussed independently (Barletta et al., 2013). However, the combined approach of progressive and constant loading conditions has not been attempted, interpreted, and correlated elsewhere.

2.11. Early-stage oxidation of Crofer 22 APU steel

The commercially available ferritic steels used for SOFC have a chromium content ranging from 18 to 28 wt.%. As the content of chromium increases in the alloy, the oxidation

resistance also increases (Niewolak et al. 2010; Quadakkers et al. 2000; Young et al. 2011). In the temperature range of 600-900 °C, chromia is the prominently formed oxide scale layer (Niewolak et al. 2016). At temperatures greater than 1000 °C, chromia acts as an electronic conductor, and the electrical conductivity is independent of oxygen partial pressure (Singheiser et al. 2010). Titanium presence in the alloy forms titania precipitates in the sub-scale region of chromia. At low oxygen partial pressure, titanium dissolves in the inner part of the chromia scale, and titanium re-precipitates at higher oxygen pressure in the outer part of the scale due to the reduced solubility in Cr₂O₃ as the oxygen partial pressure increases (Niewolak et al. 2014, 2016; Quadakkers 1987; Shindo et al. 1986; Singheiser et al. 2010). At elevated temperatures, the inclusion of Ti in the oxide layer will increase the growth rate of chromia (Singheiser et al. 2010).

The conventional method to study the oxidation kinetics and mechanism involves characterization techniques such as XRD, FE-SEM, and depth profiling using cross-sectioned samples exposed to long-term oxidation. Whereas the initial stage oxidation of high oxidation materials like Crofer 22 APU is carried out in a shorter duration in a controlled atmosphere, it would not be easy to identify and evaluate using state-of-the-art characterization tools. Understanding such early growth of complex two-layer oxide during initial stage oxidation mechanisms would be better when using surface analytical tools such as GIXRD and GD-OES for quantification.

Besides conventional characterization tools, Glow Discharge Optical Emission Spectrometer (GD-OES) is an interesting tool for quick depth profiling surfaces, thin films, and coating. In GD-OES, the distribution of all elements can be obtained for a specific depth from the surface (Nelis and Pallosi 2006; R. Kenneth Marcus 2002). GD-OES can quantify the oxide scales formed on the surface by interpreting the intersection of the oxygen depth profile with the depth profile of other elements (Ghosh et al., 2013).

The Grazing Incidence XRD (GIXRD) analysis is more accurate than traditional XRD for investigating thin films of tens of nanometres thick or the oxide scales formed after oxidation (Achilli et al. 2022). The GIXRD measurement uses a beam incidence angle (ω) of $<5^\circ$ when the detector is rotated around the sample. Due to the low ' ω ' applied to the incidence beam, the signals from the surface of the specimen increases which is favourable in detecting the oxides of nanometre thickness (Stabrawa et al. 2019). The advantage of using GIXRD is that the incoming X-ray beam's penetration depth can be accurately regulated. This method also allows the investigation of monolayers on single crystallite

surfaces and vital information of a crystalline surface can be obtained by non-destructive analysis (Marra et al. 1979; Scherzer et al. 2019).

2.12. Thermal expansion induced thermal mismatch of MCF coated Crofer 22 APU metallic interconnect

Chromia-forming alloys are a favorable choice to facilitate the thermal expansion coefficient match with other components. In addition, the electronic conductivity of chromia (Cr_2O_3) is higher than other oxide scales (Fergus 2005; Han et al. 2007; Öztürk et al. 2018; Zhu and Deevi 2003). But the continued growth of the Cr_2O_3 scale will result in ohmic losses and becomes incompatible with other components. The volatile gaseous components of chromium species can degrade the cathode and cathode/electrolyte interface (Hu et al. 2020; Mohamed et al. 2022; Park et al. 2018). The degradation of the interconnect, electrode, and electrolyte affects the long-term stability of the cells. The application of diffusion barrier coatings have been realized to mitigate the degradation of metallic interconnect (Huang et al. 2008; Miguel-Pérez et al. 2012; Przybylski et al. 2014; Yang et al. 2005; Zhang et al. 2014). Ceramic protective coatings have shown promising results in minimizing chromium evaporation and controlling the oxide scale growth (Hassan et al., 2020).

The thermal stresses generated require a detailed analysis of linear expansion and coefficient of thermal expansion (CTE) since the mismatch in thermal expansion between the coating and substrate is prevalent during the coating deposition, heat treatment, and real-time implementation of SOFC. The formation of oxides, induced residual stresses, and interfaces are the characteristics of coatings induced by the thermal spray process. As bulk expansion behavior is commonly observed in thermal spray coatings, determining the correct values of CTE is essential for designing SOFC and predicting the coating performance under thermal stress (Bejarano et al. 2019). The spray process parameters influence thermal expansion due to phase changes caused by oxidation, precipitate formation, etc. The thermal mismatch stresses generated due to the dissimilarity in CTE between coating and substrate result from a more significant temperature gradient during the long-term spraying process, phase transformation, etc. (Khan and Lu 2007; Kustov et al. 2001; Tao et al. 2022) The thermal mismatch strains strongly affect coated components' bond strength and thermal fatigue life (Khor et al. 1999). As significant stresses are generated during oxidation, the determination of thermal stresses associated with oxide

layer growth on the substrate and coating is important to predict the lifetime of the system (Panicaud et al. 2021).

The growth stresses occurring during the isothermal oxidation process may influence the protective properties of the oxide scales by reducing the lifetime of the metallic substrate. Irrespective of the particular alloy being oxidized or the kind of oxide formed, the growing oxide film is usually under significant stresses (around GPa). Thus, it is important to accurately determine the strain and stress fields associated with the growth of oxide films on metallic substrates to investigate the lifetime of such systems (Panicaud et al. 2021).

The coefficient of thermal expansion quantifies the expansion and shrinkage due to changes in the temperature of a material. The CTE of substrate and coating materials strongly influences the adhesion strength of the overlay coating. The large variation in CTEs leads to a mismatch in strain, causing cracks and degradation (Bednarz et al. 2019; Loghman-Estarki et al. 2014; Öztürk et al. 2021). The influence of residual stress concentration due to a mismatch in thermal expansion behavior between the substrate and coating resulted in delamination/failure of the coating (Chen et al. 2010a; Jamali et al. 2012; Khor and Gu 2000; Molin et al. 2014; Tao et al. 2022). The mismatched thermal expansion coefficient at the interface causes the local volume to change across the interface (Cernuschi et al. 2005; Khan et al. 2021; Tao et al. 2020). In YSZ coating on Ni-based superalloy GH3128, the mismatch in strain generates internal stress in the coating resulting in damage to the outer/ inner layer of the coating interface (Tao et al. 2022). In a Fe doped Mn-Co spinel coating, the Co occupancy in octahedral sites is substituted by Fe due to higher ionic radius; the increase in lattice parameter and reduction in CTE is also caused by Fe addition (Liu et al. 2013; Masi et al. 2017; Talic et al. 2018).

The thermal expansion behavior of various SOFC interconnect materials has been studied using the dilatometer, and the CTE match with other components was reported (Sakai et al. 2005; Simner et al. 2003). A high-temperature vertical dilatometer measures the CTE of (Mn, Co)₃O₄ (25-1000 °C) doped with Fe. The CTE of MnCo_{1.66}Fe_{0.34}O₄ and MnCo_{1.66}Fe_{0.34}O₄ were $12 \times 10^{-6} \text{C}^{-1}$ and $11.2 \times 10^{-6} \text{C}^{-1}$, respectively, which showed a close match of CTE to ferritic stainless steel ($11-13 \times 10^{-6} \text{C}^{-1}$). The CTE increase with increasing cobalt was offset by doping with Fe (Wang et al. 2011). Few studies also focus on investigating the thermal mismatch behavior of other components of SOFC like anode, cathode, and electrolyte (Church et al. 2005; Ding et al. 2009; Nakajo et al. 2006).

2.13. Effect of MCF coating on the oxidation resistance of Crofer 22 APU steel

Compared to the Al_2O_3 and SiO_2 forming materials, the Cr_2O_3 scales formed on the alloy surface exhibited a lower oxide growth rate (Fergus 2005). But the Cr (VI)-species that evaporates from these steel results in Cr poisoning and a reduction in cell efficiency (Fergus 2007). Cell performance is also affected by the low electric conductivity of the Cr_2O_3 oxide layer (Jiang et al. 2002). With the addition of a small percentage of Mn, the Fe-Cr alloys form spinels of Mn and Cr (Horita et al. 2003). These alloys with below 1 wt.% Mn content led to $(\text{Mn}, \text{Cr})_3\text{O}_4$ spinel formation on top of Cr_2O_3 , which increases the electrical conductivity and mitigates the Cr evaporation due to lower evaporation pressure of the spinel than chromia (Yang et al. 2004, 2007). Studies have shown that forming low conductivity Cr_2O_3 oxide increases the area-specific resistance (ASR) under long-term exposure (Fergus 2005). The growth of the oxide scales can be reduced, and a protective spinel coating can increase the electrical conductivity of the alloy (Zhao et al., 2020). Various materials used as a coating for SOFC applications include rare earth perovskites, reactive element oxides, and conductive spinels (Shaigan et al. 2010).

The oxidation kinetics of $\text{MnCo}_{1.7}\text{Fe}_{0.3}\text{O}_4$ spinel coating on Crofer 22 APU showed that Cr evaporation was reduced by 97% by reduction and re-oxidation heat treatment causing the coating to densify (Talic et al. 2017a). The oxidation study on LSCF48 film deposited on Crofer 22 APU carried out at 800 °C for 200 h in air showed a reduction in oxidation rate by three times of LSCF48 coated Crofer steel than the uncoated steel. The reduction in oxide growth caused by the low oxygen diffusion coefficient of LSCF48 film was seen after 2400 h of oxidation at 800 °C (Durda et al. 2020). The evolution and growth of Cr_2O_3 , MnCr_2O_4 , and surface nodules were the reason for two-stage oxidation in Mn containing Fe-16Cr alloy oxidized at 650–850 °C in the air up to 500 h (Jian et al. 2006). The investigation of the oxidation behavior of $\text{Mn}_{1.5}\text{Co}_{1.5}\text{O}_4$ (MCO) coated Crofer 22 APU and Haynes 230 (H230) between 700–900 °C showed a 5.5 times reduction in the oxidation rate of Crofer 22 APU but showed no effect on the kinetics of Haynes 230 alloy (Chen et al. 2010b). The effect of Mn content (Mn = 0.0, 0.5, 1.0, and 3.0 wt.%) in Fe-17Cr alloy on oxidation behavior and electrical conductivity were investigated. The increase in Mn content in the alloy increased the oxidation rate due to the faster diffusion of Mn. The ASR also increased due to forming thicker oxides at a high oxidation rate (Hua et al. 2011).

In the $(\text{Mn}, \text{Co})_3\text{O}_4$ spinel coating on Crofer 22 APU, the $\text{Mn}_{1+\delta}\text{Co}_{2-\delta}\text{O}_4$ spinels ($\delta=0.3-0.9$) exhibiting a dual phase structure at room temperature undergoes a cubic-tetragonal spinel phase transformation during heat treatment. The phase transformation of $\text{Mn}_{1.5}\text{Co}_{1.5}\text{O}_4$ spinel coating from cubic to tetragonal at 400 °C was confirmed by XRD, which showed a negligible effect on the thermal expansion of the coating (Yang et al. 2007). MCF is an interesting candidate material for diffusion barrier coating as it exhibits a self-healing effect, and subsequent densification of the coating during annealing is chromium mitigation in the SOFC stack operation. The $(\text{Mn}, \text{Co}, \text{Fe})_3\text{O}_4$ spinel configuration of the powder is transformed into $(\text{Mn}, \text{Co}, \text{Fe})\text{O}$ rock salt configuration in the as-sprayed coating. The $\text{Mn}_{1.0}\text{Co}_{1.9}\text{Fe}_{0.1}\text{O}_4$ coating on Crofer steel exhibited a complete phase transformation from cubic to spinel phase during annealing at 850 °C for 100 h. This phase transformation leads to a volume expansion in the coating, which helps to close the cracks, also called crack-healing. The increase in annealing time influenced the two-phase regions (major simple cubic and spinel) observed in the as-sprayed condition leading to the formation of a single $(\text{Mn}, \text{Co}, \text{Fe})_3\text{O}_4$ spinel phase (Grünwald et al. 2017; Vaßen et al. 2016). In these studies, conventional techniques like SEM-EDS and XRD were used to study the oxidation behavior of the coatings.

However, the effect of plasma-sprayed MCF coating on the oxidation kinetics of the Crofer substrate has not been studied. No information is available about the effect of crack healing on other electrical properties of MCF coating for a prolonged period of high-temperature exposure. Particularly, the effect of coating on the oxidation resistance of the Crofer substrate with the help of advanced analytical techniques such as GD-OES, Raman spectroscopy, and UV-vis-NIR would bring more insight into the understanding of the oxidation resistance of such overlay coatings. Besides, these tools combined with conventional FE-SEM (EDS) can be complemented for better understanding, which has not been reported earlier.

3. SCOPE AND OBJECTIVES OF PRESENT WORK

From the literature survey, it is observed that Cr poisoning is a major drawback of metallic interconnect. To overcome this issue, protective coatings by APS are being extensively used. Different coatings such as nitride, perovskite (LaCrO_3), spinels ($\text{Mn}_{1.5}\text{Co}_{1.5}\text{O}_4$, MnCr_2O_4 , $(\text{Mn},\text{Co})_3\text{O}_4$, $\text{MnCo}_{1.8}\text{Fe}_{0.2}\text{O}_4$, $\text{Cu}_{1.3}\text{Mn}_{1.7}\text{O}_4$ CuFe_2O_4) have been studied extensively. Amongst all the coatings studied to date, spinel coatings have shown to be the most effective coating to suppress the evaporation of Cr. The study of MCF coating on Crofer 22 APU has been less explored. To our knowledge, not much work is done in characterizing MCF coating, and also the short and long-term oxidation behaviour of the coating has to be investigated.

3.1. Research gap

- Fundamental research activity has been carried out on Crofer 22 APU to a large extent, but research on APS coated MCF on Crofer steel has been limited.
- However, fundamental characterization of MCF coated Crofer steel, like in-situ high temperature XRD, thermal expansion characteristics, adhesion strength, and oxidation mechanism using in-situ XRD, GIXRD, and GDOES are not seen in the open literature.

The overall aim of this research work is to study the short, and long-term oxidation mechanism of $\text{Mn}_{1.0}\text{Co}_{1.9}\text{Fe}_{0.1}\text{O}_4$ (MCF) coated Crofer 22 APU and to evaluate the mechanical and electrical properties. The $\text{Mn}_{1.0}\text{Co}_{1.9}\text{Fe}_{0.1}\text{O}_4$ formulation used as the coating material provides a protective coating on the Crofer steel SOFC interconnect. The MCF powder coated by Atmospheric Plasma Spraying (APS) on interconnect material demonstrated a dense structure and self-healing phenomena of microcracks during annealing under oxidizing atmospheres. The MCF coating has also lowered the degradation rates in SOFC stack operation. The $\text{Mn}_{1.0}\text{Co}_{1.9}\text{Fe}_{0.1}\text{O}_4$ spinel powder has also demonstrated the decomposition of the spinel phase to the cubic structure during plasma spraying and transition to the spinel phase upon annealing. Also, spinels are shown to provide good electrical conductivity, which is beneficial for SOFC stack operation.

3.2. Proposed objectives

1. To study and analyze the Crofer 22 APU substrate microstructure and its $Mn_{1.0}Co_{1.9}Fe_{0.1}O_4$ (MCF) protective coating deposited by Atmospheric Plasma Spray (APS) by using FE-SEM.
2. To evaluate the adhesion strength and electrical conductivity of $Mn_{1.0}Co_{1.9}Fe_{0.1}O_4$ (MCF) coating by Scratch Indentation Testing and Impedance Analyzer, respectively.
3. To examine the short-term oxidation and thermal expansion characteristics of Crofer 22 APU substrate and $Mn_{1.0}Co_{1.9}Fe_{0.1}O_4$ (MCF) coated substrate using in-situ high-temperature XRD.
4. To study the long-term oxidation behavior of the uncoated and coated Crofer 22 APU steel at 850 °C in ex-situ atmospheric conditions.
5. To understand the short-term and long-term oxidation mechanism of uncoated and coated Crofer steel using GIXRD, FE-SEM, DSC, TGA, GDOES, Raman Spectroscopy, and UV-vis-NIR.

4. MATERIALS AND METHODS

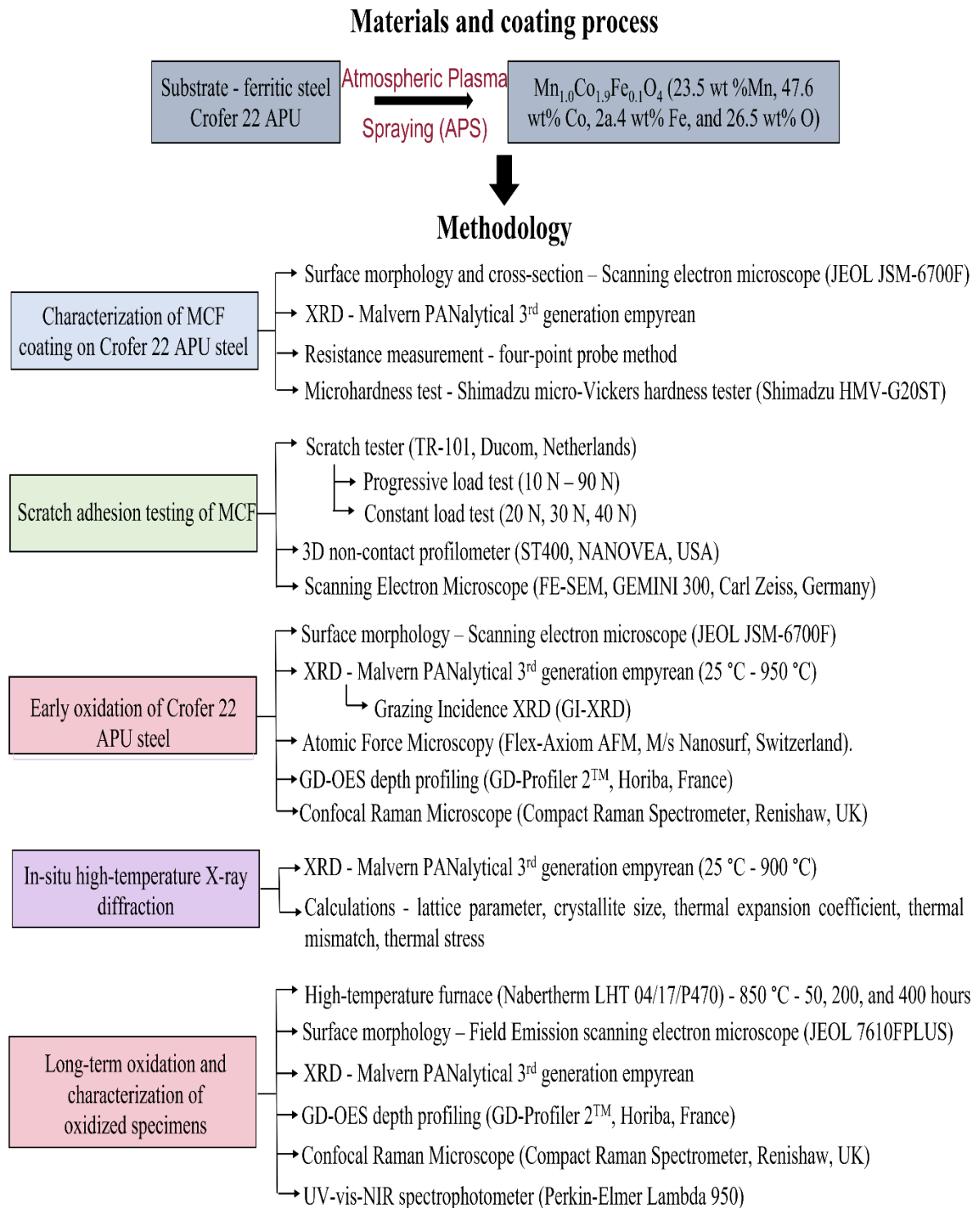


Figure 16: Flow chart showing the proposed methodology

4.1. Materials and coating process

The substrate material used for the plasma spray is ferritic steel Crofer 22 APU (ThyssenKrupp VDM GmbH, Werdohl, Germany). In order to obtain a realistic SOFC stack condition, the substrates will be laser cut to provide a linear channel structure similar to the original interconnect component. The substrate will then be sandblasted with F150 alumina particles of size 60-105 μm . A manganese-cobalt-iron oxide powder having a spinel structure (H.C. Starck, Laufenburg, Germany) is used for the coating. The chemical composition of the coating powder was: 23.5 wt.% Mn, 47.6 wt.% Co, 2.4 wt.% Fe, and 26.5 wt.% O (Grünwald et al. 2017, 2019; Vaßen et al. 2016).

Table 1: Composition of Crofer 22 APU

	Cr	Fe	C	Mn	Si	Cu	Al	S	P	Ti	La
Min	20.0			0.3						0.03	0.04
Max	24.0	Bal.	0.03	0.8	0.5	0.5	0.5	0.02	0.05	0.20	0.2

The APS process parameters: applied current: 500 A, power: 49 kW, plasma gases: 50 slpm Ar and 4 slpm, and stand-off distance: 150 mm (Back et al. 2020; Grünwald et al. 2017; Vaßen et al. 2016).

4.2. Methodology

4.2.1. Characterization of MCF coating on Crofer 22 APU steel

The surface morphology of the as-deposited coating was using a scanning electron microscope (JEOL JSM-6700F). The MCF-coated Crofer steel was then polished for cross-sectional analysis. The coating thickness and porosity levels were assessed from the analysis of the cross-section images using ImageJ (version 1.53t) (Rueden et al. 2017). The coating thickness was measured at five different locations in the cross-section of the ridge/groove and side walls. The porosity was measured at three locations with the same area considered for measurement on the ridge/groove and side surface.

The diffraction patterns were collected using Cu-K α ($\lambda = 1.540 \text{ \AA}$) radiation at 45 V and 40 A in Malvern PANalytical 3rd generation empyrean XRD machine. The parameters for scanning: scan angle - 30° to 90°, scan step size - 0.0262606°, time per step - 67.065 s. "High Score Plus Software (version 5.0)" attached to the system was used for analyzing the XRD patterns, and the phases were identified using the standard Crystallographic Open Database (COD) and Powder Diffraction File (PDF-2) of the International Centre for Diffraction Data (ICDD).

The resistance of as-sprayed MCF-coated Crofer steel was measured using a four-point probe method. The measurements were recorded at room temperature, 50, 100, 150, and 200 °C. As the heating was limited to 200 °C temperature, the data were extrapolated using exponential-curve fitting up to 850 °C, which is the typical operating temperature for SOFCs.

A microhardness test was carried out on the polished cross-section of the MCF-coated Crofer steel interconnect using a Shimadzu micro-Vickers hardness tester (Shimadzu HMV-G20ST). Indentations were made at 0.01 N (100 g) load with a dwell time of 15 s. The micro-hardness at different places of the interconnect groove was estimated using: $V = 1.854 (F/d^2)$ (Tiegel et al. 2015), where F is the load and d is the mean penetrated diameter.

4.2.2. Scratch adhesion testing

A scratch tester (TR-101, Ducom, Netherlands) was used to carry out constant and progressive load tests with a Rockwell C-type diamond conical indenter tip radius of 200 μm and an apex angle of 120°. A load was applied at a constant speed by the indenter on the test specimen and the scratch path was created by the continuous sliding movement of the indenter against the specimen surface. The scratch testing on the coating was performed in progressive and constant loading conditions. The scratch testing conditions and parameters are provided in Table 2 and Table 3. The changes in friction force, coefficient of friction (COF), and acoustic emissions were continuously recorded. Based on the outcome of the progressive load test, parameters for the constant load scratch test were decided. The experiment was carried out in the same conditions three times for repeatability, and the standard deviations of the critical load, stroke length, friction force, and COF at coating failure were calculated.

Table 2: Testing conditions of progressive load scratch test

Parameter	Value
Initial load, N	10
Final load, N	90
Rate of load increase, N/s	0.89
Scratch indenter velocity, mm/sec	0.1
Stroke length, mm	9

Table 3: Testing conditions of constant load scratch test

Parameter	Value
Constant loads, N	20, 30, 40
Scratch indenter velocity, mm/sec	0.1
Stroke length, mm	5

The coated substrates were characterized using a 3D non-contact profilometer (ST400, NANOVEA, USA) before and after the scratch test. A high-speed sensor of 110 μm resolution was used for the scan. The step size for the scan was kept constant at 5 μm . The average surface roughness, 2D and 3D surface texture, and depth profile were evaluated. The EUR15178N standard was used for roughness characterization in three dimensions. A Scanning Electron Microscope (FE-SEM, GEMINI 300, Carl Zeiss, Germany) was used to characterize the cross-section, surface morphology, pre- and post-scratch test analysis.

4.2.3. Early oxidation of Crofer 22 APU steel

The X-ray diffraction (XRD) patterns were measured using Malvern PANalytical 3rd generation empyrean XRD machine using Cu-K α ($\lambda = 1.540 \text{ \AA}$) radiation at 45 V and 40 A. The Crofer 22 APU steel specimen was cut into a 10 mm \times 10 mm piece. The thickness of the specimen was reduced to 0.5 mm using SiC polishing papers. The specimen was placed in the high temperature (HTK) stage, and a vacuum was created, maintaining a vacuum pressure of 10^{-4} mbar. The Crofer steel was heated from 25 $^{\circ}\text{C}$ to 950 $^{\circ}\text{C}$ using a Pt strip. The heating rate was 60 $^{\circ}\text{C}/\text{min}$, and the temperature increased to 950 $^{\circ}\text{C}$ in steps of 100 $^{\circ}\text{C}$ with 30 minutes of holding time at each stage. The specimen was scanned from 20 $^{\circ}$ to 100 $^{\circ}$ using a scan step size of 0.0262606 $^{\circ}$ and the time per step was 36.465 seconds. The XRD patterns were analyzed using the "High Score Plus Software" attached to the system, and the phases were identified using the standard Crystallographic Open Database (COD) and Powder Diffraction File (PDF-2) of the International Centre for Diffraction Data (ICDD).

The surface morphology of the Crofer 22 APU before and after in-situ oxidation was recorded using Jeol JSM-6700F to investigate the morphological changes. The surface of the Crofer steel after in-situ oxidation was characterized to investigate the formation of oxide layers. As the oxides formed on the surface were thin, it was difficult to detect in conventional XRD. GI-XRD was used to study and analyze the phases and oxides formed.

The GI-XRD parameters: a scan step size of 0.04° , 1.76 seconds/step, and an omega value of 1 was chosen for the scan.

The surface topography and roughness of the Crofer steel before and after oxidation were investigated by Atomic Force Microscopy (Flex-Axiom AFM, M/s Nanosurf, Switzerland). The AFM tip used for this measurement was a Tapping Mode cantilever made of silicon nitride. The scan rate and area were 1 Hz and $2\ \mu\text{m} \times 2\ \mu\text{m}$, respectively.

The GD-OES depth profiling (GD-Profilier 2TM, Horiba, France) was carried out using a 2mm diameter anode. The Crofer steel sample was loaded into the GD-OES system, and the air between the sample and the anode was flushed with argon gas for 105 s. The GD-OES was performed using an RF generator with plasma conditions: argon gas pressure of 650 Pa and power of 15 W. The depth profiling was performed to a depth till the stabilization of alloying elements. It was $3\ \mu\text{m}$ and $8\ \mu\text{m}$ before and after oxidation samples. A Confocal Raman Microscope (Compact Raman Spectrometer, Renishaw, UK) was used to detect oxide levels at a wavelength of 532 nm in the spectral range of $100\text{-}1000\ \text{cm}^{-1}$ with an exposure time of 10 s.

4.2.4. Thermal expansion mismatch of MCF coated Crofer 22 APU metallic interconnect

The microstructures of Crofer 22 APU and MCF coated steel specimens before in-situ heating were studied using FE-SEM. Crofer steel and MCF coated steel diffraction patterns were obtained using Malvern PANalytical (3rd generation empyrean) XRD machine. The MCF-coated Crofer steel substrate was cut into two pieces. The coated surface and substrate surface were exposed to X-ray incidence independently at the high-temperature stage using two pieces of the specimen cut from the same condition. The specimen was placed in a high temperature (HTK) stage (Anton Paar, Pt strip crucible), and a vacuum with a pressure of 10^{-4} mbar was created inside the HTK chamber. The incidence beam was Cu-K α ($\lambda = 1.540\ \text{\AA}$) radiation at 45 V and 40 A. The specimen was heated from $25\ ^\circ\text{C}$ to $900\ ^\circ\text{C}$ at a heating rate of $60\ ^\circ\text{C}/\text{min}$. The stability was created by holding the specimen for 15 minutes at each temperature. The diffraction patterns for Crofer 22 APU and MCF coating were recorded at $25\ ^\circ\text{C}$ and 300 to $900\ ^\circ\text{C}$ with a step of $100\ ^\circ\text{C}$. The specimen was scanned from 30° to 90° with a scan step size of 0.0262606° . High Score Plus Software (version 5.1) attached to the system was used to analyze the XRD pattern, and phase identification was made using the standard Crystallographic Open Database (COD) and

Powder Diffraction File (PDF-2) of the International Centre for Diffraction Data (ICDD). The lattice parameter, crystallite size, and thermal expansion coefficient for every temperature were evaluated, and the mismatch between substrate and coating was investigated.

4.2.5. Long-term oxidation and characterization of oxidized specimens

A table-top high-temperature furnace (Nabertherm LHT 04/17/P470) was used for the oxidation process. The specimens were heated from room temperature to 850 °C at a heating rate of 10 °C/min and heated isothermally for 50, 200, and 400 hours. The oxidation process was carried out in normal/standard atmospheric condition. The specimens were weighed on a high precision weight balance (Contech CAH-223) before placing them in the furnace and weighed again after every oxidation interval to calculate the weight gain on the sample.

The microstructures and elemental analysis of Crofer 22 APU and MCF-coated steel after oxidation were studied using FE-SEM. The cross-section of the oxidized samples was characterized for oxide formation and to evaluate oxide layer thickness. Subsequently, to assess the porosity levels after each oxidation stage, the cross-section images were used for analysis using the image processing software ImageJ (version 1.53t) (Rueden et al. 2017). The porosity measurements were performed at different locations in the cross-section image, and the standard deviation was calculated.

The X-ray diffraction (XRD) patterns were measured using Malvern PANalytical 3rd generation empyrean XRD machine using Cu-K α ($\lambda = 1.540 \text{ \AA}$) radiation at 45 V and 40 A. The oxidized Crofer steel and MCF coating were scanned from 20° to 80° using a scan step size of 0.026° and the time per step was 42.55 seconds. The XRD patterns were analyzed using the "High Score Plus Software" attached to the system, and the phases were identified using the standard Crystallographic Open Database (COD) and Powder Diffraction File (PDF-2) of the International Centre for Diffraction Data (ICDD). A Rietveld refinement was carried out to estimate the change in lattice parameters and quantification of phases and oxides.

The GD-OES depth profiling (GD-Profiler 2TM, Horiba, France) was carried out on the oxidized Crofer steel using a 2 mm diameter anode. The oxidized sample was loaded into the GD-OES system, and argon gas was purged to flush the air between the sample and the anode for 105 s. An RF generator with a plasma condition of 650 Pa argon gas pressure

and 15 W power was used for the measurements. Depth profiling was performed on the samples till the alloying elements were stabilized.

A Confocal Raman Microscope (Compact Raman Spectrometer, Renishaw, U.K.) was used to detect the oxide levels. Raman data were collected on excitation at the wavelength of 532 nm in the spectral range of 100-800 cm^{-1} with an exposure time of 10 s. The absorbance spectra of as-sprayed and oxidized MCF coating were measured using a UV-vis-NIR spectrophotometer (Perkin-Elmer Lambda 950) equipped with an integrating sphere of 150 mm. The reflectance and absorbance measurements were performed wavelength range of 190-850 nm.

5. RESULTS AND DISCUSSION

5.1. Characterization of plasma sprayed $Mn_{1.0}Co_{1.9}Fe_{0.1}O_4$ coating on Crofer 22 APU ferritic stainless steel used for solid oxide fuel cell interconnect

5.1.1. FESEM and XRD analysis

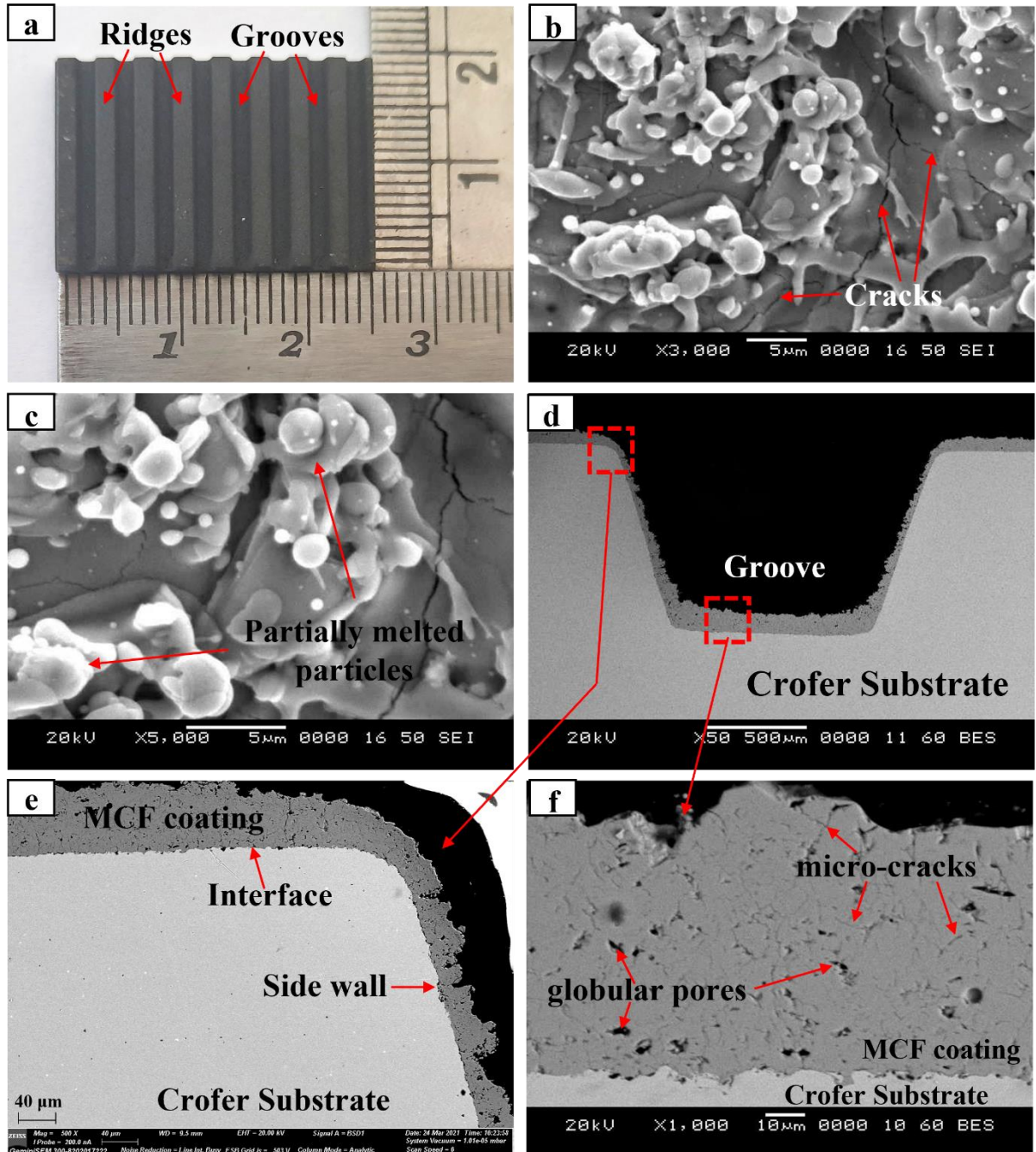


Figure 17: (a) Macro image of MCF coating on Crofer 22 APU steel interconnect with rectangular gas flow channels, (b), (c) Surface morphology of coating, (d), (e), (f) cross-section image of the MCF-coated Crofer steel at different magnifications.

Figure 17a shows the macro-image of the Crofer steel interconnect coated with MCF. The laser-cut linear rectangular channel structure of the interconnect can be observed with alternate ridges and grooves. The channels enable the gas flow (typically hydrogen fuel in SOFC) to induce the chemical reaction at the anode side. The surface morphology of the as-sprayed MCF coating is shown in Fig. 17 b and c. The morphology shows unmolten and partially melted particles, usually an inherent defect in coatings produced by the atmospheric plasma spray process (N. Manjunath and B. Rajasekaran, 2022). The surface morphology indicates rapid solidification of the coating powder during atmospheric plasma spraying displaying flashy and rough surfaces (Back et al. 2020). Cracks on the surface of the coating are also visible. The back scattered cross-section analysis of the MCF-coated Crofer steel (Fig. 17 e and f) show a varied uniformity in the coating thickness on side walls compared to flat surfaces. The side walls of the metallic interconnect have a non-uniform thickness, whereas the thickness is uniform on the flat surfaces.

It should be noted that the deposition of thermal spray coating on the substrate surface is perpendicular to the plasma plume than the parallel surfaces (side surfaces). The TriplexPro210 gun enables coating at the side surfaces of the metallic interconnects with non-uniform coating thickness. The probability of the molten MCF splats hitting the perpendicular surface is more than at the side wall, irrespective of the thermal spray variant. However, the adhesion of the coating was found to be adequate and intact in the cross-section images. As shown in Fig. 17f, the coating showed typical plasma sprayed microstructure characterized by microcracks and globular porosity. The standard deviation of the porosity at different regions on ridges/grooves was 10.93 ± 1.323 %. The porosity of the coating on the side walls was found to be 10.3 ± 0.4 %. The coating thickness ranged between 60 and 80 μm on the ridges/grooves and the thickness range of 20-50 μm on the side walls. Chromium will also evaporate from the side walls upon high temperature exposure. So, the coating is equally important on the side walls of the interconnects.

Figure 18 and Table 4 show the spot and area EDS data of the elemental composition in as-sprayed MCF coating. The weight percentages of Mn, Co, Fe, and O were found to comply with the nominal composition of the coating powder used as feedstock for the deposition process. The deviation in the chemical composition of the as-deposited coating may be attributed to the decomposition of the feedstock in the plasma plume or during the rapid solidification. However, the as-deposited coating was found to be chemically homogeneous in the cross-sections and the marginal deviations can be attributed to the fully molten and

partially molten splats. In as-sprayed conditions, CoO is the primary phase confirmed by the highest weight percentage of Co in the coating.

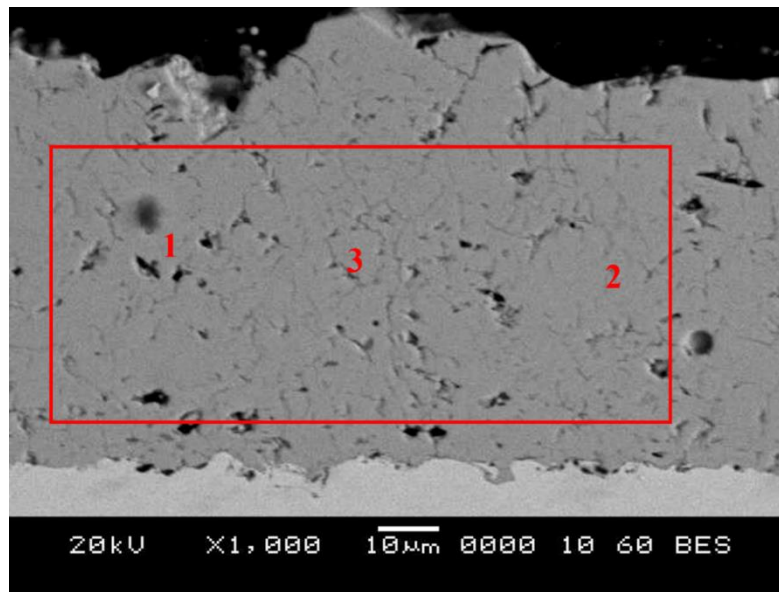


Figure 18: EDS spot and area analysis of a cross-section of MCF-coated Crofer steel

Table 4: EDS spot and area analysis from Fig. 18

Location	Elements (wt.%)			
	Mn	Co	Fe	O
Spot 1	28.5	55.7	3.1	12.6
Spot 2	28.9	58.4	2.9	9.7
Spot 3	31.7	55.2	2.9	10.1
Selected Area	29.4	57.8	2.9	9.9

Phase analyses by x-ray diffraction of as-received Crofer steel and as-sprayed MCF coating are given in Fig. 19. The XRD patterns of the Crofer steel revealed α -Fe with cubic structure as the major phase. Though the chromia layer is readily formed on the steels, it was not detected in the normal XRD. The XRD analysis of MCF coating revealed CoO with cubic structure as the major phase. The lattice parameters, crystallite size, and micro-strain are detailed in table 5.

The Crystallite size of the Crofer steel and MCF coating was measured using the Debye-Scherrer equation. The measurements were performed with instrument-corrected profile fitting using SiO₂ standards. The Debye-Scherrer equation for crystallite size is given by (Khorsand Zak et al. 2011):

$$D = K\lambda/\beta\cos\theta \dots\dots\dots(8)$$

where D is the crystallite size, λ is the x-ray wavelength, θ is the diffraction angle, β_D is full width at half maximum intensity, and K is Scherrer constant (0.89).

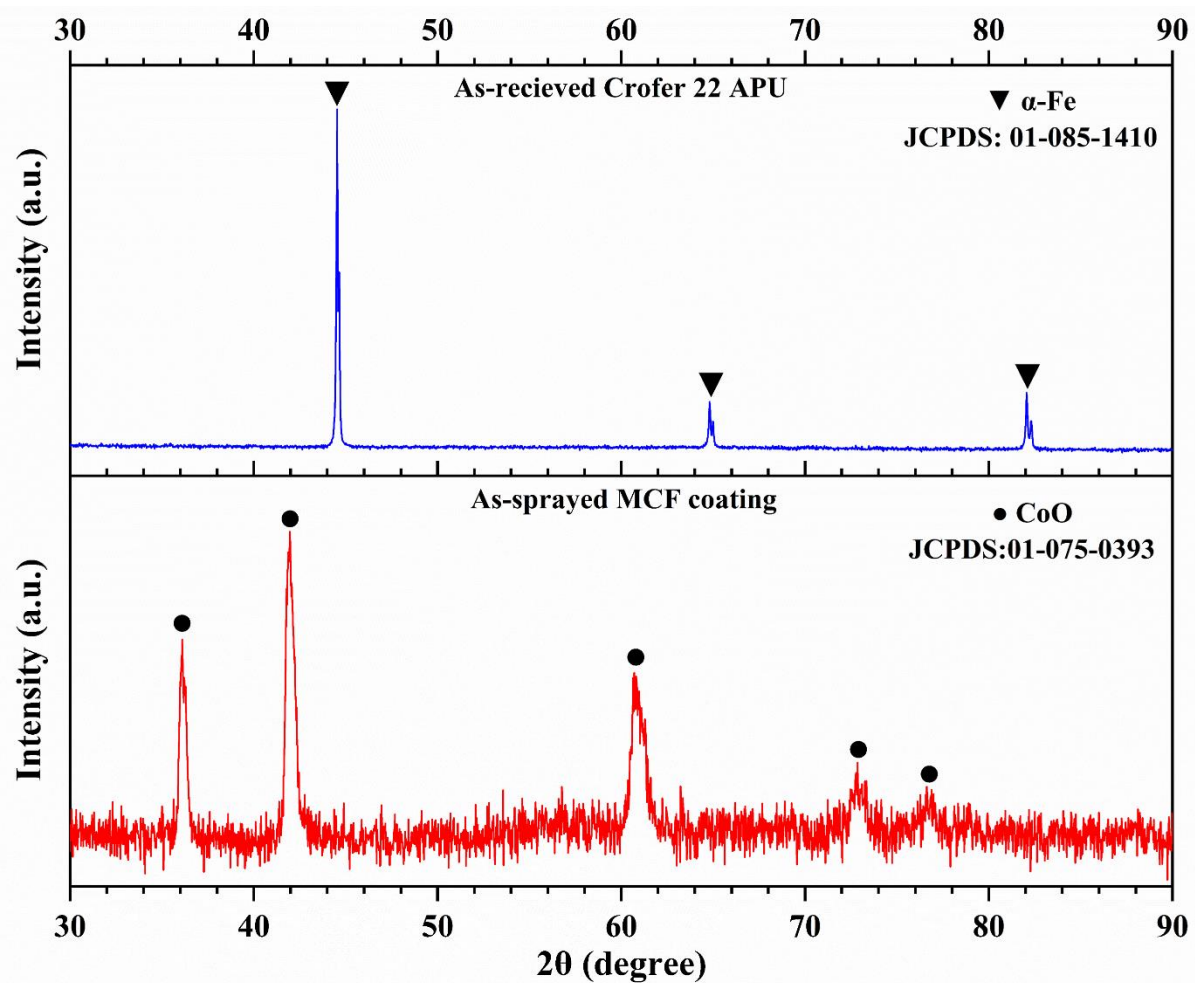


Figure 19: XRD patterns of as-received Crofer 22 APU steel (top) and as-sprayed MCF coating (bottom)

Table 5: Lattice parameter, crystallite size, and micro-strain of as-received Crofer 22 APU steel and as-sprayed MCF coating

Material	Lattice parameter (Å)	Crystallite size (Å)	Micro-strain (%)
Crofer 22 APU	2.866	468	0.271
MCF coating	4.258	224	0.563

In the as-sprayed MCF coating, the cross-section EDS analysis (Table 5) and X-ray diffraction patterns (Fig. 19) reveal the spinel configured $(\text{Mn, Co, Fe})_3\text{O}_4$ powder transformed to $(\text{Mn, Co, Fe})\text{O}$, which has rock salt structure (Grünwald et al. 2017). The MCF coating can be considered as Mn-Co-O due to the very low content of Fe (Back et al. 2020). Therefore, the CoO with cubic rock salt structure has been identified as the major

phase. The stability of the rock salt phase was seen only at high temperatures, as studied by the phase diagram of the Mn-Co system (Aukrust and Muan 1963). Due to the fast cooling of the (Mn, Co, Fe)₃O₄ spinel powder during plasma spraying on the cold Crofer steel substrate, the deposited MCF coating has a metastable rock salt configuration. This rapid cooling from the molten state did not provide adequate time to recover from the cubic spinel phase. The XRD analysis of the as-sprayed MCF coating exhibited a simple cubic phase of CoO and a considerable amount of Fe_{3-x}O₄ phase. This phase was regarded as Co instead of Fe due to the highest weight percentage of Co in coating powder (Vaßen et al. 2016). The globular pores, amounting to about 11% porosity, develop from improper volume filling during the plasma spraying, leading to gas entrapments (Back et al. 2020).

5.1.2. Micro-hardness

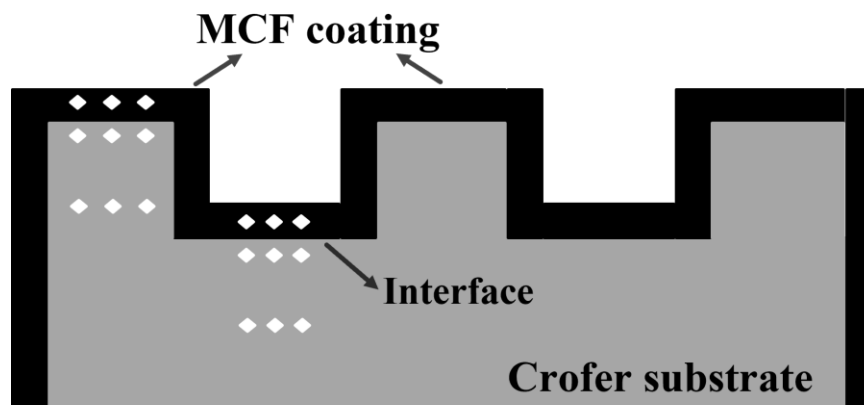


Figure 20: Schematic showing locations for micro-hardness measurements

The micro-hardness was measured on the substrate, coating, and adjacent to the coating-substrate interface. The schematic of the locations used for micro-hardness measurements is shown in Fig. 20. The parallel ridge/groove cross-section of the coated interconnect was used for the measurements. The measured values are detailed in Table 6. The micro-hardness of the Crofer substrate varies in the range of $112 \pm 6 \text{ HV}_{0.1 \text{ N}}$, and the values near the coating-substrate interface increase to $128 \pm 8 \text{ HV}_{0.1 \text{ N}}$. The MCF coating had the highest hardness value ($163.5 \pm 1.5 \text{ HV}_{0.1 \text{ N}}$), and a good repeatability of the measurements was seen for the coating. The hardness value of the coating-substrate interface lies in between coating and substrate values measured individually. This indicates a strong metallic interlocking at the Crofer substrate and MCF coating interface (Chawla 2012). In addition, no interfacial delamination between the ceramic coating and metallic substrate was noticed when the microhardness test was performed nearer to the interface. A similar trend was

observed in the silicate glass ceramic micro-hardness study on Crofer 22 APU (Sharma and Singh 2019).

Table 6: Hardness values of Crofer 22 APU, coating-substrate interface, and MCF coating in as-sprayed conditions

Hardness (HV _{0.1N})		
As-received Crofer 22 APU	Interface	As-sprayed MCF coating
106	120	162
113	136	163
118	128	165

5.1.3. Resistance of as-sprayed MCF coating as a function of temperature

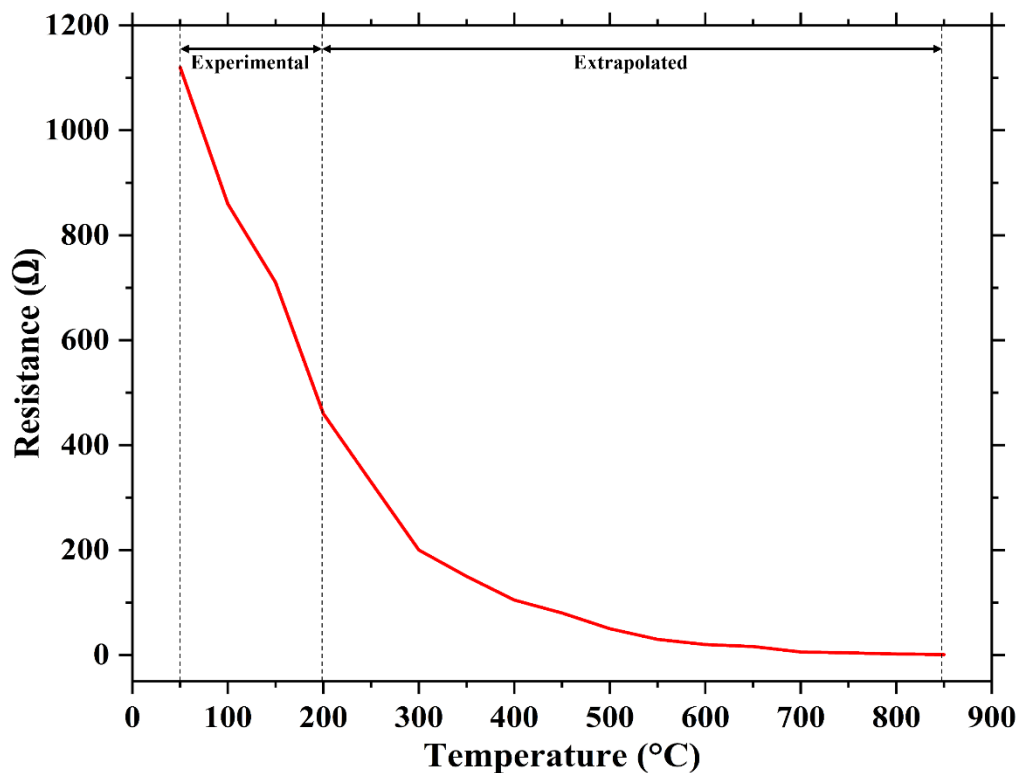


Figure 21: Graph of resistance of as-sprayed MCF coating as a function of temperature

Figure 21 represents the graph of resistance of MCF coating as a function of temperature. A substantial drop in resistance can be seen with increasing temperature. This indicates that the MCF coating on the interconnect is suitable coating material for conduction at high temperatures. In Fig. 21, a drastic initial decrease in the resistance of the MCF-coated steel can be seen. E. Ruiz-Trejo. et al. made similar observations (Ruiz-Trejo et al. 2015). The time required for the resistivity of spinels to reach a saturation value is substantially less,

where no or very little change in resistivity is seen during annealing at 850 °C. This indicates that MCF powder has good sintering activity at lower temperatures (Megel et al. 2011). Mn-Co spinel protective coatings application ferritic steels showed a reduced contact resistance and mitigated the chromium transport at the cathode side (Alvarez et al. 2011). The doping of Fe, Ti, and Cu in Mn-Co spinel powder has shown higher enhanced electrical conductivity (Chen et al. 2005; Montero et al. 2008; Wang et al. 2011). The AISI-SAE 430 stainless steel dip coated with Y, Co, and Y/Co-containing precursor using the sol-gel technique demonstrated a higher conductivity with the presence of Co-containing spinel phases (Qu et al. 2006). The transfer of ions among cations in the octahedral voids and the availability of various valence states between octahedral cations have enhanced the conductivity in MCF spinel. The MCF-coated Crofer 22 APU shows a reduction in the ASR value due to the formation of the MnCoCrO_4 spinel phase, where the electrical conductivity increases by two orders of magnitude compared to Cr_2O_3 . The MCF coating increases the electrical conductivity, acts as a diffusion barrier, and mitigates the Cr cations migration, improving the cell's performance (Miguel-Pérez et al. 2013). The MCF has been designed to sustain the good electrical conductivity of Crofer 22 APU even at the high operating temperature of SOFCs. It should also be noted here that the role of MCF coating is to act as a diffusion barrier coating to mitigate chromium poisoning while sustaining electrical conductivity.

Spinel conduct by hopping charges between octahedral sites and conduction is facilitated by the presence of various valence states among octahedral cations. In the case of Fe_3O_4 , Fe^{3+} occupies the tetrahedral sites and Fe^{2+} and Fe^{3+} ions occupy the octahedral sites equally. As the temperature increases, the hopping or mixing of cations between the sites is caused by the entropy and hence conductivity increases. Similarly, in MnFe_2O_4 , a mixed distribution of cations occurs in the octahedral sites and hopping among the Mn^{2+} , Mn^{3+} , Fe^{2+} , and Fe^{3+} ions on the octahedral sites will also increase the conductivity (Petric and Ling 2007). The conductivity in MnCo_2O_4 spinel is caused by polarons hopping between $\text{Mn}^{3+}/\text{Mn}^{4+}$ and $\text{Co}^{2+}/\text{Co}^{\text{III}}$ on the octahedral sites. As the Mn^{2+} ions are substituted by Co^{2+} ions in the tetrahedral sites, the conduction occurs hopping between $\text{Mn}^{3+}/\text{Mn}^{4+}$ and $\text{Co}^{2+}/\text{Co}^{\text{III}}$ pairs at octahedral sites (Kruk et al. 2020). But for an extensive study on mechanism of conduction in spinels, factors like activation energy and cation distribution on tetrahedral and octahedral sites must be considered (Bordeneuve et al. 2010).

5.2. Mechanical integrity of the $Mn_{1.0}Co_{1.9}Fe_{0.1}O_4$ coating using scratch indentation testing

5.2.1. Surface analysis of as-deposited MCF coating using a 3D non-contact profilometer

Figure 22 shows the 3D surface view of the MCF-coated Crofer 22 APU substrate used for the adhesion test. The coated interconnect has uniformly machined ridges and grooves. The surface topography of a single ridge of coated interconnect is shown in Fig. 23a. An area of $1\text{ mm} \times 6\text{ mm}$ on the coating surface was considered for surface roughness. The surface roughness profile along the area considered for analysis is shown in Fig. 23b. The analysis revealed that the surface roughness varied across the area. The coating was studied by selecting a defined area on the coating as shown in Fig. 24. Fig. 24 (a) shows the 2D view of the surface where the variation of the roughness throughout the surface was observed. The values of the parameters obtained are displayed in Table. 7. The arithmetic mean height or mean surface roughness, S_a , was $6.041\text{ }\mu\text{m}$. Both surface porosity (seen in blue in Fig. 24a) of as-deposited coatings and rapidly solidified splats (seen in red in Fig. 24a) is attributed to the surface roughness.

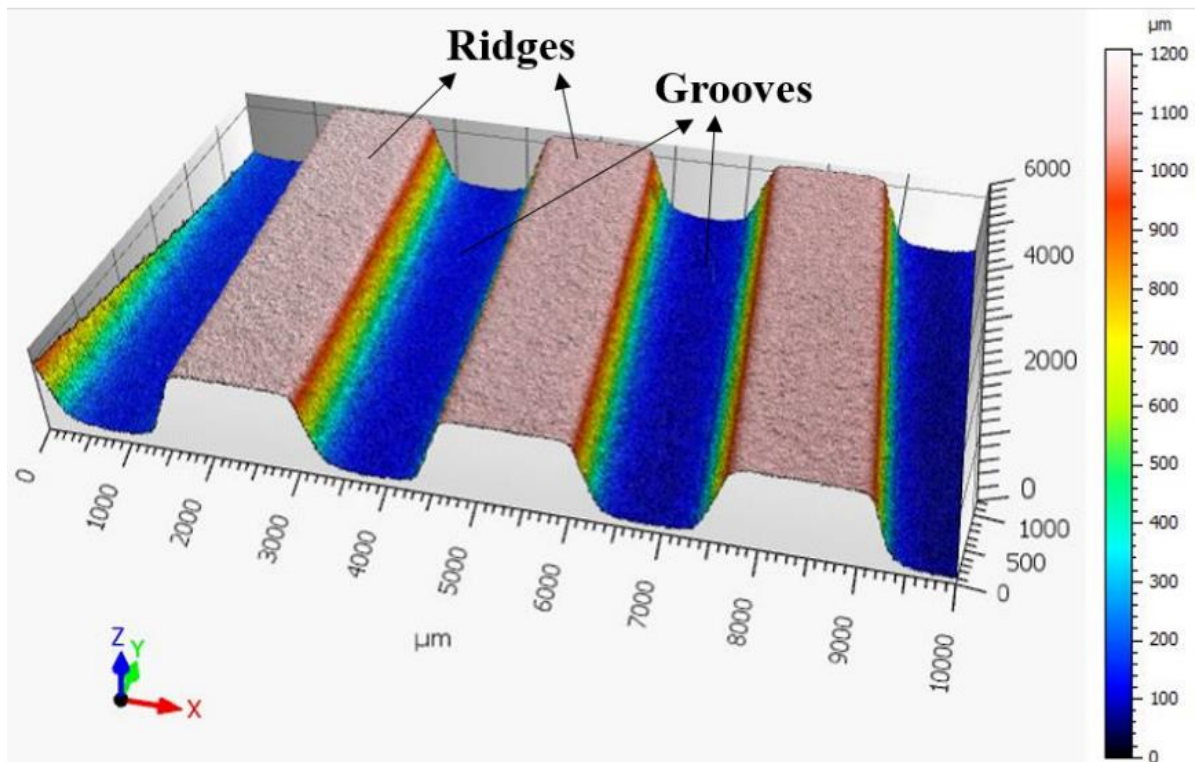


Figure 22: 3D profile of the specimen displaying the surface of the ridges and grooves

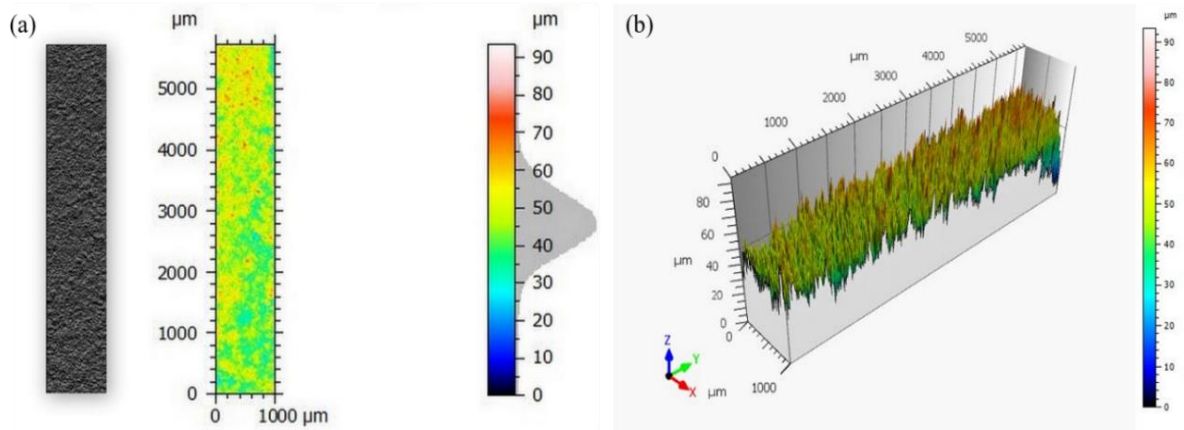


Figure 23: (a) Surface profile of coating depicting depth characteristics, (b) Primary surface profile in 3D for estimating average surface roughness

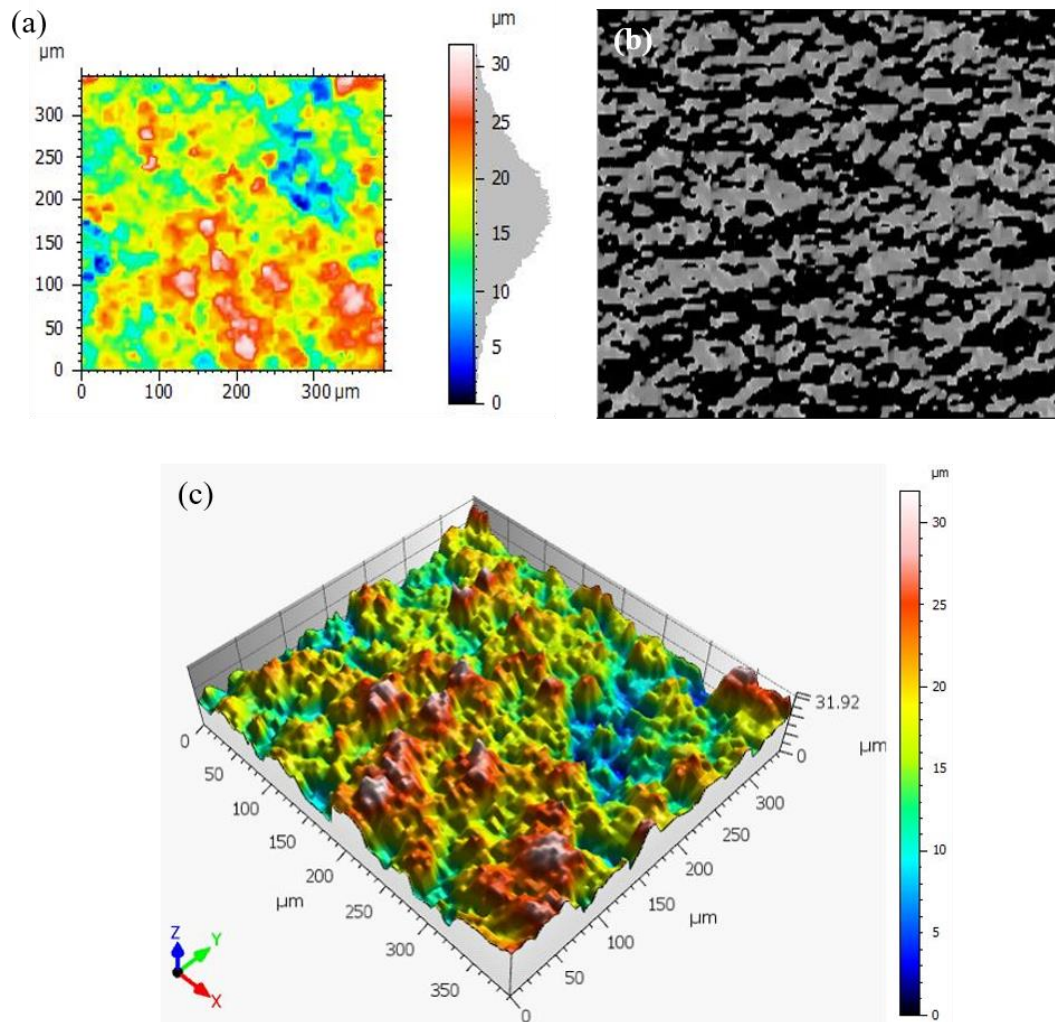


Figure 24: Coating analysis area using a confocal profilometer, (a) selected area of the investigated coating for measuring surface roughness, (b) photo simulation of the coated surface, (c) 3D view of the selected coating area showing variation in roughness

Table 7: Surface profile parameters obtained from a 3D noncontact profilometer before the scratch test

Height Parameters	Value (μm)
Root mean square height, S_q	7.608
Maximum peak height, S_p	47.15
Maximum pit height, S_v	46.21
Maximum height, S_z	93.36
Arithmetic mean height, S_a	6.041

5.2.2. Scratch test

5.2.2.1 Scratch test under progressive loading

The progressive load scratch test was carried out in the load range between 10-90 N. The result is shown in Fig. 25a. The scratch curve clearly depicts the critical load (L_c) value for coating failure where a sudden and predominant change in slope was observed. The sudden increase in friction force and coefficient of friction (COF) at the critical load also indicates the coating failure where the scratch indenter comes in contact with the steel substrate while the MCF coating has been peeled-off. The COF of the coated surface is low compared to the steel surface. The sudden change in slope could be delamination of coating, plastic deformation, cracking in the coating or substrate, etc. (Das et al. 1991; Jaworski et al. 2008; Xie and Hawthorne 1999). In this case, the delamination of the coating was observed at critical load. The critical load may be affected by several intrinsic and extrinsic parameters. Intrinsic parameters include indenter tip radius, loading rate, and scratch speed, and extrinsic parameters including friction coefficient, surface roughness, substrate properties like hardness and elastic modulus, coating properties like hardness, thickness, modulus, residual stress (Steinmann et al. 1987) (Bull and Berasetegui 2006). The penetration depth increased linearly until the critical load was attained. Coating delamination started when a sudden increase in depth of penetration was also observed in the scratch curve. Further increase in the load led to a linear increase in the penetration depth of the indenter. From the progressive scratch test result, the critical load, L_c , was found to be 35.7 N. The corresponding values of friction force and coefficient of friction were 4.501 N and 0.126, respectively.

An in-situ acoustic emission test setup monitored the progressive scratch test. The testing is especially applicable when the adhesion between the substrate and coating is strong enough (Ariharan and Maurya 2021). A sudden change in the acoustic emission signal (indicated in a

dotted red color box in Fig. 25b) resulted from the release of internally stored elastic energy and an indication of crack initiation and complete delamination (Antolino et al. n.d.; Ariharan and Maurya 2021; Boháč et al. 2014; Tomastik et al. 2015). The corresponding load/critical load for failure was around 35N, which was noticed during the progressive load test in Fig. 25a.

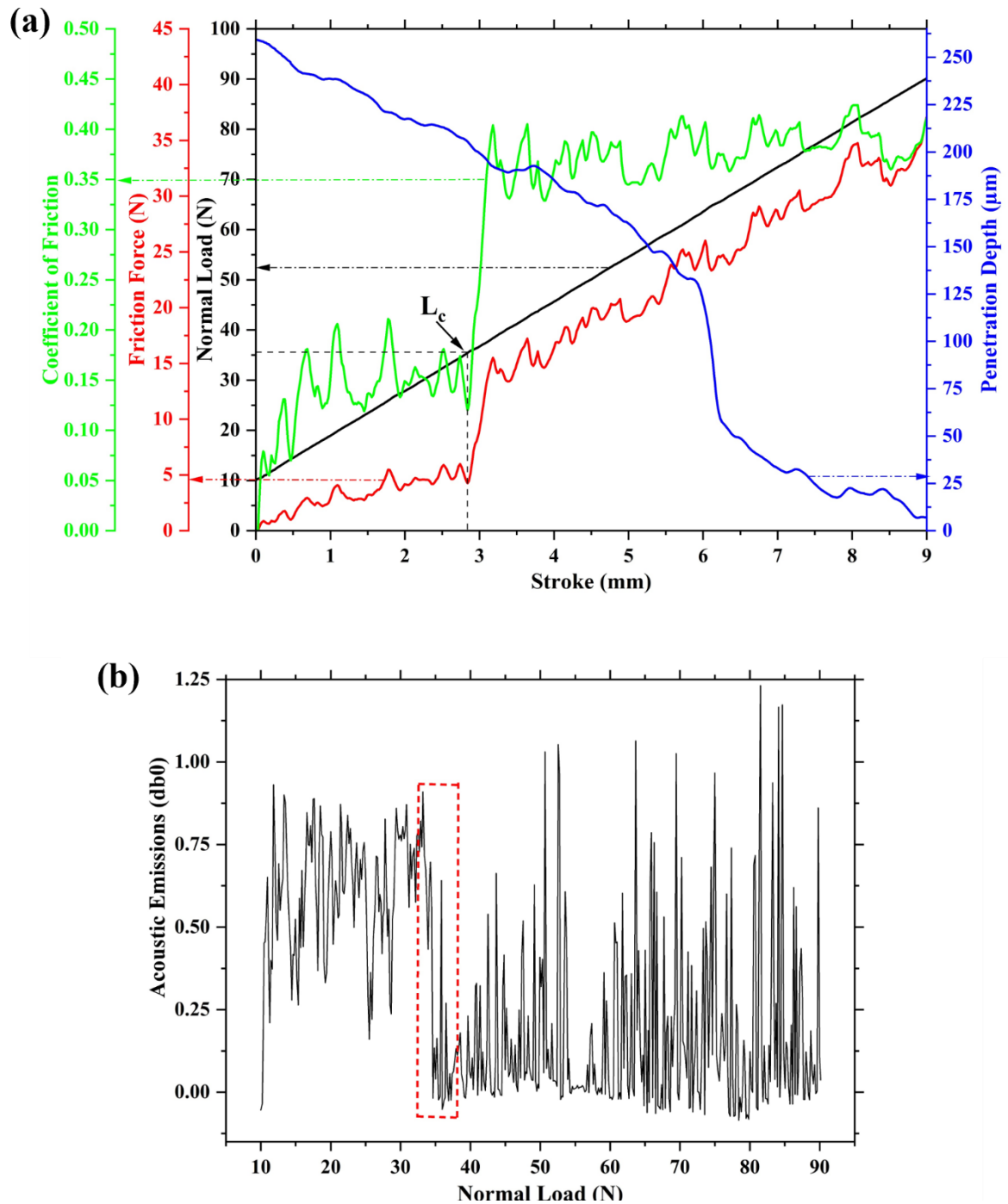


Figure 25: (a) Scratch curve plotted for progressive scratch testing, (b) Acoustic Emission v/s Normal Load (dotted red rectangular box indicating failure of coating)

5.2.2.2 Scratch test under constant loading

The scratch curves for the constant loads of 20 N, 30 N, and 40 N are shown in Fig. 26 a, b, and d, respectively. Based on the results of the progressive load scratch test, the load levels 20 N, 30 N, and 40 N were chosen for the constant load scratch test. As the critical load for coating failure was observed around 35 N, the load levels above and below were also considered. When a constant load of 20 N was applied, a sudden increase in friction force and the COF as the indenter came in contact with the coating surface due to the tangential force acting on the specimen, as shown in Fig. 26a. As the test advances at the same load, a friction force and COF saturation is attained. But the increase in penetration depth is linear throughout the experiment; however, no coating delamination was noticed. The coating was intact and sustained a load of 20 N throughout the entire stroke length. The scratch curve for 30 N constant load is shown in Fig. 26b. The sudden increase of initial friction force and COF was observed at the beginning of the test, and not much variation was noticed until the failure. The penetration depth was observed to increase gradually. A sharp increase in friction force and COF was observed after a stroke of about 3.5 mm, due to the partial peel-off of the coating. Similarly, penetration depth also soars up to a larger extent because of the complete delamination of the coating upon a further increase in stroke length. The coating failure can also be noticed from the acoustic emission signal, as shown in Fig. 26c. The critical load/critical stroke length exhibited the most noticeable shift in the acoustic emission signal. The coating failure was abrasion mode at the beginning of the scratch test, which shifted to interfacial delamination/peel-off immediately after the critical load to failure had reached. When the coating thickness is relatively small, the change in acoustic signal is highly distinguishable due to abrupt changes in the material removal/wear mechanism. (Antolino et al. n.d.; Ariharan and Maurya 2021; Boháč et al. 2014; Tomastik et al. 2015).

Figure 26d shows an initial increase in penetration depth when the indenter comes in contact with the coating surface for the test carried out at 40 N. Similarly, the friction force and COF increase initially and can be seen to show slight variation as the indenter proceeds on the scratch path. When a constant load of 40 N was applied, the coating was completely delaminated in the initial test stage. The complete delamination indicates that the coating no longer sustains the constant load of 40 N. It should be noted that the applied load is greater than the critical load, which is 35 N, as identified by the progressive load test.

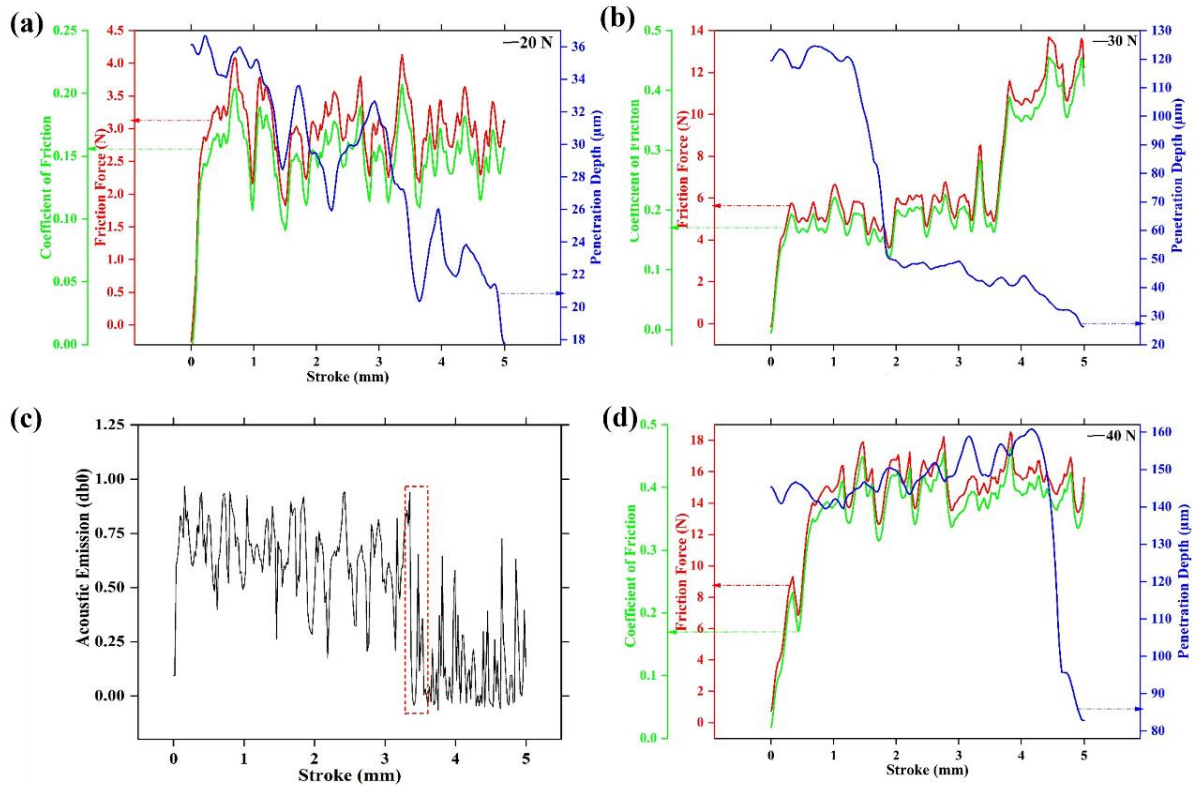


Figure 26: Scratch curves of constant loads, (a) 20 N, (b) 30 N, (d) 40 N, (c) Acoustic Emission vs. Stroke (dotted red rectangular box indicating failure of coating)

5.2.3. Post-test failure analysis by FESEM

5.2.3.1 Progressive load

The FESEM images of the specimen after the progressive load scratch test are shown in Fig. 27 a, b, and c. FESEM images of the scratch path were linear as a function of load and were in good agreement with the result of the progressive load test reflected in the scratch curve (Fig. 25a). The image shows evident coating delamination when the critical load is reached. The brittle mode of failure is observed where the exposed substrate area is significantly large and usually extends beyond the limit of the scratch track. Whereas, in a ductile mode of failure, after the coating delamination, the area of the uncovered substrate is small or restricted within the scratch track. The interfacial de-cohesion and large coating spallation can be observed in Fig. 27b, which implies that either the adhesion is inadequate due to residual stresses in the coating, which are usually tensile (Back et al. 2020). The cracks were observed on the coating surface over a stroke length well before the delamination, as shown in Fig. 27c. These cracks were initiated at the trailing edge of the diamond indenter and are expected to propagate towards the outward direction with speed higher than the indenter. During the scratch test, the cracks are believed to grow to a significant distance on

either side of the scratch path, resulting in a large interfacial flaw. The observed cracks may be caused by the tangential drag between the indenter and substrate due to tensile stresses generated during the slide (Bull 1991). The coating was peeled-off on both sides of the scratch (Fig. 27a). It is also logical that the coating is pushed into the substrate by the indenter (Damage et al. 1989). Subsequent load application induces scratch on the substrate once the entire coating is peeled off. The debris of the coating was also observed in the adjacent areas.

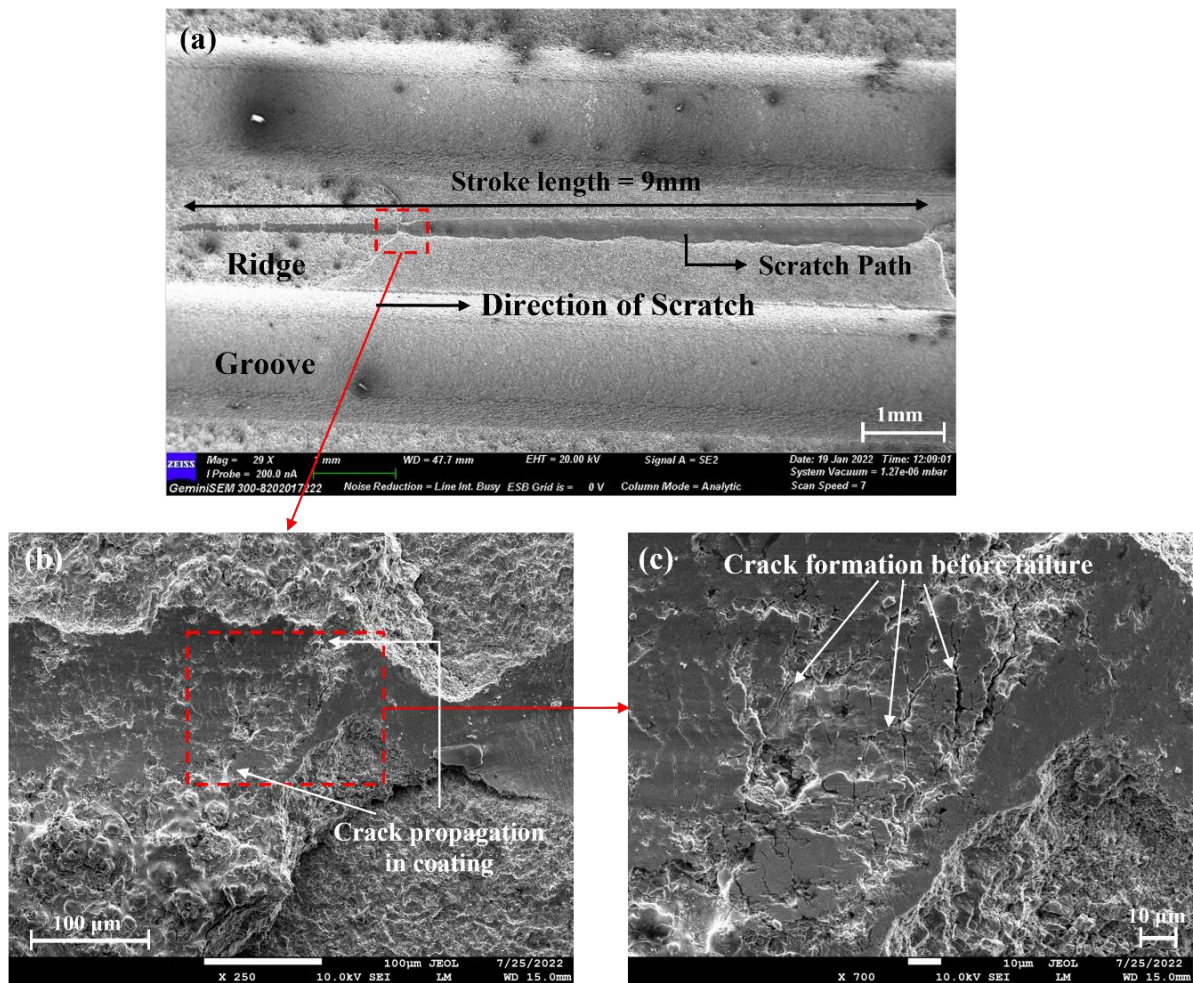


Figure 27: FE-SEM image of progressive load scratch (a) Image covering the overall scratch length (b) magnified image of the area of failure (c) magnified image of the cracks formed before failure

5.2.3.2 Constant load

The constant load scratch tests were carried out for different loads: 20 N, 30 N, and 40 N, for a constant stroke length of 5 mm. Figure 28 shows the FE-SEM images of the constant load of scratch tests. The constant load scratch test using 20 N reveals no delamination of the coating, as shown in Fig. 28a. There were no significant defects in the coating surface, like microcracks formation or alterations, and the coating was completely intact. The constant load

scratch test using 30 N, as shown in Fig. 28b, shows the formation of microcracks at the beginning of the scratch and visible delamination of coating noticed after a stroke length of 3.5 mm. The failure of the coating was due to the formation of the microcracks well before the complete delamination, as revealed by Fig. 28c. These cracks extended beyond the scratch path and propagated into the coating and substrate interface, resulting in complete delamination. The nature of the coating failure at a constant load of 30 N resembled that of failure under progressive loading conditions. The scratch induced by the constant load of 40 N is shown in Fig. 28d. The coating has been delaminated as soon as the indenter comes in contact. It should be noted that the load applied (40 N) is above its critical load (35 N) as observed by the progressive load test; the coating delaminated totally, exposing the substrate.

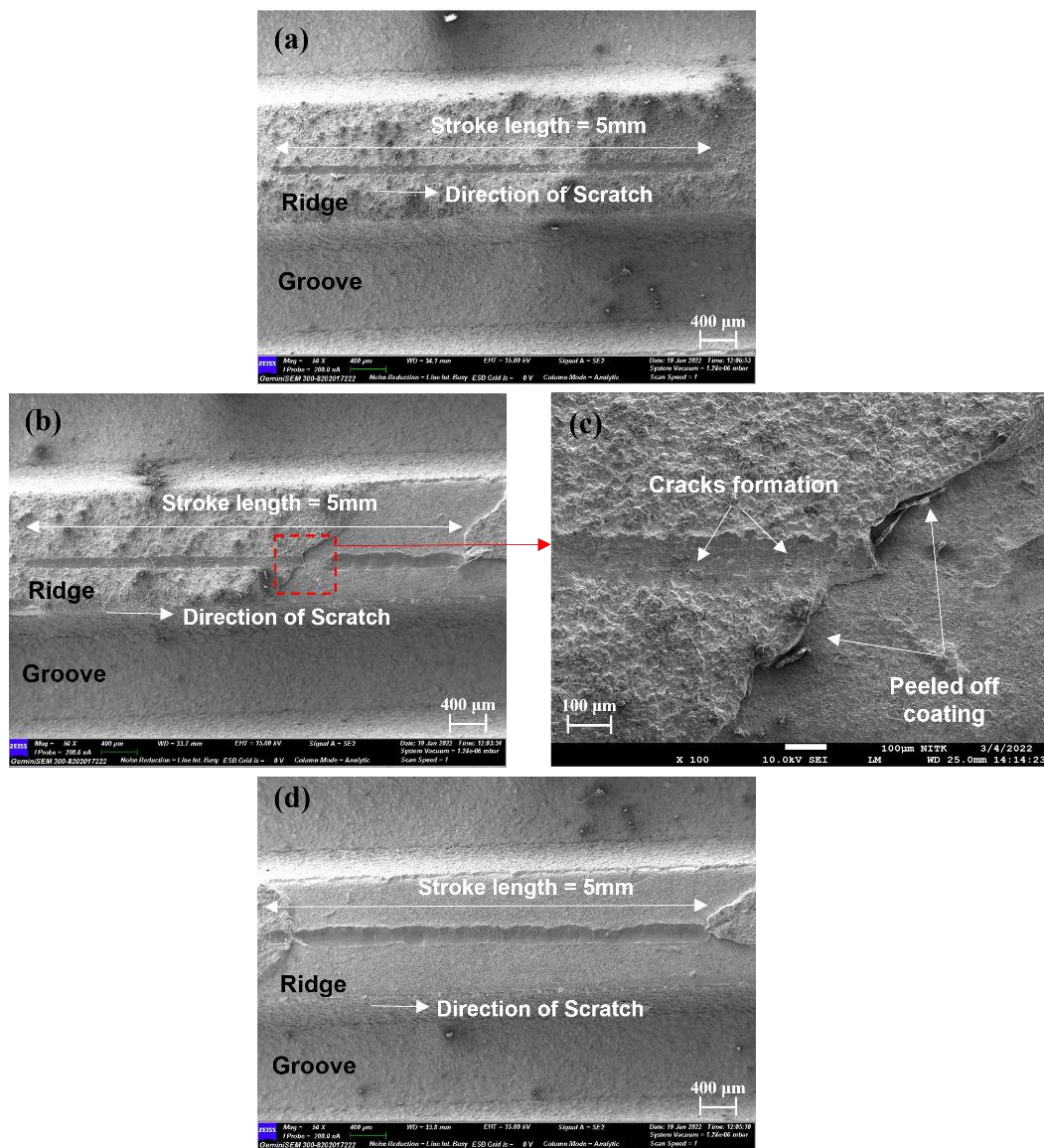


Figure 28: FE-SEM images of constant load scratch (a) 20 N, (b) 30 N, (c) magnified image of 30 N at the area of failure, (d) 40 N

5.2.4.3D noncontact profilometer analysis

The 3D surface topography of the coating after the progressive scratch test is shown in Fig. 29a. The coating is intact at the beginning of the test, and the total peel-off is visible over a stroke length of above 3.5 mm, where the critical load for failure is reached. The impact of a load exceeding the critical load (30-35 N) has been extended laterally to the sides, causing the coating to peel off over the entire surface of the ridge. However, the effect load has not been transferred to the sidewall of the grooves/wall of the channels, where the coating is still adhering to the substrate. The load above the critical load is high enough to plow the substrate. Similar behavior was noticed during the constant load test carried at 30 N, where the delamination started above a certain stroke length while the coating was wholly peeled off at the beginning of the 40N load test, as shown in Fig. 29 c and d. The constant load test at 20 N did not show a failure indication in Fig. 29b.

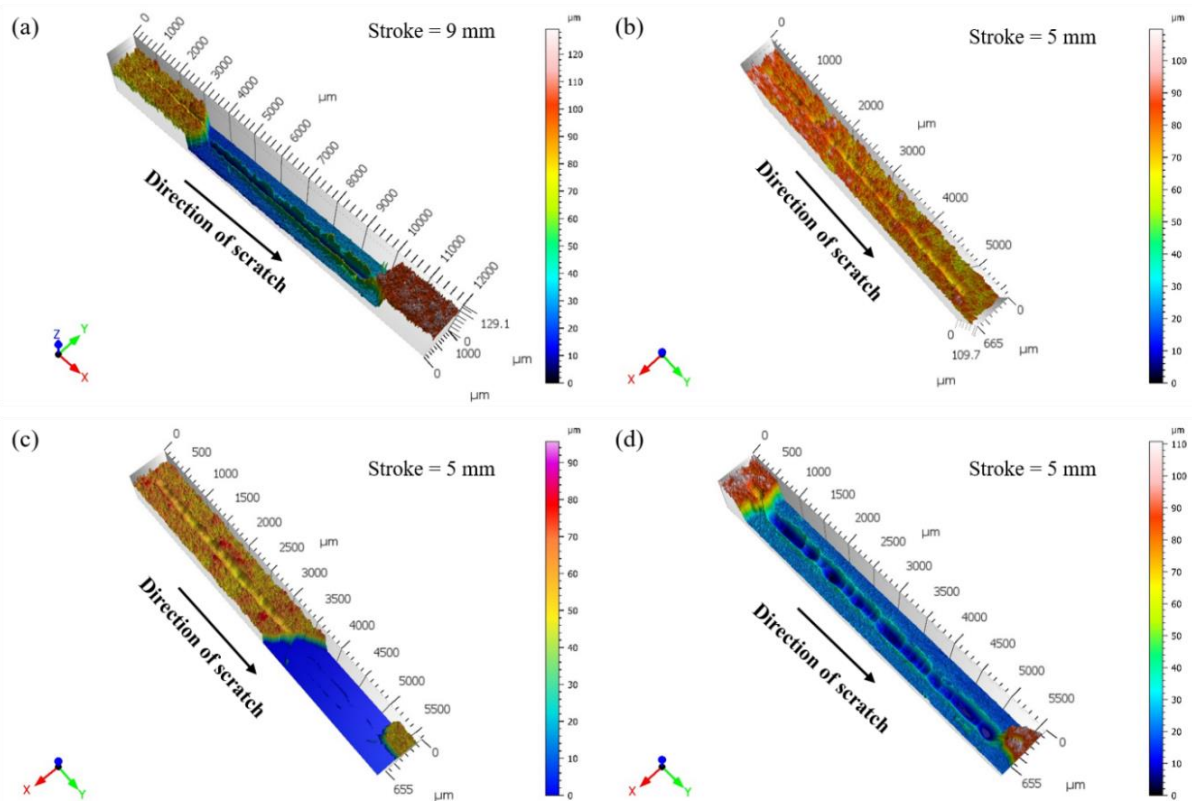


Figure 29: (a) Confocal profilometer images of progressive load scratch test (a) and constant load test (b) 20N, (c) 30N, (d) 40N

The MCF coating shows the tendency of abrasive wear during the scratch indentation test, while material removal in the Crofer steel substrate is entirely in plowing wear mode. The mechanism of coating failure is clearly interfacial delamination/peel-off due to the mechanical interlocking of asperities and molten-solidified particles. There was an absence of

metallurgical bonding and significant chemical in-homogeneity at the interface. Besides, the residual stress variation between the ceramic coating and metallic substrate can also be attributed to the interfacial delamination. The critical load to failure at around 30-35 N has been considered superior adhesion at the interface in the APS coating process. The critical load for failure for some of the ceramic coatings reported in the literature was relatively lower than that reported in the present study (Ariharan and Maurya 2021).

It should be noted that a moderately thin coating, a thickness of around 50-60 μm , is sufficient to act as a Cr-diffusion barrier for SOFC applications. The present study emphasizes that the correlative scratch indentation test (combination of progressive and constant load) is beneficial for understanding the critical load to failure. It would be highly suggested to overlay ceramic coatings on metallic substrates when the coating thickness is relatively small. It should be noted that MCF coatings change and densify extensively after heat treatment, so the measurements do not reflect the coating properties observed in service.

5.3. Early oxidation of Crofer 22 APU steel

5.3.1. Surface morphology under scanning electron microscope (SEM)

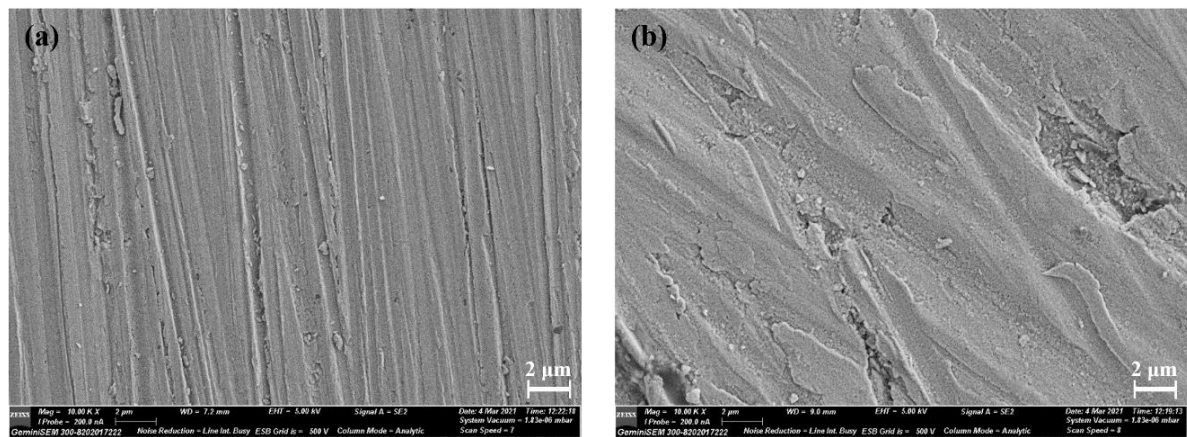


Figure 30: Surface morphology of Crofer 22 APU steel (a) before in-situ oxidation (b) after in-situ oxidation

The surface morphology of Crofer 22 APU before and after in-situ oxidation is shown in Fig. 30. Table 8 provides comprehensive data on the composition of various elements in the sample before and after oxidation obtained from area EDS analysis. No notable surface morphology changes have been observed on the SEM images to identify the oxides. However, an increase in the weight percent of oxygen has been noticed after in-situ oxidation. It is clear from the results that conventional state-of-the-art characterization tools such as XRD and FE-SEM did not identify any prominent oxide formation on Crofer steel.

Thus, surface analytical tools such as GD-OES, GIXRD, Raman spectroscopy, and AFM become more significant in revealing the oxide formation. Besides, they complement quantifying the complex oxide formation.

Table 8: Area EDS data of Crofer steel before and after in-situ oxidation

Elements (wt.%)	O	Fe	Cr	Mn	Si	Ti	Al	La
Before oxidation	1.03	73.29	24.11	0.45	0.00	0.34	0.01	0.76
After oxidation	3.75	70.52	23.72	0.32	0.03	0.47	0.00	1.07

5.3.2. X-Ray diffraction

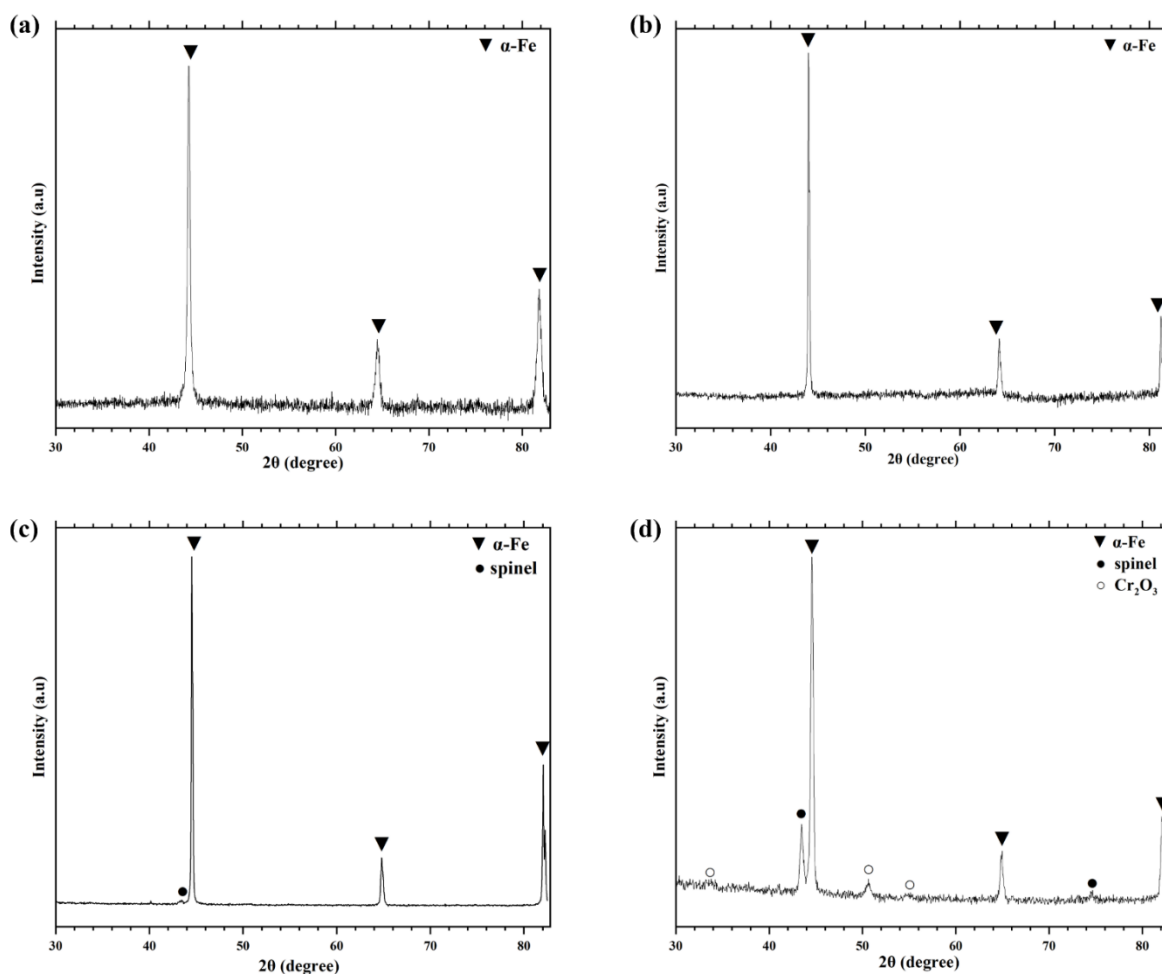


Figure 31: X-Ray Diffraction pattern of Crofer 22 APU (a) before oxidation at room temperature (b) at 950 °C in-situ oxidation (c) after in-situ oxidation at room temperature (d) GIXRD after in-situ oxidation

In Fig. 31, the normal XRD pattern of RT and 950 °C showed α-Fe peaks with no indication of oxide formation. Through the analysis, it can also be inferred that even though chromia (Cr₂O₃) and several other spinels like MnCr₂O₄ are readily formed with 15-30 seconds of

oxidation, under normal XRD conditions, detection of these oxides is difficult (Advisor and Aindow 2012). The GIXRD pattern reveals oxide formation, as shown in Fig. 31d. The peaks were designated as Fe (JCPDS File No. 080-3816), Cr₂O₃ (JCPDS File No. 076-9511), MnCr₂O₄ (JCPDS File No. 38-1479) (Miguel-Pérez et al. 2012). The oxide scale in the oxidized Crofer steel contains chromia (Cr₂O₃) and spinel (MnCr₂O₄). The substrate peaks of α -Fe indicated that the oxide scales formed were very thin. Chromium has more affinity toward oxygen for the formation of chromium oxide (Rao et al. 2020). The weight percentage of chromium (20-24%) was favorable in forming its oxides.

The Debye-Scherrer equation for calculating the crystallite size of the oxides is given in Equation (8) (Devendra et al. 2021).

Table 9: Crystallite size of Oxides from GIXRD

Phases	Peak position (°2Th)	FWHM (°2Th)	Crystallite Size (Å)
MnCr₂O₄	43.444	0.383	290
	74.502	0.340	418
Cr₂O₃	33.586	1.078	83
	50.599	0.638	159
	54.705	0.452	245

In the present study, the crystallite size (Table 9) reveals that the chromia layer has been fine-grained during early oxidation, which makes it favorable for Mn to diffuse to the surface to form MnCr₂O₄. With the addition of a small percentage of Mn, the Fe-Cr alloys form spinels of Mn and Cr (Horita et al. 2003). These alloys with below 1 wt.% Mn content led to (Mn, Cr)₃O₄ spinel formation on top of Cr₂O₃, which increases the electrical conductivity and mitigates the Cr evaporation due to lower evaporation pressure of the spinel than chromia (Yang et al. 2004, 2007). The reaction to form MnCr₂O₄ will also lead to the depletion of the Cr reservoir for the formation of Cr₂O₃ (Advisor and Aindow 2012). The kinetics data indicated that thin oxide film formed on Fe-Cr alloys tends to break by the voids nucleated by vacancy condensation at the metal-oxide interface (Cox et al. 1975). These voids cause the chromia layer to expose the underlying substrate to the atmosphere leading to faster diffusion of Mn to form spinels.

Chromia forming alloys are subjected to volatilization of chromium species (CrO₂(OH)₂) during oxidation, and this makes it complex to investigate the oxidation behavior of Crofer steel (Niewolak et al. 2014). At low oxygen partial pressure of 10⁻²¹ bar and 1000 °C temperature, studies showed the formation of a stoichiometric compound MnCr₂O₄, but a

continuous solid solution of $(\text{Mn}_x\text{Cr}_{1-x})_3\text{O}_4$ with $0 < x < 0.39$ results in chromium site occupied by manganese when the oxide system is in equilibrium with air (Naoumidis et al. 1991). The MnCr_2O_4 formed is a normal spinel that is stable at low $p\text{O}_2$ (SOFC anode gas), and $(\text{Mn}, \text{Cr})_3\text{O}_4$ is an inverse spinel that forms in gases with high $p\text{O}_2$ (in the air) (Niewolak et al. 2016). The rapid growth of the outer spinel layer at higher oxygen partial pressure seemed possible with the existence of manganese of both cation sub-lattices leading to a higher diffusion coefficient (Niewolak et al. 2014). In the present study, oxidation was carried out at 10^{-4} mbar pressure, which is favorable for forming the top layer of MnCr_2O_4 .

5.3.3. Atomic force microscopy (AFM)

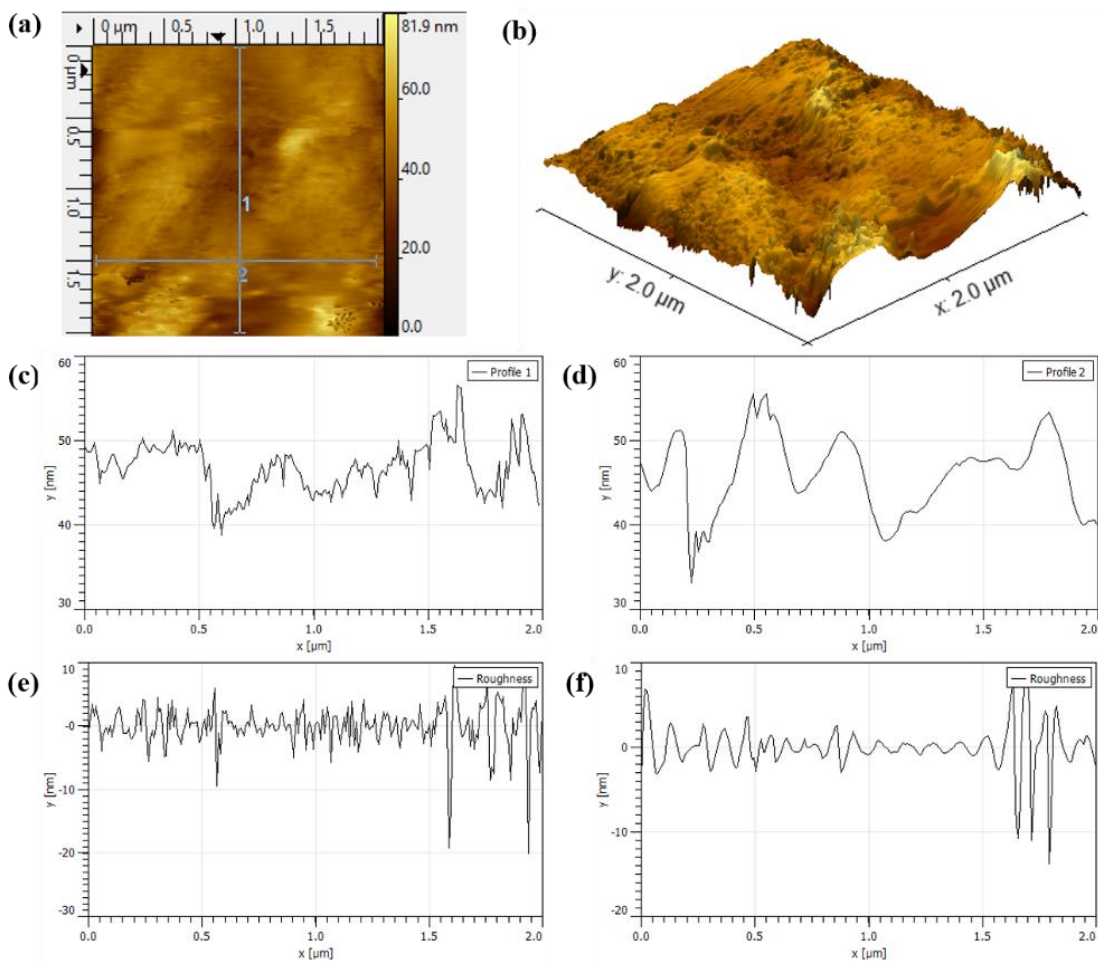


Figure 32: AFM images of Crofer 22 APU before in-situ oxidation (a) 2D image, (b) 3D image, (c) line profile 1, (d) line profile 2, (e) roughness profile across line 1, (f) roughness profile across line 2.

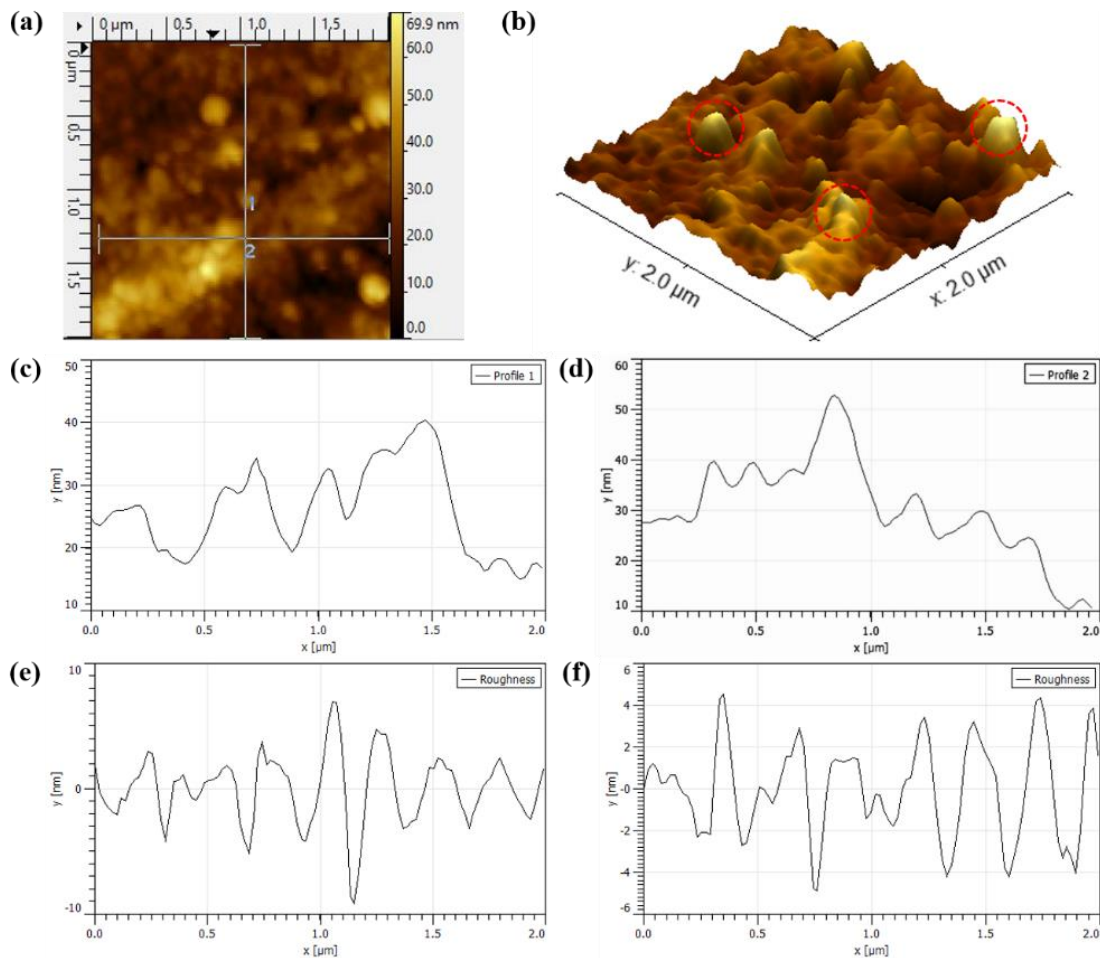


Figure 33: AFM images of Crofer 22 APU after in-situ oxidation (a) 2D image, (b) 3D image (red dotted line indicated high structures), (c) line profile 1, (d) line profile 2, (e) roughness profile across line 1, (f) roughness profile across line 2.

The AFM topographies and roughness profiles of Crofer steel before and after oxidation are shown in Fig. 32 and 33. The hump (red circles) and valley are indicated by bright and dark colors, respectively. The roughness parameters are given in Table 10. R_a is the average roughness of the considered line profile, R_q is the root-mean-square roughness of the profile, and R_z is the average maximum height of the profile. The change in roughness was noticed after the formation of oxide scales. The oxide scales formed showed a reduction in R_z value, indicating the surface of the specimen to be smooth after oxidation (Wei et al. 2018). This showed a 60% decrease in surface roughness across both profiles, and oxide formation smoothed the steel surface. The roughness of WO_3 thin films deposited on glass substrate at different temperatures, estimated by AFM, showed an initial increase up to 400 °C and reduced because of slower crystal growth and incomplete decomposition of WO_3 film below 400 °C (Srinivasa Rao et al. 2022). The hump (red dotted circle in Fig. 33b) indicates a heterogeneous oxide layer due to grain agglomeration. Similar findings

have been observed by AFM on Crofer 22 H (Gazdzicki et al. 2016), and the oxidized surface became more compact and smoother (Wei et al. 2018).

Table 10: Roughness values of Crofer 22 APU from AFM

Parameters (nm)	Before in-situ oxidation			After in-situ oxidation		
	R _a	R _q	R _z	R _a	R _q	R _z
Line profile 1	2.10319	3.34218	21.0122	2.11209	2.74366	9.30359
Line profile 2	1.57616	2.56834	17.3053	1.84430	2.24399	7.86852

5.3.4. Raman spectroscopy

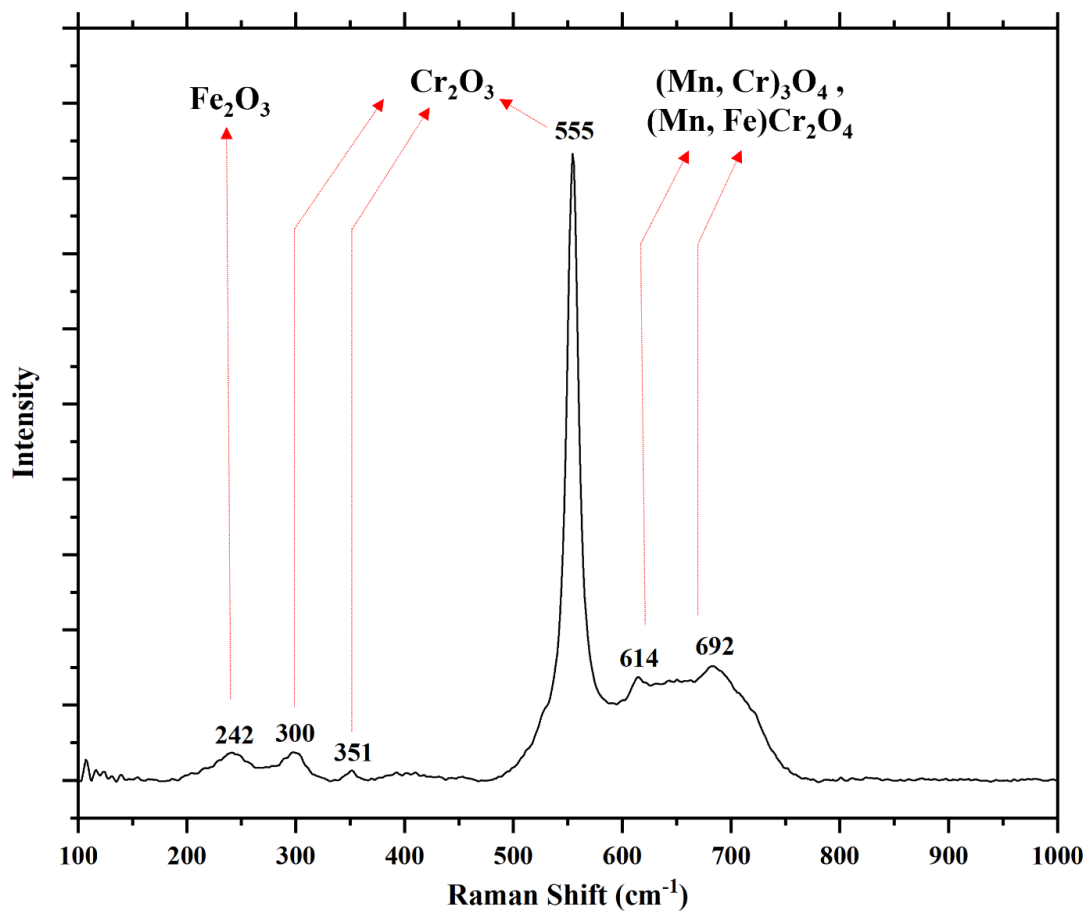


Figure 34: Confocal Raman Spectra of Crofer 22 APU after in-situ oxidation

Figure 34 shows Raman spectrum of chromium oxide with an intensive peak at 555 cm^{-1} and weak peaks at 300 and 351 cm^{-1} (Bik et al. 2022; Demeneva et al. 2019; Ghiara et al. 2021; Mazur et al. 2022). The low intense peaks at 242 cm^{-1} represent Fe_2O_3 (Mazur et al. 2022; Rao et al. 2020). The peaks at 614 and 692 cm^{-1} correspond to $(\text{Mn, Cr})_3\text{O}_4$ and $(\text{Mn, Fe})\text{Cr}_2\text{O}_4$ spinels, respectively (Bik et al. 2022). However, the formation of oxides like Fe_2O_3 , $(\text{Mn, Cr})_3\text{O}_4$ was not detected in GIXRD. The change in cation distribution caused

by the phase transition results in a change in the relative intensity of the Raman peak (Priyadharsini et al., 2022). The Raman spectrum (Fig. 34) revealed the homogeneous formation of Cr_2O_3 , whereas the Fe_2O_3 , $(\text{Mn}, \text{Cr})_3\text{O}_4$, and $(\text{Mn}, \text{Fe})\text{Cr}_2\text{O}_4$ peaks have less intensity due to inhomogeneity (Mougin et al. 2001; Niewolak et al. 2016). The oxide layer formation (MnCr_2O_4 and Cr_2O_3) correlated to the AFM images and changes in surface roughness (Wei et al. 2018).

5.3.5. Glow discharge optical emission spectroscopy (GD-OES)

Analyzing FE-SEM images and XRD data provides qualitative information on the formation of oxide scales. In contrast, GD-OES provides a quantitative evaluation of the elemental distribution of the oxides scales as a function of the depth. Also, the time consumed for GD-OES testing and analysis was less than the SEM-EDS technique (Rao et al. 2020). The GD-OES depth profiles of Crofer steel before oxidation are shown in Fig. 35 (a-c). Fe and oxygen signals are very strong at the surface, while oxygen depletes after about 300 nm. The depth of Cr at the surface is shown to be strong, and the signal is stable up to the measured depth of 3 μm . The enrichment of Cr is seen till a depth of about 15 nm, where Cr and O intersect. As the oxides of Cr are readily formed on the Crofer steel, it can be confirmed that the Cr_2O_3 scale thickness is about 15 nm. The weight percentage of Mn in Fig. 35a is observed to be more than the nominal weight percentage of Mn in Crofer steel. The depth profile of elements like Si, Ti, Al, and Ni comply with the nominal weight percentage of the Crofer steel.

Figures 35 (d-f) show the depth profile of the Crofer steel after in-situ oxidation. The enrichment of Cr is seen from the top surface until the intensity of Fe increases. A very strong signal of O can be seen at the surface and become stable after a depth of about 2 μm . The determination of oxide layer formation from GD-OES results can be done in the material where the oxygen content exceeds 2 wt.%. This criterion is helpful in obtaining the oxide scale thickness as a function of exposure time (Zhu and Lindbergh 2001). The thickness of the oxide film can also be estimated by considering the depth profile of oxygen, where the signal drops to 50% of its value at the surface (Ghosh et al., 2013). But the intersection of the signal from Cr and O is seen after the signal of O drops well below 50%. Comparing the signals of Cr from Fig. 35a and 35d, the elemental composition shows an increase in Cr and O at the surface, confirming the formation of the Cr_2O_3 layer after in-situ oxidation.

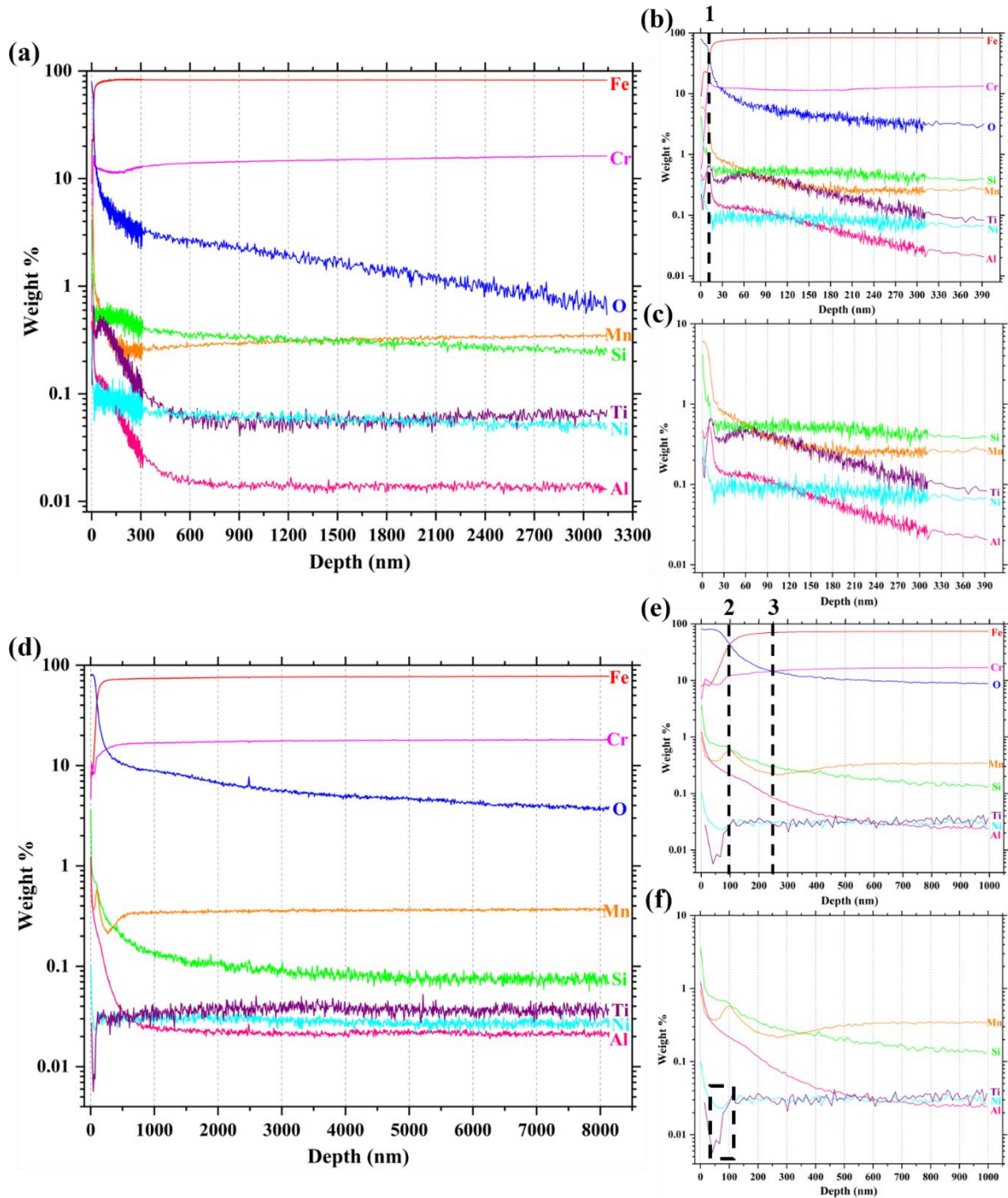


Figure 35: Depth Profile elemental composition by GD-OES (a) before oxidation (b & c) magnified view (d) after oxidation (e & f) magnified view, (line 1 – the intersection of all elements with O, line 2 – the intersection of elements with O, line 3 – the intersection of Cr with O, dotted square – enrichment of Ti)

The depth profile in Fig. 35f indicates the existence of Ti-rich internal oxides in the subsurface of the oxidized sample, where the enrichment of Ti has usually been observed (Garcia-Fresnillo et al., 2018). The depletion in weight percentage of Si, Ni, and Al from the surface after in-situ oxidation corresponds to a decreased amount of the precipitated

phase. The formation of silicon oxides with low Si concentration was expected in the subscale region, similar to titanium, due to more thermodynamic stability than Cr_2O_3 (Niewolak et al. 2014).

A thin oxide layer of chromia is readily formed on the steel, as confirmed by GD-OES (Fig. 35b). As the specimen is exposed to in-situ high temperature conditions, the temperature increase enhances the chromia layer's growth. Mn diffuses through the chromia layer to form MnCr_2O_4 spinel as the top oxide layer. The formation of MnCr_2O_4 spinel and growth of the Cr_2O_3 layer was also confirmed by GD-OES (Fig. 35e). The two-layer oxidation scale formation in Crofer 22 APU can also be understood with the depth profile obtained by GD-OES in Fig. 35d, where the enrichment of Mn and Cr follow a similar pattern up to a depth of 100 nm, after which the Mn depletion is seen. The intersection of Cr and O is seen at a depth of 250 nm in Fig. 35e, which indicates that the Cr_2O_3 subscale layer thickness is 150 nm below the top layer MnCr_2O_4 . The thickness of spinel growth after in-situ oxidation accounts for 40% of the overall scale thickness, and the remaining 60% can be attributed to the Cr_2O_3 subscale. The thickness of the Cr_2O_3 subscale is more than the top layer MnCr_2O_4 . A slow growth rate of formation of chromia was observed in pure chromium and chromium-based alloy at elevated temperatures (Singheiser et al. 2010). Chromium-containing alloys (Fe-15 wt.% Cr and Fe-20 wt.% Cr) showed a faster growth rate of spinel oxides compared to corundum oxides (Fe_2O_3 , Cr_2O_3) (Cox et al. 1975). Hence, in the current study, growth rate of MnCr_2O_4 and Cr_2O_3 is 1:1.5. The formation of spinel is also in good agreement with Raman spectra peaks obtained at 614 and 692 cm^{-1} (Fig. 34).

The depletion of Ti from the surface to a depth of 70 nm is seen. Enrichment of Ti can be seen between 70 nm and 120 nm, after which the signal becomes stable. It was observed that the addition of a small amount of Ti forms a very thin precipitate of Ti oxides (TiO_x) in the sub-surface region (Magdefrau et al. 2013). The Gibbs free energy change for the formation of oxide of Ti is -920 kJ/mol of O_2 (Hasegawa 2013). As the weight percentage of Ti in Crofer steel is 0.03-0.2 (Table 1), TiO_x is observed in the form of precipitates incorporated in the subscale surface of the oxide layer. This can be ascribed to the high solubility of titanium in the Cr_2O_3 subscale at low oxygen partial pressure in the alloy/scale interface (Naoumidis et al. 1991).

5.4. Thermal expansion induced thermal mismatch of $Mn_{1.0}Co_{1.9}Fe_{0.1}O_4$ coated Crofer 22 APU metallic interconnect used for SOFC – an experimental approach using in-situ high temperature X-ray diffraction

5.4.1. Phase analysis and thermal expansion mismatch

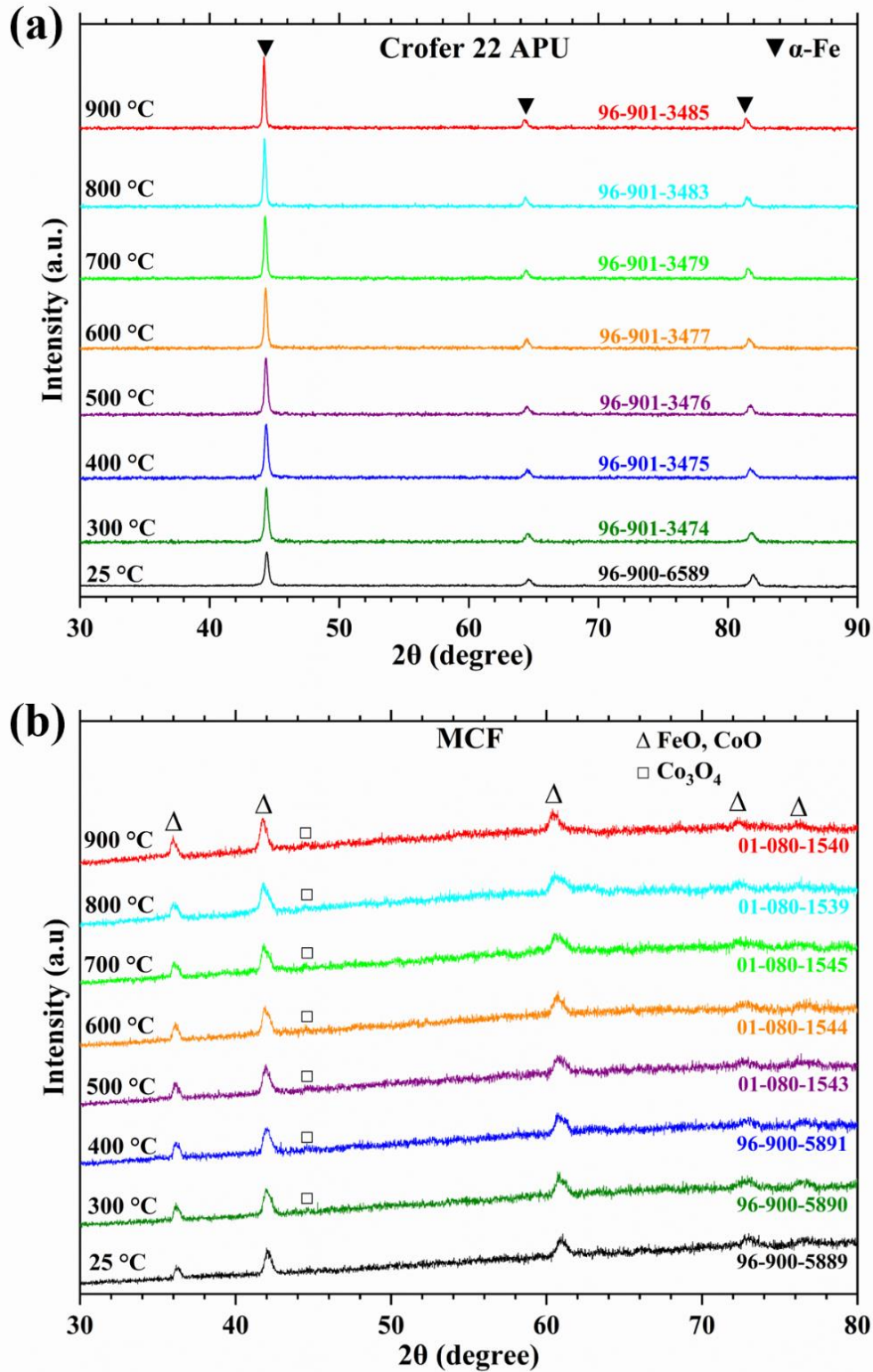


Figure 36: In-situ high-temperature XRD stack (a) Crofer 22 APU (b) MCF coating

The analyzed XRD data of Crofer 22 APU and MCF coating at different temperatures are shown in Fig. 36. No difference in XRD pattern was noticed between room temperature and at high temperature except for peak narrowing and increase in intensity. The alpha-iron (α -Fe) with bcc structure is the prevalent phase at all temperatures (Fig. 36a). Even at high temperatures, the XRD pattern did not reveal the formation of oxides on the Crofer steel. The oxides such as Cr_2O_3 and MnCr_2O_4 are formed as thin films within 15-30 seconds of oxidation, but detecting these oxides is difficult in normal XRD (Magdefrau 2013).

The analysis of the XRD pattern of MCF coated steel (Fig. 36b) revealed a two-phase mixture of CoO as the primary phase and $\text{Fe}_{3-x}\text{O}_4$, having a rock salt crystal structure. During the process of spraying MCF coating on Crofer steel, a sudden quenching leads to reduced time for the spinel phase of MCF powder to completely transform into a stable phase, resulting in the formation of metastable rock salt structure (Grünwald et al. 2019). The CoO and FeO phases are present at all temperatures. Upon isothermal heating of the specimen in the high-temperature stage, a new peak emerges in the temperature range of 300 °C - 900 °C indicating the formation of Co_3O_4 . A fraction of CoO having metastable rock salt structure is transformed into a stable Co_3O_4 spinel phase. The holding time at each temperature was about 15 minutes; therefore, the complete transformation of the CoO phase to Co_3O_4 was not observed. The Co_3O_4 phase detected in XRD shows an increase in intensity with an increase in temperature.

The X'Pert high score analysis software was used to evaluate the lattice parameters for different temperatures using the available database (Space group: Im-3m - Crofer 22 APU & Fd-3m - MCF coating). The change in the lattice parameter in Crofer steel throughout the temperature range is entirely dependent on the variation of α -Fe crystallite size. Similarly, the change in the lattice parameter of the MCF coated steel is dependent on the Co_3O_4 stable phase formed during heating. The coefficient of thermal expansion (CTE) was calculated using the change in lattice parameters. Crystallite size at different temperatures was computed using the Scherer equation. The change in lattice parameter and CTE of Crofer 22 APU and MCF coating have been tabulated in Table 11 and Table 12, respectively.

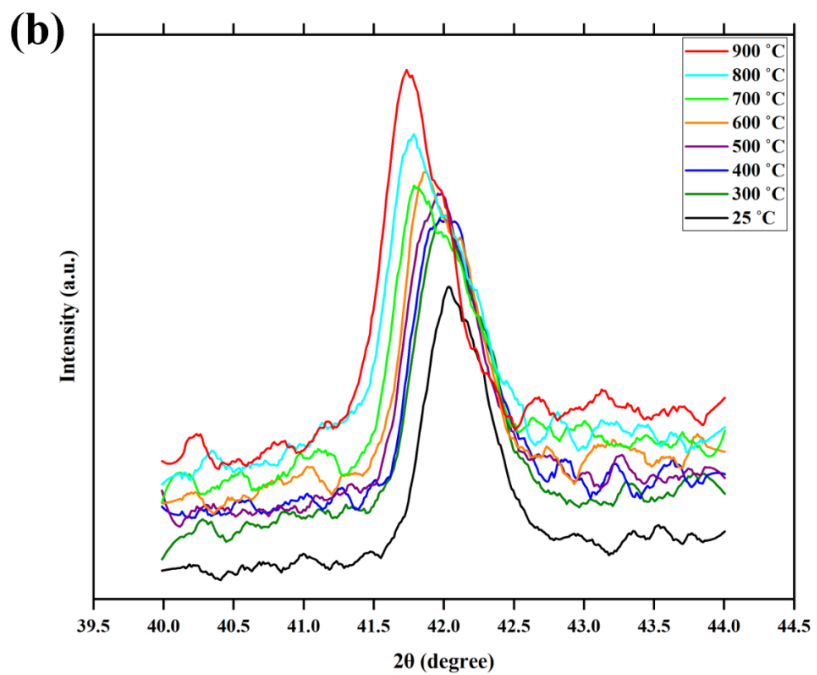
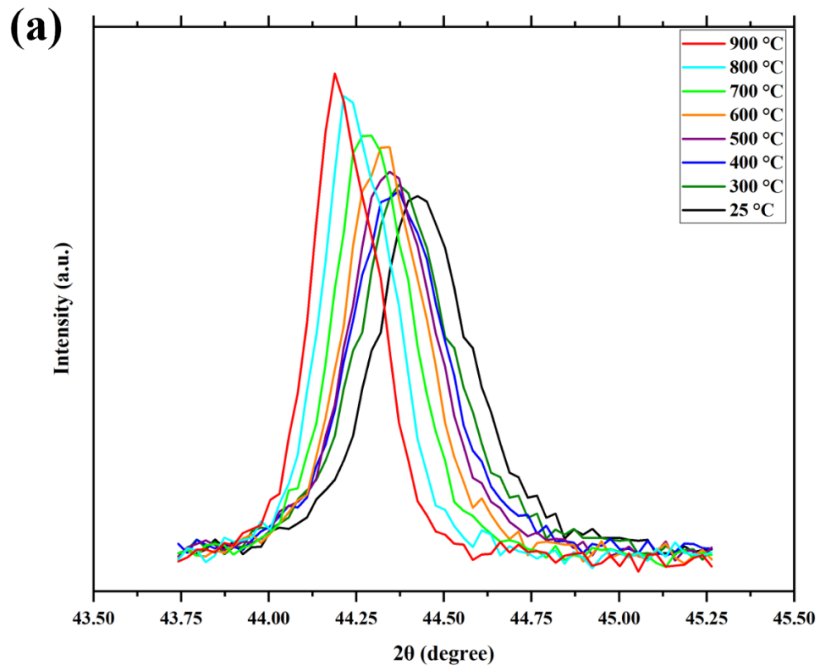


Figure 37: Peak shift after in-situ (a) Crofer 22 APU (b) MCF coating

The change in crystallite size and lattice strain of Crofer steel and MCF coating with a temperature estimated with Scherrer equation with instrument correction using SiO₂ standard (Kamalan Kirubaharan et al. 2017).

$$D = k\lambda/\beta_D \cos\theta \dots\dots\dots(9)$$

where k is the shape factor (0.89), λ is the wavelength of the radiation, θ is the peak position, β_D is the peak width at a half-maximum intensity, and the instrument corrected broadening given by (Rogers and Daniels 2002),

$$\beta_D^2 = [(\beta)_{\text{measured}}^2 - (\beta)_{\text{instrumental}}^2] \dots\dots\dots(10)$$

The change in crystallite size and lattice strain of Crofer steel and MCF coating with a temperature estimated with the Williamson-Hall plot Uniform Deformation Model (UDM) is given by (Basak et al. 2022),

$$\beta_{hkl} \cos \theta = \left(\frac{k\lambda}{D}\right) + (4\epsilon \sin \theta) \dots\dots\dots(11)$$

The results of the instrument corrected Scherrer equation cannot be intercorrelated with the Williamson-Hall plot.

Calculation of CTE for the specimen between room temperature and 950 °C is given by (Corsepius et al. 2007; Halvarsson et al. 1995);

$$\text{By the definition of CTE, } \alpha = \frac{1}{a_i} \left(\frac{\partial a}{\partial T}\right) = \frac{a_o - a_i}{a_i(T_o - T_i)} \dots\dots\dots(11)$$

where ∂a is the difference of lattice parameters a for the interval ∂T , ∂T is the difference in temperature (°C), a_i , a_o are initial and final lattice parameters respectively (Å), T_i , T_o are initial and final temperature respectively (°C). Here, T_i is considered at room temperature (25 °C), and a_i is the lattice parameter with respect to T_i for all our calculations.

Table 11: Lattice Parameter, Crystallite size, and Coefficient of thermal expansion (CTE) of Crofer 22 APU after in-situ oxidation

Sl. No	Temperature (°C)	Elements/ Compounds	Crystal Structure	Lattice Parameters (Å)	CTE ‘ α ’ (x 10 ⁻⁶ /°C)
				a = b = c	
1	25	α -Fe	Cubic	2.866	-
2	300	α -Fe	Cubic	2.873	8.88
3	400	α -Fe	Cubic	2.877	10.24
4	500	α -Fe	Cubic	2.882	11.75
5	600	α -Fe	Cubic	2.886	12.13
6	700	α -Fe	Cubic	2.891	12.90
7	800	α -Fe	Cubic	2.895	13.06
8	900	α -Fe	Cubic	2.900	13.56

Table 12: Lattice Parameter, Crystallite size, and Coefficient of thermal expansion (CTE) of MCF coated steel after in-situ oxidation

Sl. No	Temperature (°C)	Elements/ Compounds	Crystal Structure	Lattice Parameters (Å)	CTE 'α' (x 10 ⁻⁶ /°C)
				a = b = c	
1	25	Co ₃ O ₄	Cubic	8.0968	-
2	300	Co ₃ O ₄	Cubic	8.1180	9.52
3	400	Co ₃ O ₄	Cubic	8.1290	10.60
4	500	Co ₃ O ₄	Cubic	8.1440	12.23
5	600	Co ₃ O ₄	Cubic	8.1546	12.40
6	700	Co ₃ O ₄	Cubic	8.1690	13.20
7	800	Co ₃ O ₄	Cubic	8.1893	14.10
8	900	Co ₃ O ₄	Cubic	8.1975	14.20

Crystallite size and lattice strain were plotted as a function of temperature, as shown in Fig. 38 (a-d). In Fig. 38 a, b, the crystallite size and lattice strain variation for steel substrate are typical, while the lattice strain of MCF coating keeps increasing until 800 °C and then decreases. The crystallites of MCF coating are more stable and showed marginal variation as a function of temperature. The lattice parameter and coefficient of thermal expansion were plotted as a function of temperature, as shown in Fig. 39 a, b. The CTE of Crofer 22 APU and MCF for different temperatures were listed in Tables 11 & 12. The CTE of substrate and coating at 900 °C were 13.56×10⁻⁶ /°C and 14.20×10⁻⁶ /°C, respectively.

The obtained CTE values of substrate and coating for different temperatures were used to calculate the thermal stress based on the following equation (Daniel et al. 2011; Huntz et al. 2006) :

$$\sigma_{th} = \frac{E_c}{1-\nu_c} (\alpha_s - \alpha_c) (T - T_d) \dots\dots\dots(12)$$

E_c is the Elastic Modulus, and ν_c is the Poisson's ratio of coating. The α_s and α_c are the thermal expansion coefficients of the substrate and coating, respectively. T is the temperature at which thermal stress is measured, and T_d is the deposition temperature (Assuming T_d=0 and T_d=200 °C). E and ν are 220 GPa and 0.3 for Crofer 22 APU (Stygar et al. 2013) and 210 GPa and 0.25 for Co₃O₄ (Meena et al. 2018), respectively.

The thermal expansion mismatch between the Crofer substrate and MCF coating upon heating from the zero-mismatch point of room temperature to a temperature T can be calculated using the equation (Church et al. 2005):

$$\Delta E_{\text{heating}} = \left[\frac{\Delta l}{l_0} \right]_{m,T} - \left[\frac{\Delta l}{l_0} \right]_{c,T} \dots\dots\dots(13)$$

where Δl is the change in lattice parameter, l_0 is the lattice parameter at room temperature, and T is the corresponding temperature.

Table 13: Thermal stress between Crofer 22 APU and MCF, Thermal expansion mismatch (%) between Crofer steel and MCF coating upon heating from room temperature in MCF coated Crofer steel

Temperature °C	Thermal Stress (GPa)		Thermal mismatch (%)
	T _a = 0 °C	T _a = 200 °C	
300	-0.05	-0.018	-0.17
400	-0.04	-0.02	-0.14
500	-0.07	-0.043	-0.24
600	-0.05	-0.034	-0.16
700	-0.06	-0.042	-0.19
800	-0.23	-0.17	-1.2
900	-0.17	-0.125	-0.6

Table 13 and Fig. 39 d & e show the thermal stress generated during heating. The mismatch in thermal expansion between Crofer steel and MCF coating upon heating from room temperature is shown in Fig. 39c. Up to 700 °C, the net thermal expansion mismatch is marginal and showed no significant mismatch. But the increase in temperature beyond 700 °C showed a substantial variation in the mismatch, which is compressive.

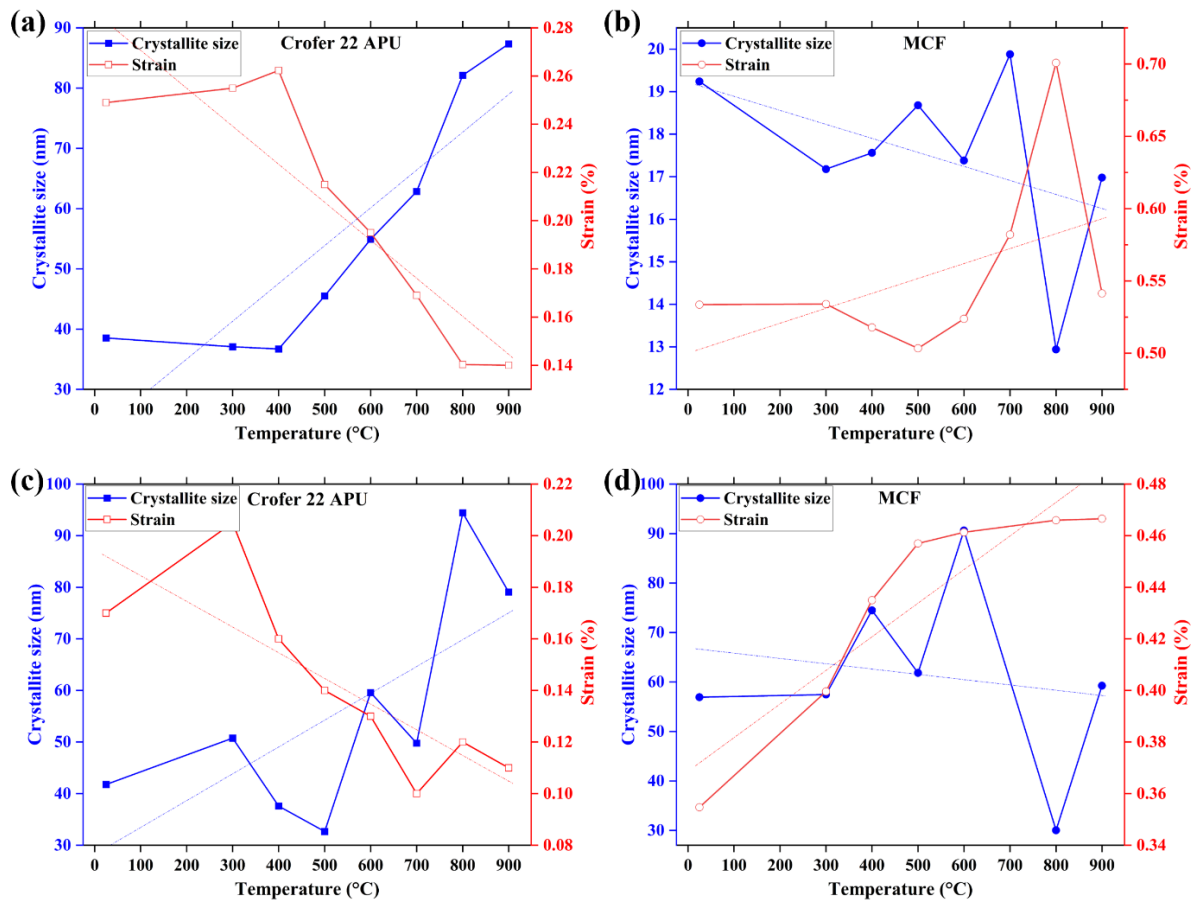


Figure 38: Crystallite size & lattice strain vs. temperature, Scherrer Equation - (a) Crofer 22 APU, (b) MCF, Williamson-Hall Plot - (c) Crofer 22 APU, (d) MCF

5.4.2. Discussions

The formation of Mn_2O_3 and Cr_2O_3 on a steel surface under a controlled atmosphere was in its early stage and difficult to detect by HTXRD. However, the thin film of these oxides did not influence the lattice parameter, lattice strain, and crystallite size CTE measurements. Therefore, this study has not considered the influence of these oxides on CTE and thermal mismatch. However, MCF coating under HTXRD showed traces of Co_3O_4 phase formation above 300 °C. This phase transformation is indeed reflected in the lattice strain variation as a function of time. Interestingly, lattice strain gradually increases with temperature until 800 °C, which is usually uncommon. The strained lattice usually relaxes at high temperatures. This phase transformation is martensitic in nature, which is deformation/strain-induced. The volume expansion associated with the phase transformation is the reason for a gradual increase in lattice strain until 800 °C; it may be the temperature at which the transformation is complete (Grünwald et al. 2017; Shen et al. 2018; Vaßen et al. 2016). It was also seen that the Co_3O_4 phase emerging after 300 °C led to a volume expansion induced by the phase transformation of Co_3O_4 from cubic ↔

tetragonal, which is believed to be the reason for crack-healing/self-healing in the MCF coating. The volume expansion of about 21.1% during the phase transformation was also attributed to the densification characteristics of MCF coating (Grünwald et al. 2017). $(\text{Mn}, \text{Co})_3\text{O}_4$ spinel has a dual-phase microstructure consisting of cubic and tetragonal structures. MCF coating having a similar spinel structure undergoes a displacive phase transformation at higher temperatures (Aukrust and Muan 1963; Naka et al. 1972; Yang et al. 2007). Once the phase transformation is complete, the lattice strain decreases above 800 °C. Similar observations were seen in Ti-6Al-4V. A decrease in the lattice strain in the temperature range of 800-900 °C implied that the strain was no longer compressive but became tensile (Kaschel et al. 2020). The increase in the crystallite of mechanically alloyed $\text{Mg}(\text{Ni}_{1-x}\text{Mn}_x)_2$ was due to the growth of crystal grains and microstrain reduction (Gkanas et al. 2019). The grain growth in the MCF coating was sluggish up to 600 °C (Fig. 38b), and the growth rate is seen to increase after 600 °C due to the decrease in compressive lattice strain with increasing temperature. The change of tensile strain to compressive after 800 °C and the phase transformation to Co_3O_4 in MCF were detected in small traces in the XRD patterns (Fig. 36b). The formation of new Co_3O_4 grains hinders grain growth (Grünwald et al. 2017; Vaßen et al. 2016). Hence the microstructure (crystallite size) of MCF coating is stable at higher temperatures.

In the analysis of high-temperature XRD, cubic \leftrightarrow tetragonal transformation of the spinel phase in $\text{Mn}_{1.5}\text{Co}_{1.5}\text{O}_4$ was observed around 400 °C. Still, the thermal expansion behavior of the spinel was not affected by the phase transformation (Yang et al. 2007). In the present study, Co_3O_4 phase transformation did not influence the CTE of MCF coating, which is $14.20 \times 10^{-6} / ^\circ\text{C}$, while the CTE of steel substrate is $13.56 \times 10^{-6} / ^\circ\text{C}$. The CTE of MCF coating is marginally higher than that of Crofer steel substrate. Indeed, MCF was designed to have comparable CTE to ferritic stainless steels used for SOFC interconnects. In Table 11, the CTE of Crofer steel at 950 °C was $13.56 \times 10^{-6} / ^\circ\text{C}$. The average CTE of Cr_2O_3 and Crofer 22 APU between room temperature and 800 °C are 9.6 and 12.4 ppm K^{-1} , respectively (Bi et al. 2013). The insignificant difference in CTE of Crofer steel and MCF coating shows good compliance of the interconnect material with other components of SOFCs, having CTE values in the range of $10\text{-}13 \times 10^{-6} / ^\circ\text{C}$. The XRD peak shift to the left is caused due to the thermal expansion of the crystal lattice with the temperature rise, as shown in Fig. 37. The XRD peak with high FWHM values is attributed to poor crystalline quality or an existing amorphous phase. The increase in crystallite size results in the

narrowing of diffraction peaks (Londoño-Restrepo et al., 2020). At low temperatures, thermal expansion of crystal lattice due to annealing leads to a change in the lattice parameter. The diffusion of elements at low temperatures is very slow to cause notable phase transformation; hence, the variation in lattice parameters could be related to relaxation in stress (Elmer et al. 2005; Mortalò et al. 2019).

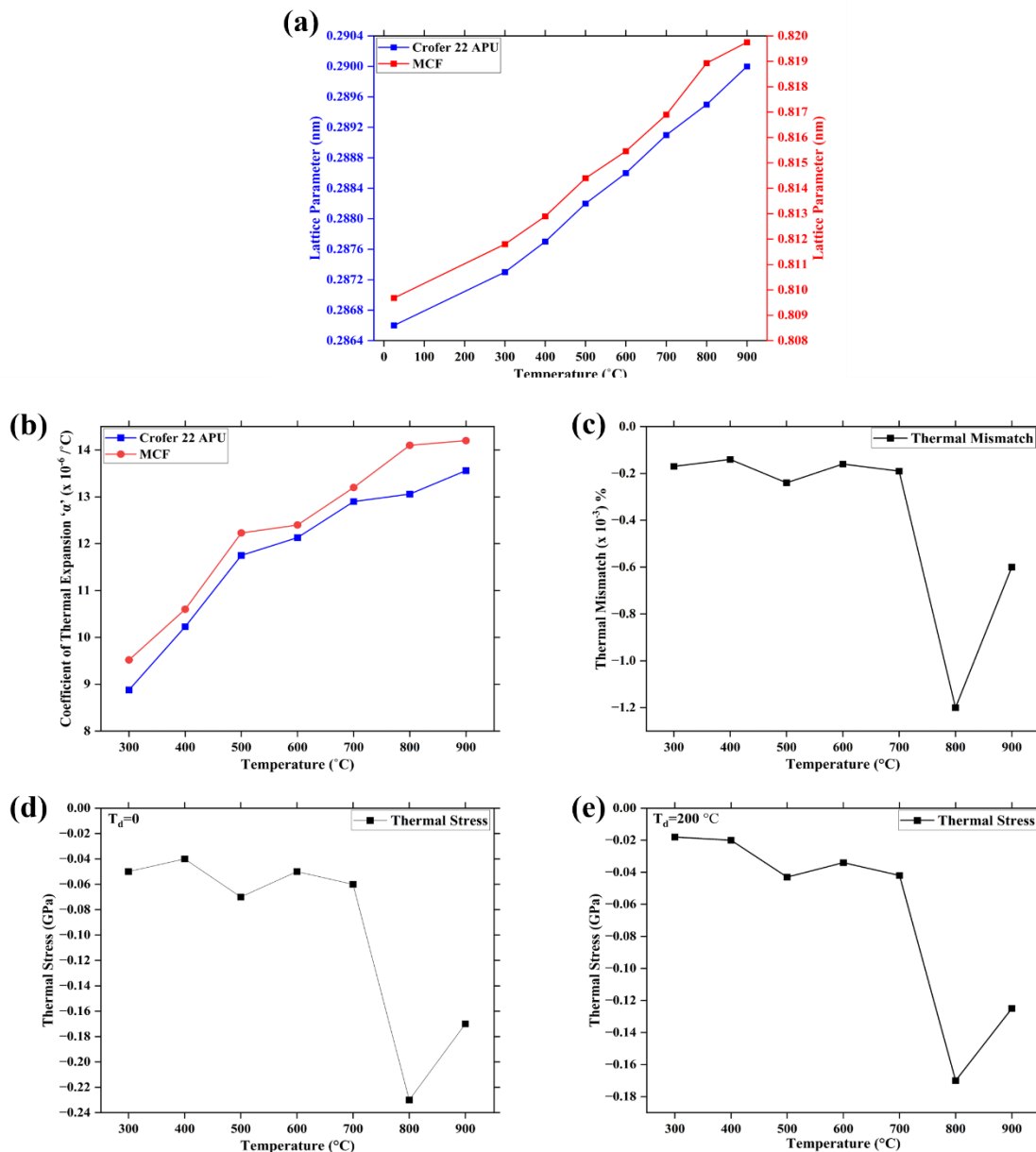


Figure 39: Variation of Lattice Parameter vs. Temperature (a), Coefficient of Thermal Expansion (CTE) (α) vs. temperature (b), Thermal mismatch between Crofer steel and MCF coating upon heating from room temperature (c), Thermal stress vs. temperature $T_d = 0$ & (d) $T_d = 200$ °C (e)

The phenomenon of peak shift and narrowing for steel substrate as a function of temperature in Crofer steel is as expected. In contrast, the shifting of the peak in MCF is

constrained. The narrowing is not prominent/significant as a function of temperature, especially at temperatures 400, 500, 600 and 700 °C. The strain-induced phase transformation of (Mn, Co, Fe)₃O₄ from cubic ↔ tetragonal is accompanied by induced volume expansion and is responsible for the absence of narrowing. The same can be seen in Fig. 38b, where the micro-strain increases as a function of temperature. However, the CTE of MCF has not been influenced by phase transformation. The same observation was also seen by Z. Yang et al. (Yang et al. 2007).

The overall residual stress in the components comprises intrinsic stress (σ_i), thermal stress (σ_{th}), and extrinsic stress (σ_e). During thermal treatment, a variation in each residual stress component influences the substrate due to the difference in CTE and is attributed to a change in thermal stress with temperature. An increase in compressive stress was observed during the heating Cr, and CrN layers as the CTE of the Cr and CrN layers was larger than that of the silicon substrate (Daniel et al. 2011). The in-situ high-temperature testing was performed on the as-received MCF-coated Crofer interconnect. As the Crofer substrate was laser cut to obtain the linear gas channel structure similar to the original SOFC interconnect, tensile residual stress could have been induced during the process. The magnitude of the thermal stress and thermal mismatch strain is compressive, as shown in Fig. 39 c & d. The higher CTE of MCF is beneficial as it induces the compressive mismatch stresses and prolongs coated interconnects' life. The thermal stress and mismatch are also compressive, assuming the plasma spray deposition temperature is about 200 °C. Relatively, a thin coating of thickness around 50 to 60 μm is sufficient to provide diffusion barrier coating on Crofer steel.

Similar behavior is seen in Fig. 39 b and c, where the initial sharp increase in CTE up to 500 °C was due to the formation of compressive Thermal Mismatch Stress (TMS). The further increase in the CTE above 500 °C is not sharp, which can be attributed to compressive stress relaxation. The creep rates of Crofer 22 APU are relatively high at elevated temperatures, i.e., $\approx 10^{-5} \text{ s}^{-1}$ at 800 °C at 20 MPa, which leads to a faster stress reduction (Chiu et al. 2011). The thermal mismatch between the Crofer substrate and MCF coating is shown in Fig. 39c. A sharp increase in the thermal mismatch at 800 °C could be due to a higher creep rate of the Crofer substrate. In summary, and as revealed by the in-situ HT-XRD study, the thermal mismatch and recrystallization between the steel substrate and MCF can be controlled by controlling the operating temperature of SOFC stacks by about 700 °C or below for the prolonged life of metallic interconnects.

5.5. Effect of plasma sprayed $\text{Mn}_{1.0}\text{Co}_{1.9}\text{Fe}_{0.1}\text{O}_4$ protective coating on the oxidation resistance of Crofer 22 APU SOFC interconnect

5.5.1. Microstructure analysis

Figures 40, 41, and 42 show the SEM secondary electron images of the substrate and coating surface morphology. Similarly, the backscattered cross-section image, corresponding elemental mapping, and line scan are shown. Table 14 shows EDS analysis of the surface oxide isothermally formed on Crofer 22 APU steel and MCF coating after 50, 200, and 400 hours at 850 °C in the air. Scale spallation was not observed on any of the samples after oxidation. After 50 h oxidation, as shown in Fig. 40a, SEM-EDS analysis of the oxide scales formed on the substrate revealed that the Mn- rich and Cr- rich products. The cross-section image (Fig. 40b) shows the oxide scale formed on the alloy surface with internal oxides of Ti distributed near the substrate-oxide interface, confirmed by the line scan. The elemental mapping and line scan (Fig. 40. c & d) show a Cr-rich oxide layer formed adjacent to the substrate and a top layer of Mn and Cr-rich oxide layer, indicating the spinel layer. After 200 h oxidation, as shown in Fig. 41a, the substrate surface consists of prism-like grains and clusters. The EDS results (Table 14) show that the atomic ratio of Mn to Cr is approximately 1:1 indicating the non-stoichiometric $\text{Mn}_{1.5}\text{Cr}_{1.5}\text{O}_4$ spinel layer formed uniformly on the underlying Cr_2O_3 because of the faster diffusion on Mn through fine-grained Cr_2O_3 structure. As seen in Fig. 41b, the oxides of Ti are seen as precipitates (black dots) near the substrate-oxide interface, which was also confirmed by the line scan (Fig. 41d). The elemental mapping (Fig. 41c) shows the distribution of the Mn and Cr-rich oxide scale on the substrate surface where the oxide scale can be seen to be non-uniform in few areas. After 400 h oxidation, as shown in Fig. 42a, the surface majorly consists of prism-like structures. From the EDS results in Table 14, the atomic ratio of Mn to Cr is approximately 1:2 for prism-like grains, indicating the structure's composition is close to MnCr_2O_4 . The clusters formed seem rich in Cr, indicating that the structures are probably Cr_2O_3 . The line scan (Fig. 42d) reveals the two-layer oxides of Cr and Mn-Cr spinel, where the signal of Cr increases near the substrate-oxide interface and the Mn signal increase near the top surface. The elemental mapping differentiates the oxides from the substrate.

In as-sprayed conditions, MCF coating exhibits a cubic rock salt phase of (Mn, Co, Fe) O. Upon annealing, the rock salt phase is transformed into a spinel phase, similar to the coating powder configuration (Grünwald et al. 2017). The EDS analysis (Table 14) at various points on the coating for 50, 200, and 400 h oxidation time shows the presence of Co and

O in the highest atomic percentage compared to Mn and Fe. The cubic rock salt phase of CoO in the as-sprayed condition is transformed to spinel phase Co_3O_4 . The Co_3O_4 spinel is dominated due to the higher weight percentage of Co in the coating powder. The cross-section of the MCF coating (Fig. 40f, 41f, 42f) shows the coating-substrate interface, and a reduction in porosity can be observed. The interface between the substrate and coating exhibits an oxide layer consisting of oxides of Cr and Al formed by the diffusion of the elements from the substrate. This elemental mapping confirmed this (Fig. 40g, 41g, 42g) and line scan images (Fig. 40h, 41h, 42h) of the MCF coating where the signal of Cr and Al enriches at the interface with the enrichment of oxygen and depletes towards the coating. This implies that the diffusion of Cr from the substrate is very low, and coating can effectively reduce the Cr-poisoning in stack operation. The thickness of this oxide layer is seen to grow with the increase in oxidation time. Porosity measurements from the image analysis determine an average porosity of $7.84 \pm 1.4\%$, $7.27 \pm 1.1\%$, and $6.64 \pm 1.1\%$ for 50, 200, and 400 h oxidation conditions, respectively. The resulting decreasing porosity levels indicate the densification of the coating.

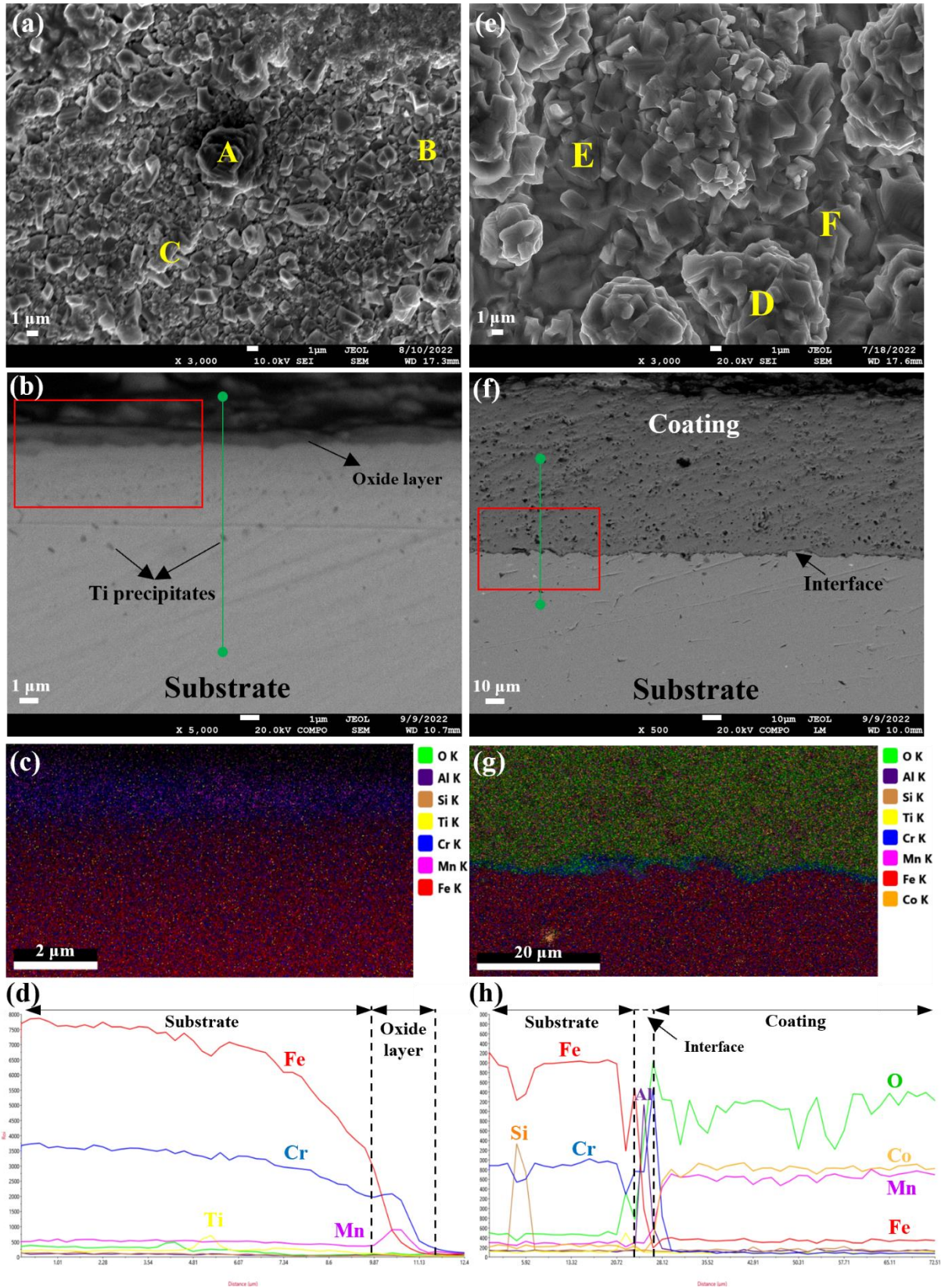


Figure 40: FE-SEM analysis after 50 h oxidation at 850 °C of Crofer 22 APU and MCF coating respectively, (a), (e) surface morphology, (b), (f) back scattered cross-section, (c), (g) elemental mapping, (d), (h) line scan

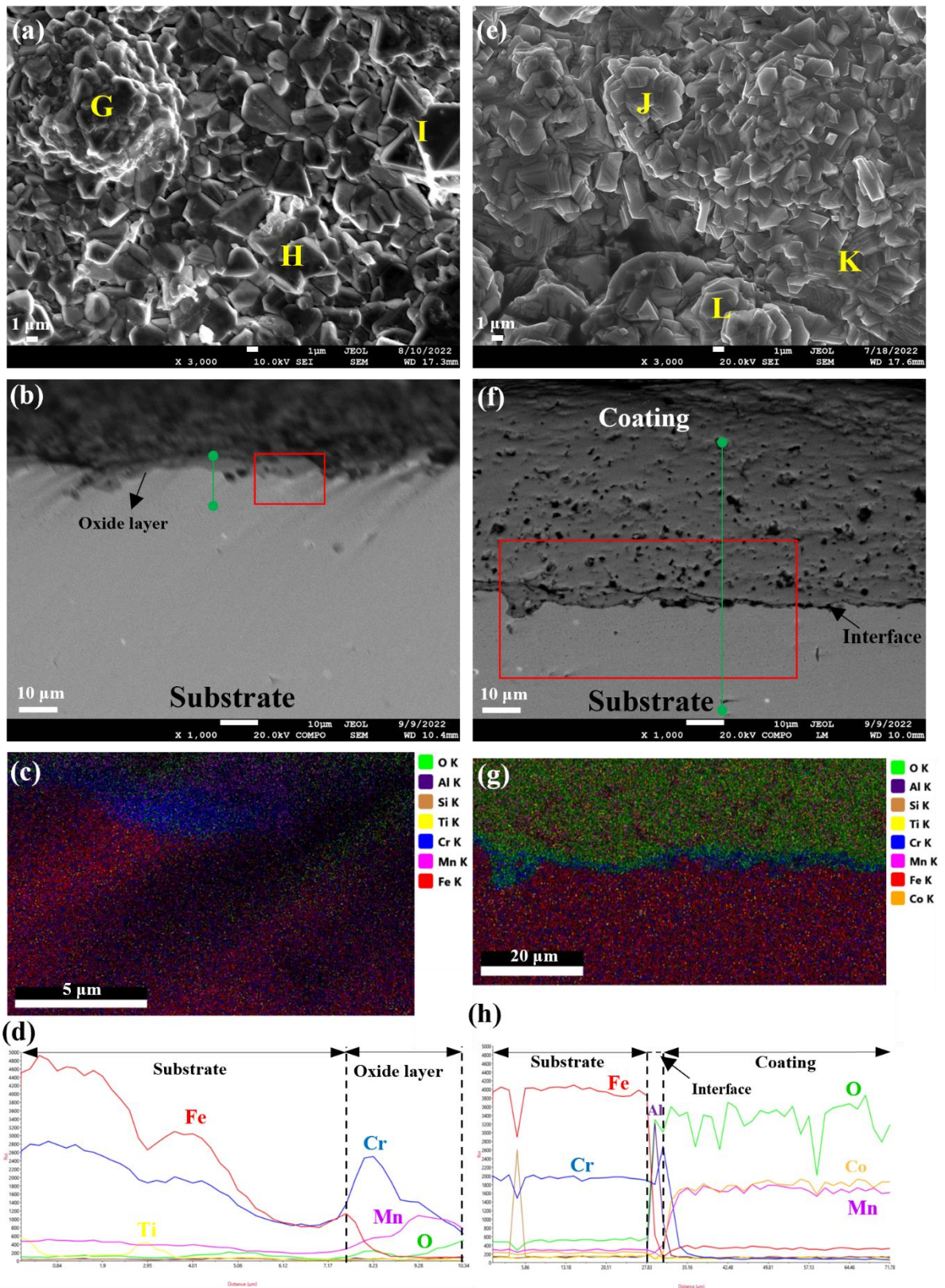


Figure 41: FE-SEM analysis after 200 h oxidation at 850 °C of Crofer 22 APU and MCF coating respectively, (a), (e) surface morphology, (b), (f) back scattered cross-section, (c), (g) elemental mapping, (d), (h) line scan.

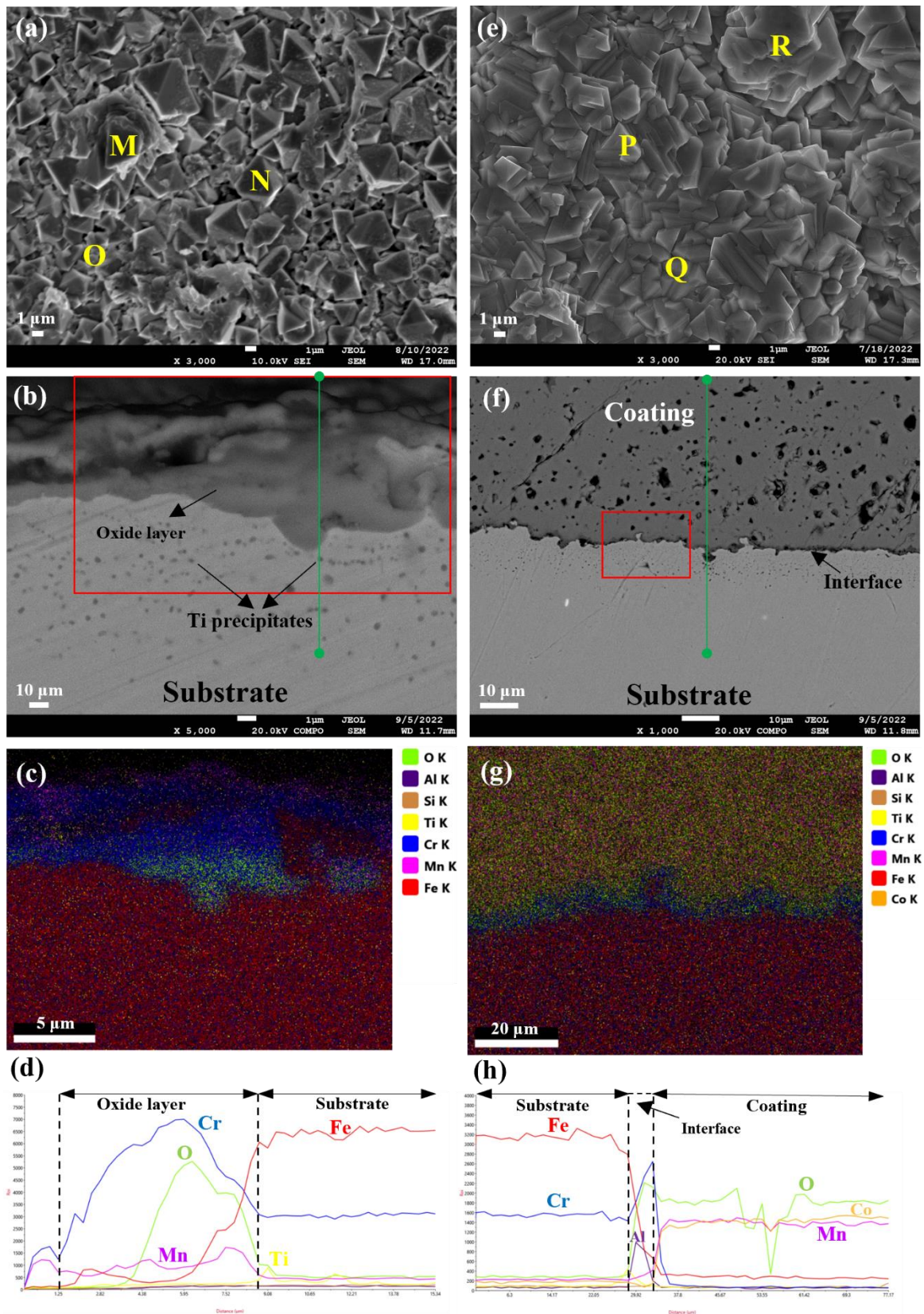


Figure 42: FE-SEM analysis after 400 h oxidation at 850 °C of Crofer 22 APU and MCF coating respectively, (a), (e) surface morphology, (b), (f) back scattered cross-section, (c), (g) elemental mapping, (d), (h) line scan.

Table 14: EDS analysis results of Crofer steel and MCF coating after oxidation at 850 °C as shown in Figures 40, 41 and 42

Oxidation time (h)	Figure No.	Area	Mn (at.%)	Cr (at.%)	Co (at.%)	Fe (at.%)	O (at.%)
50	40	A	17.4	23.5	-	3.6	55.5
		B	18.5	27.0	-	2.5	52.0
		C	19.3	28.8	-	2.5	49.3
		D	1.0	-	41.3	0.1	57.6
		E	1.7	-	40.1	0.4	57.8
		F	1.6	-	44.8	0.2	53.4
200	41	G	20.6	24.7	-	2.2	52.5
		H	21.1	23.5	-	1.8	53.6
		I	22.4	25.1	-	2.4	50.1
		J	2.6	-	33.8	0.0	63.6
		K	3.4	-	36.4	0.1	60.1
		L	2.9	-	31.3	0.0	65.8
400	42	M	14.7	28.9	-	2.0	54.5
		N	17.8	33.1	-	2.4	46.7
		O	15.8	49.9	-	2.2	48.2
		P	1.6	-	45.6	0.2	52.6
		Q	2.9	-	59.1	0.2	59.1
		R	1.4	-	43.2	0.1	55.4

5.5.2. GDOES depth profiling of oxidized Crofer substrate

Figure 43 provides the elemental depth profiles of Crofer 22 APU steel after oxidation at 50, 200, and 400 h at 850 °C. To estimate the oxide layer thickness, an interface has to be determined between the oxide film and the metal, which can be set at a distance where the oxygen signal drops to 50% of its value at the surface (Takeda et al. 2006). In the case of 50 h oxidation, the oxide film/metal interface is determined at about 1.7 μm , indicating the total thickness of the oxide layer. Similarly, the total oxide layer thickness corresponding to 200 h and 400 h oxidation is 3.2 μm and 4.1 μm . Fig. 43a shows the enrichment of Mn and Cr from the top surface. The depth at which the intensity of Mn decreases indicates the MnCr_2O_4 layer thickness, i.e., 0.4 μm , and the Cr_2O_3 layer thickness is about 1.3 μm . In Fig. 43b, the signal of Mn and Cr are seen to be enriched to a larger depth. The estimated thickness of the top MnCr_2O_4 spinel and subscale Cr_2O_3 is about 1 μm and 2.2 μm , respectively. Similarly, in Fig. 43c, the oxide layer thickness of spinel was 2 μm , and that of chromia was 2.1 μm .

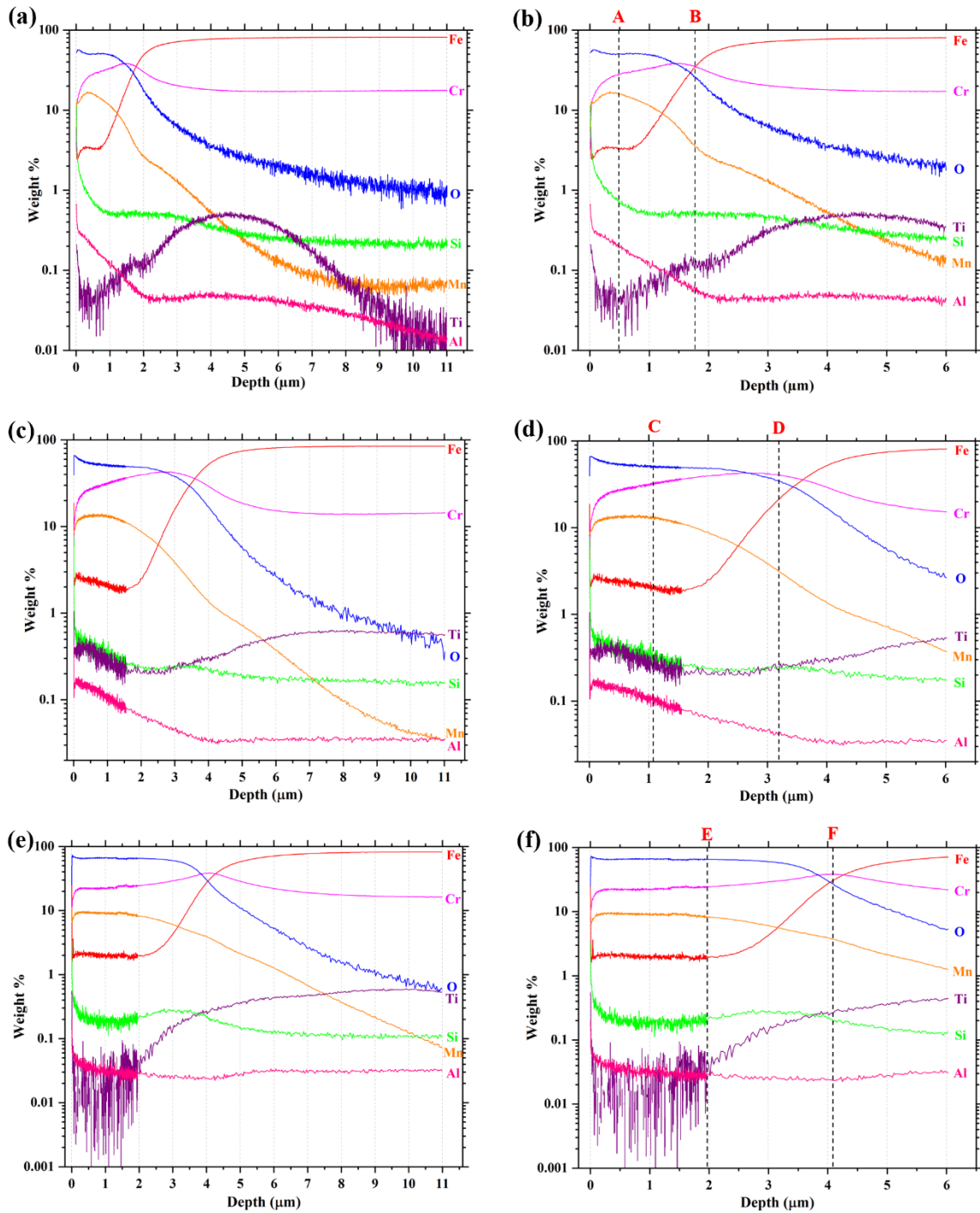


Figure 43: GD-OES depth profiles of Crofer 22 APU, (a) & (b) after 50 h, (c) & (d) after 200 h, (e) & (f) after 400 h [lines A, B, C, D, E, F represents the oxide layer thickness]

The enrichment of Fe and Ti can be seen in the subscale region in all conditions indicating the internal oxidation product of Fe and Ti. The signal of Si is weak at the surface and is seen to enrich in the subscale region, which could also be one of the products of internal oxidation. The depletion of the signal of Al from the surface indicates that no oxides of Al are formed.

5.5.3. X-ray diffraction

The XRD analysis of the oxidized Crofer steel, as shown in Fig. 44a, demonstrates the formation of MnCr_2O_4 spinel and Cr_2O_3 as the primary oxidation products. As the oxidation time increases, the intensity of the diffraction pattern of MnCr_2O_4 spinel and chromia increases, and the intensity of the substrate peaks decreases gradually. This implies that the oxide scales grew thicker or became more uniform with increased oxidation time. The decrease in the intensity of diffraction of the substrate is because of oxidation. It is controlled by the outward diffusion of Mn from the alloy, which depletes the alloying elements at the steel surface (Hua et al. 2010a). Rietveld refinement results of oxidized Crofer steel are detailed in Table 15. The increase in the peak intensity of the MnCr_2O_4 and Cr_2O_3 is supported by the increase in the volume fraction with oxidation time. Similarly, the decrease in the Fe content is due to the faster outward diffusion of Mn through the Cr_2O_3 layer, which depleted the Fe content on the surface of the steel.

The XRD analysis of the MCF coating after oxidation, as shown in Fig. 44b, reveals Co_3O_4 , $(\text{Mn, Co, Fe})_3\text{O}_4$, and CoO as oxidation products. The XRD pattern after 50 h oxidation reveals high intense peaks of the Co_3O_4 cubic spinel phase. As the oxidation time is increased, the relative intensity between Co_3O_4 and $(\text{Mn, Co, Fe})_3\text{O}_4$ decreases. This could be due to the transformation of the CoO phase to spinel. The intensity of $(\text{Mn, Co, Fe})_3\text{O}_4$ increases with the oxidation time. Rietveld refinement results of MCF coating after oxidation, as shown in Table 16, indicates the increase in the $(\text{Mn, Co, Fe})_3\text{O}_4$ phase over the oxidation time, which supports the phase transformation. As the Fe content in the coating is significantly less, the phase can be considered as $(\text{Mn, Co})_3\text{O}_4$.

The effect of oxidation time on the crystallite size of Crofer 22 APU steel and MCF coating was estimated with the Scherrer equation (Equation (8)) with instrument correction using the SiO_2 standard (Khorsand Zak et al. 2011).

It is observed that the crystallite size of α -Fe reduces, whereas the chromia layer formed grows with an increase in oxidation time. But the crystallite size of the MnCr_2O_4 spinel layer is seen to reduce with the oxidation time. Similarly, the crystallite size of CoO and Co_3O_4 decreases, whereas the crystallite size of $(\text{Mn, Co})_3\text{O}_4$ increases with oxidation time. The variation of crystallite size with oxidation is detailed in Table 17.

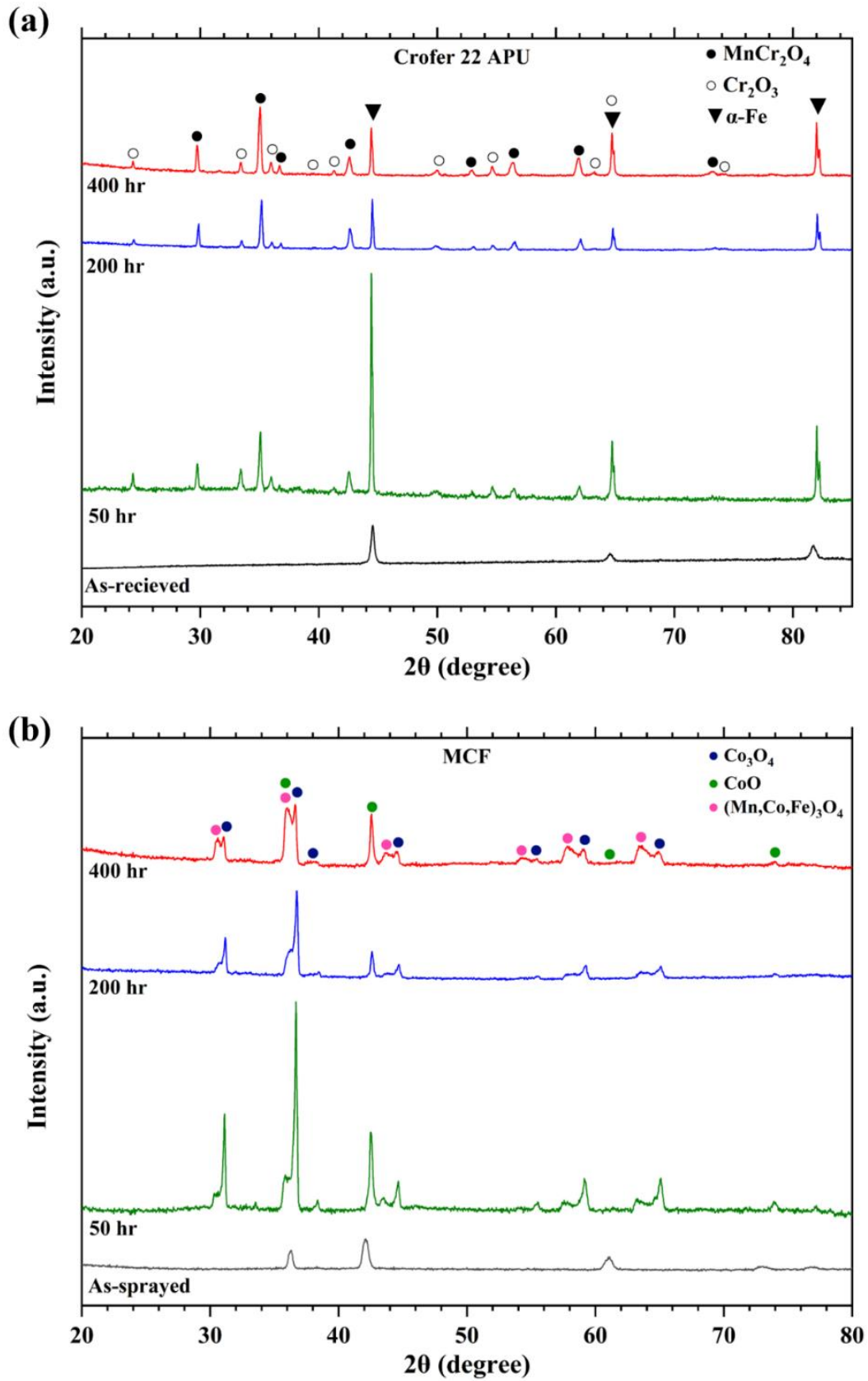


Figure 44: XRD of (a) Crofer 22 APU (b) MCF coating after oxidation at 850 °C

Table 15: Results of Rietveld Refinement made on the XRD patterns of Crofer 22 APU shown in Fig. 44a

Condition	Phases	Lattice constant (Å)	Phase Fraction (%)
As-received	α -Fe	2.8660	100
50 h	MnCr ₂ O ₄	8.4360	12.7
	Cr ₂ O ₃	4.9530	49.7
	α -Fe	2.8710	37.6
200 h	MnCr ₂ O ₄	8.4470	50.7
	Cr ₂ O ₃	4.9580	31.4
	α -Fe	2.8780	17.8
400 h	MnCr ₂ O ₄	8.5110	59.7
	Cr ₂ O ₃	4.9610	25.5
	α -Fe	2.8860	14.8

Table 16: Results of Rietveld Refinement made on the XRD patterns of MCF coating shown in Fig. 44b

Condition	Phases	Lattice constant (Å)	Phase Fraction (%)
As-sprayed	CoO	4.2710	100
50 h	Co ₃ O ₄	8.0820	49.2
	(Mn, Co, Fe) ₃ O ₄	8.2630	34.8
	CoO	4.2400	16.0
200 h	Co ₃ O ₄	8.1100	53.0
	(Mn, Co, Fe) ₃ O ₄	8.2970	37.2
	CoO	4.2580	9.8
400 h	Co ₃ O ₄	8.1290	48.4
	(Mn, Co, Fe) ₃ O ₄	8.3200	40.1
	CoO	4.2670	11.5

Table 17: Crystallite size variation with oxidation time at 850 °C

Condition	Crofer 22 APU (Å)		MCF coating (Å)		
	Cr ₂ O ₃	MnCr ₂ O ₄	CoO	Co ₃ O ₄	(Mn,Co) ₃ O ₄
As-sprayed	-	-	254.5	-	-
50 h	418.75	1679.3	535	568.5	144.3
200 h	711.75	804	693	524.75	134
400 h	857.5	670	597.5	423.75	174

5.5.4. Raman spectroscopy

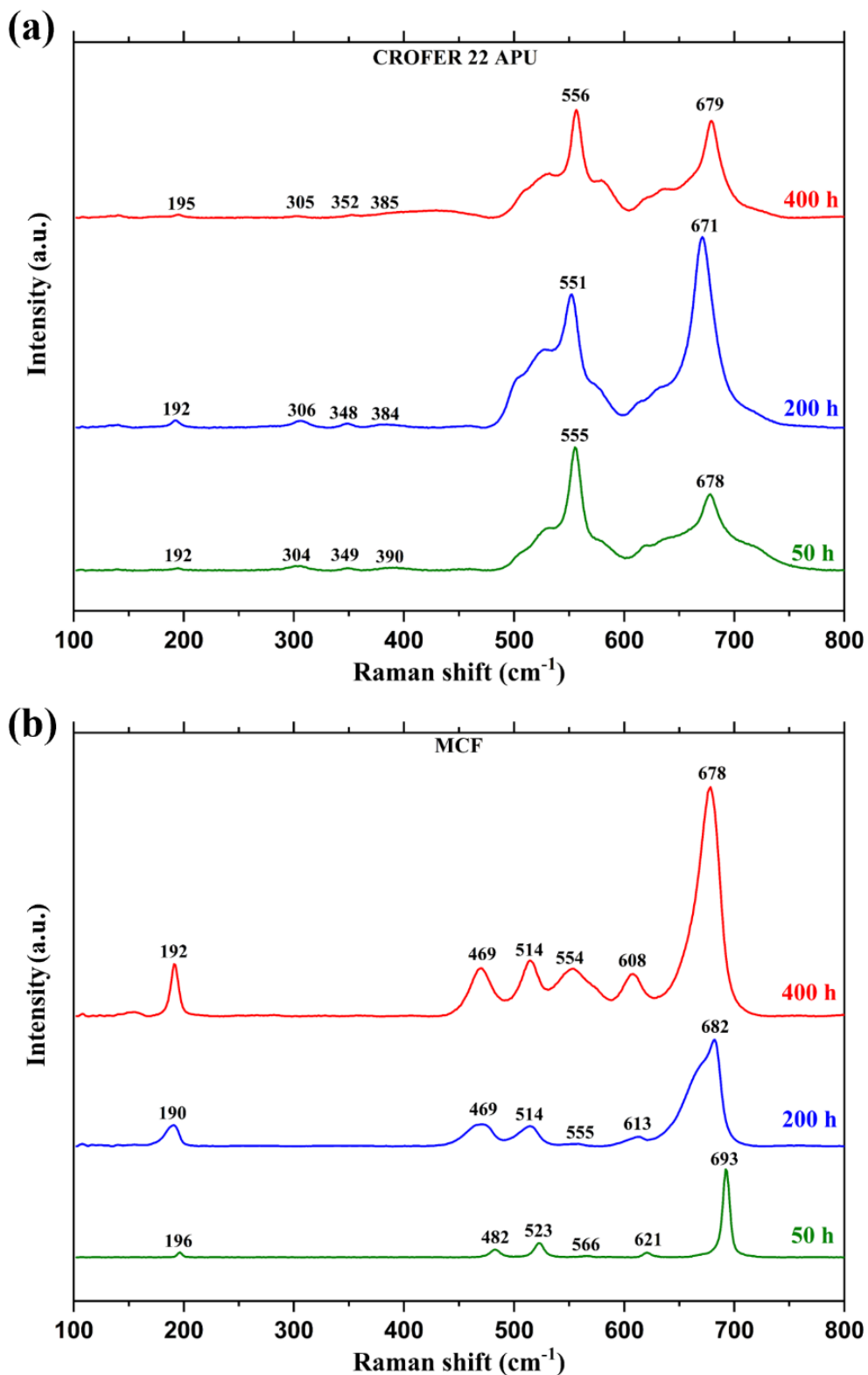


Figure 45: Raman Spectra of (a) Crofer 22 APU (b) MCF coating after oxidation

Figure 45 shows the Raman spectra of the oxidized Crofer steel and MCF coating. In Fig. 45a, the Raman peaks correspond to Cr_2O_3 and $(\text{Mn}, \text{Cr})_3\text{O}_4$ spinel formed on the surface

of Crofer steel after oxidation. The two-layer oxide formation on the Crofer steel can be confirmed from these results. After 50 h oxidation, the peaks of Cr_2O_3 have a higher intensity than those corresponding to the spinel. The Mn-Cr spinel formed is not homogenous compared to the Cr_2O_3 layer. As the oxidation time increases, the thickness of the spinel layer increases (confirmed by FESEM) and becomes more homogeneous. Hence, the effect of both oxide layers can be observed by the intense peaks of Cr_2O_3 at 556 cm^{-1} and Mn-Cr spinel at 679 cm^{-1} after 400 h oxidation. In Fig. 45b, the Raman peaks are dominated by the Co_3O_4 peaks. The growth of the Co_3O_4 layer in the MCF coating can be interpreted by the increase in the intensity of the Raman peaks corresponding to Co_3O_4 with an increase in the oxidation time. The peak at 554, 555, and 566 cm^{-1} can be attributed to the CoO phase (as seen in XRD).

Table 18: Raman spectra observed on the Crofer 22 APU and MCF coating after oxidation for 50, 200, and 400 h at $850\text{ }^\circ\text{C}$.

Observed Raman peak positions (cm^{-1})	Compound	Reference
304, 349, 555 306, 348, 551 305, 352, 556	Cr_2O_3	(Gomes et al. 2017; Mohammad taheri et al. 2018)
192, 390, 678 192, 384, 671 195, 385, 679	$(\text{Mn, Cr})_3\text{O}_4$	(Demeneva et al. 2019; Mazur et al. 2022)
196, 482, 523, 621, 693 190, 469, 514, 613, 682 192, 469, 514, 608, 678	Co_3O_4	(Hadjievl and Vergilovs 1988; Wang et al. 2019)
566 555 554	CoO	(Khalil et al. 2020)

5.5.5. Optical analysis of MCF coating using UV-vis-NIR

The absorbance spectra (Fig. 46) indicate an increase in the absorption in MCF coating with the increase in oxidation time. This increase could be due to the growth of the Co_3O_4 layer on the coating. Similar absorption spectra were observed for Co_3O_4 nanoparticles at $800\text{ }^\circ\text{C}$ (Nasser A. M. Barakat et al. 2008). The average absorbance in the visible range

(380-740 nm) was determined as 0.974, 0.997, and 1.118 for 50, 200, and 400 h oxidation, respectively. As the value indicates, there is a substantial increase in the absorbance of the MCF coating after 400 h oxidation indicating the growth of the oxide layer thickness.

The relationship between the optical density and band gap energy (E_g) is given by the equation: $\alpha h\nu = K (h\nu - E_g)^n$, where α is the absorption coefficient, K is a constant relative to material, $h\nu$ is the photon energy, E_g is the band gap, and n is the value depending on the nature of transition (1/2 for direct and 2 for indirect allowed transition) (Reena et al. 2020). Assuming a direct transition with $n=1/2$, the Tauc plot of $(\alpha h\nu)^2$ as a function of $h\nu$ was plotted to estimate the optical band gap energy of the oxidized samples. The values of $h\nu$ were extrapolated to $\alpha=0$, which approximates the band gap energy.

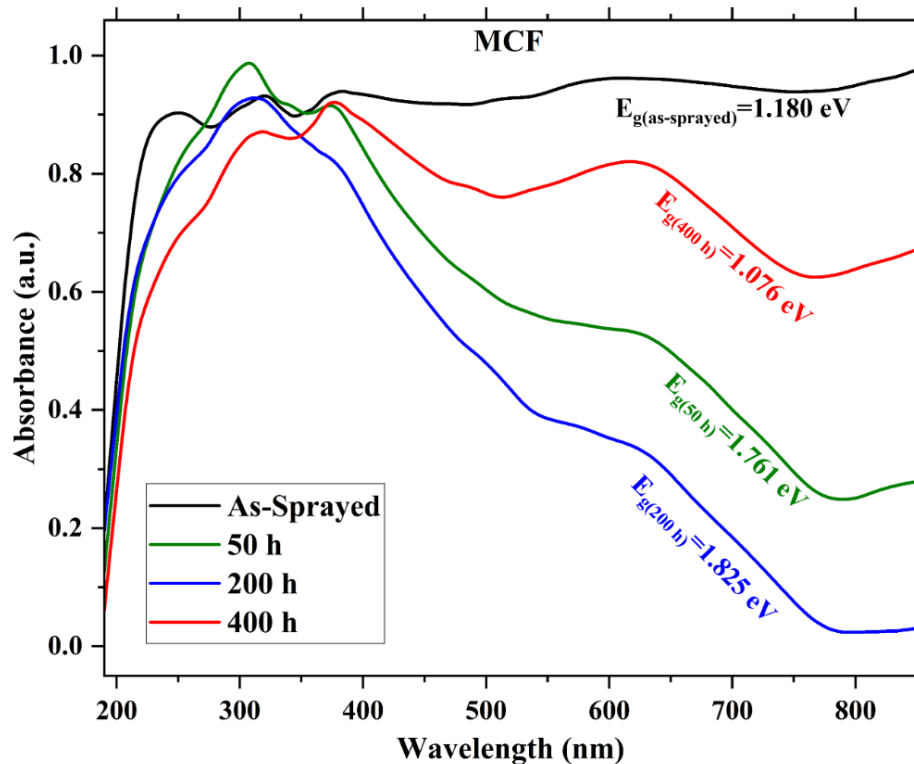


Figure 46: UV-vis-NIR absorbance spectra MCF coating after oxidation at 850 °C mentioning the band gap energy

5.5.6. Oxidation kinetics

Figure 47 shows the specific area weight gain of MCF-coated Crofer 22 APU composite as a function of oxidation time at 850 °C in air. As predicted, the weight gain increases with the oxidation time. In order to study and understand the oxidation kinetics, the square of the area-specific weight gain as a function of oxidation time (Hua et al. 2011; Jian et al. 2006):

$$\left(\frac{\Delta W}{A}\right)^2 = Kt \dots\dots\dots 14$$

where ΔW is the weight gain of the oxidized specimen, A is the surface area of the oxidized sample, K is the parabolic rate constant, and t is the oxidation time.

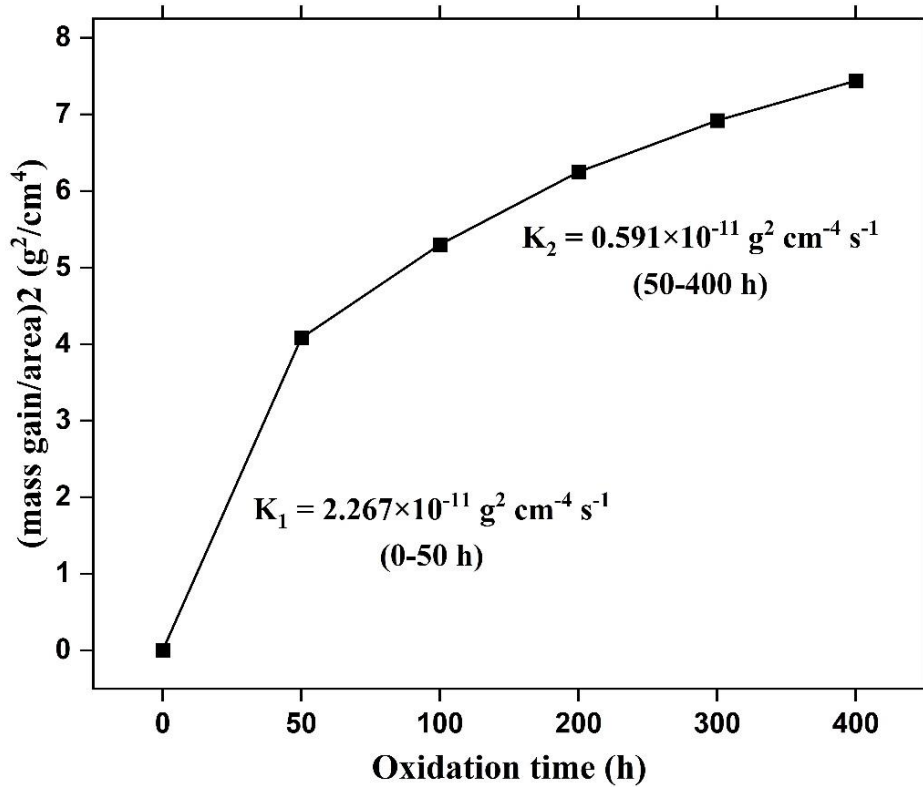


Figure 47: Oxidation kinetics of the MCF-coated Crofer 22 APU composite oxidized at 850 °C in air

The initial rapid oxidation (0-50 h) of MCF-coated Crofer 22 APU steel with a rate constant of $2.267 \times 10^{-11} \text{ g}^2 \text{ cm}^{-4} \text{ s}^{-1}$ was accompanied by a slower oxidation rate with a rate constant of $0.591 \times 10^{-11} \text{ g}^2 \text{ cm}^{-4} \text{ s}^{-1}$ between 50 h and 400 h. A linear rate constant is observed in the initial stage of oxidation upto 50 h. The oxidation rate constant between 50 h and 400 h obeys parabolic law. A similar observation was made in the oxidation behavior of Ni-Mo-Cr alloy, where the transition in oxidation was attributed to the double layer oxide of Mn and Cr formed on the alloy (Hua et al. 2009).

The thickness of oxide layers formed on the Crofer substrate and substrate-coating interface after oxidation at 850 °C for 50, 200, and 400 h are detailed in Table 19. The thickness of the oxide layers was measured from the line scan images obtained from FE-SEM analysis. The measured oxide thickness was used to study the oxide growth kinetics in the Crofer

substrate and coating-substrate interface. The parabolic rate constant for the chromia layer growth is given by the equation (Cruchley et al. 2013):

$$K_p = \frac{\xi^2}{t} \dots\dots\dots 15$$

where ξ is the thickness of the oxide layer formed, and t is oxidation time. Graphs of oxide layer thickness and growth kinetics as a function of oxidation time are plotted as shown in Fig. 48. The oxide layer on the Crofer steel is seen to grow rapidly in the initial 50 h oxidation and stabilizes after 200 h oxidation. The layer is seen to grow further with an increase in oxidation time. But in the substrate-coating interface, the oxide layer's growth is hindered by increased oxidation time.

Table 19: Change in oxide layer thickness and growth kinetics with oxidation time

Oxidation time (h)	Crofer 22 APU		Substrate-Coating Interface	
	Thickness (μm)	$K_p \times 10^{-11}$ (mm/s)	Thickness (μm)	$K_p \times 10^{-11}$ (mm/s)
50	1.82	1.84	3.6	7.20
200	2.75	1.05	3.7	1.90
400	7.44	3.84	4.75	1.57

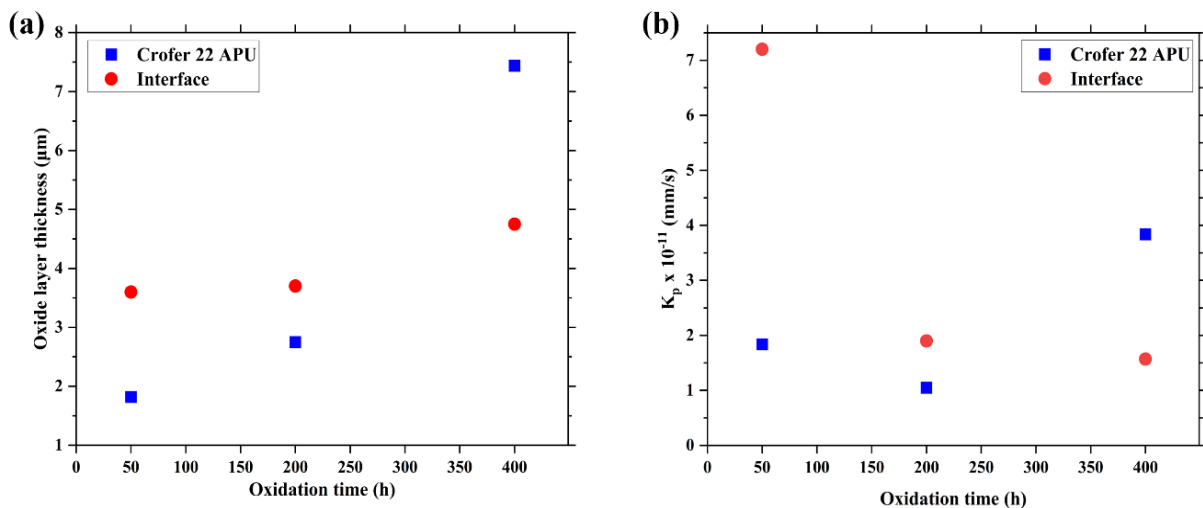


Figure 48: Graphs depicting (a) oxide layer thickness v/s oxidation time and, (b) Oxide growth kinetics v/s oxidation time

5.5.7. Discussion

5.5.7.1 Mechanism of two-layer oxide formation in Crofer 22 APU

Table 20: Energy of formation of oxides at 0 K and 1200 K

Sl. No	Oxides	Structure	Space group	Space group No.	Formation energy at 0 K (kJ/mol)	Gibbs Energy (kJ/mol) at 1200 K
1	α -Al ₂ O ₃	Trigonal	R/3c	167	-331.524	-1295.23
2	SiO ₂	Trigonal	P3_221	154	-315.314	-695.426
3	Cr ₂ O ₃	Trigonal	R/3c	167	-229.732	-818.475
4	MnO	Cubic	Fd/3m	225	-192.295	-297.490 [§]
5	Fe ₂ O ₃	Trigonal	R/3c	167	-183.998	-512.374
6	CuO	Monoclinic	C2/c	15	-91.6611	-49.73
7	MnCr ₂ O ₄	Cubic	Fd/3m	227	-226.934	-1186.4*
8	FeCr ₂ O ₄	Cubic	Fd/3m	227	-217.96	-1061.87*

[§](Jacob et al. 2008) * (Young 2016)

The scales formed on the Crofer 22 APU steel after isothermal oxidation analyzed by SEM-EDS showed a two-layer oxide formation consisting of a thin MnCr₂O₄ spinel top layer and an underlying thick and continuous fine-crystalline Cr₂O₃ layer. The oxide layer formed is seen to adhere well to the substrate material. The phenomenon of the formation of two-layer oxide is due to the fast diffusion of manganese through the chromia grain boundaries. The reaction of manganese with chromia with inward diffusion of oxygen forms the Mn-Cr spinel phase (Atkinson and Gardner 1981; Przybylski et al. 2014; Saeidpour and Ebrahimifar 2021). As seen in the line scan results (Fig. 49, 41, and 42), the two-layer oxide grows with the increase in oxidation time. The presence of Ti (line scan results) confirms the formation of internal oxidation products. It was observed in the oxidation of a Fe-Cr alloy that Ti migrates from metal to the oxide layer due to the high mobility of Ti in Cr₂O₃, which substitutes the Cr ions partially. This Ti migration may lead to the expansion in lattice parameters of Cr₂O₃, which can be observed in shifting XRD peaks to lower angles (Hua et al. 2010a). In the present study, the outward diffusion of Mn and Cr after each oxidation stage leading to the formation and growth of Cr₂O₃ and MnCr₂O₄ was confirmed by the elemental mapping and EDS-line scan along the cross-section, also confirmed by XRD.

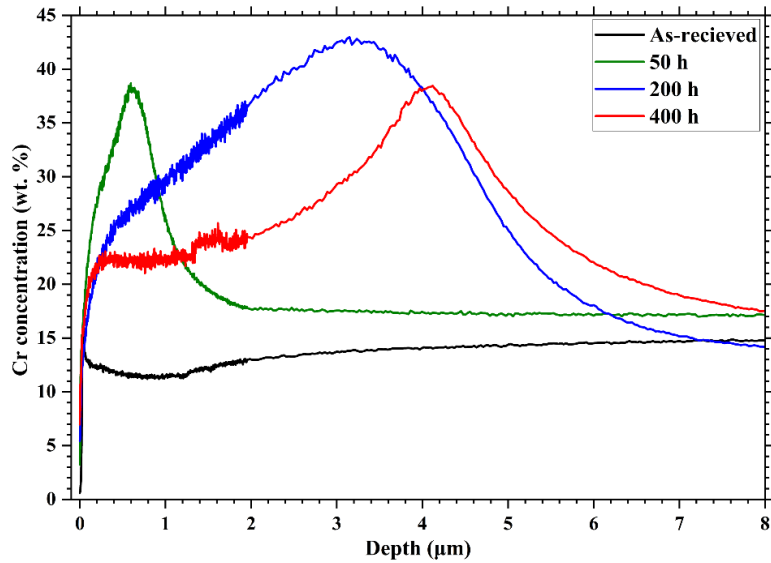


Figure 49: GD-OES Cr-concentration profiles of Crofer 22 APU from the surface after oxidation at 850 °C in air

Figure 49 represents the chromium concentration profile of the oxidized Crofer steel substrate extracted from the GDOES depth profiling. As oxidation time progresses, the depletion of Cr extends more and more into the interior of the substrate due to the increase in the oxide layer thickness. The oxidation resistance of an alloy is designed based on the selective oxidation of the elemental components in the alloy. In an ideal scenario, forming a dense adherent layer of refractory oxides, such as Cr_2O_3 , SiO_2 , or Al_2O_3 , indicates complete selectivity, and oxidation occurs by ionic transport through the oxide scale. This phenomenon of selective oxidation creates a zone within an alloy where the oxidized elements are depleted and significantly affects phase transformation (Evans and Lobb 1984). Below the temperature range of about 700 °C in steels, the diffusion of Cr is not sufficiently fast, and oxide growth is governed by combined diffusion in alloy and oxide (Ostwald and Grabke 2004). In Fig. 49, the chromium-rich layer is dense, restricting the entry of oxidizing species. The oxidation rate is eventually controlled by cation diffusion to the surface. Thus, the enrichment in manganese concentration above the chromia layer depleted (Fig. 43) in the metal (Evans et al. 1980).

The major oxide-forming elements in Crofer 22 APU are Fe, Cr, Mn, Si, Cu, and Al. The formation of oxide depends on the oxygen affinity, which is in the order of $\text{Al} > \text{Si} > \text{Mn} > \text{Cr} > \text{Fe} > \text{Cu}$, which reflects the Density Functional Theory (DFT) based calculation at 0 K and experimental result at 1200K in Table 20. But the growth rate depends on the diffusivity of the alloying elements, which is influenced by the concentration gradient, membrane permeability, temperature, and pressure. The minimum

required oxygen partial pressure for formation oxides is the order of $Al < Si < Mn < Cr < Fe < Cu$ when calculated from the Ellingham diagram. The formation of Al_2O_3 and SiO_2 , which were seen only during long-term oxidation, is ruled out in this study due to their lower concentration (Mitchell et al. 1998) (“NIST-JANAF Thermochemical Tables”). The Gibbs free energy change for the formation of $MnCr_2O_4$ is -1231.7 kJ/mol of O_2 (Swaminathan et al. 2014) (-1186.4 kJ/mol of O_2 (Young 2016)), and that of Cr_2O_3 is -818.475 kJ/mol of O_2 (Table. 20). The free energy of formation of $MnCr_2O_4$ suggests that the Mn-Cr spinel is more stable than the Cr_2O_3 . Though $MnCr_2O_4$ spinel is a less protective oxide layer than Cr_2O_3 , the $MnCr_2O_4$ has more affinity for the formation than Cr_2O_3 because of the rapid diffusion of Mn than Cr to the top surface (Rao et al. 2020).

The solubility and outward diffusion of Mn and Fe cation over Cr_2O_3 forms the spinel as supported by Raman Spectroscopy. The spinel is observed on the surface of the Cr_2O_3 during the initial oxidation stage despite the low concentration of Mn for the following reason (Young 2016):

- i. $MnCr_2O_4$ is more stable than MnO
- ii. Mn is soluble in Cr_2O_3 of max. 1.6 wt.% at 1000 °C.
- iii. Mn diffuses rapidly through lattice than grain boundary diffusion

As per the first principle calculations at 0 K (Young 2016)



The diffusion of Mn over chromia occurs rapidly despite the stability of MnO as per the equation (16) reaction given above. In addition, Mn diffuses two order magnitude of Fe in Cr_2O_3 (Lobnig et al. 1992; Wild 1977). Hence, $MnCr_2O_4$ dominated $FeCr_2O_4$. Hence, in XRD and Raman spectroscopy, Al_2O_3 , SiO_2 , and MnO were not observed.

Figure 50 shows the proposed oxidation mechanism in Crofer 22 APU steel and MCF-coated steel at 850 °C for varying oxidation times. The oxides formed on the Crofer steel consisted of chromia and Mn-Cr spinel, while the oxides formed in the coating-substrate interface consisted of a chromia layer. The mechanism proposes that in the uncoated part of the steel, the oxygen intake increases, and Cr and Mn diffusion from the substrate to the surface increases with oxidation time. Hence, growth in both chromia and the Mn-Cr spinel

layer thickness is observed. The crystallite size of chromia increase with oxidation, as seen in Table 17. The decrease in the crystallite size of Mn-Cr spinel as a function of oxidation time is attributed to the evaporation of chromium on the substrate, which is not protected by the coating. The rate of evaporation is higher for prolonged oxidation time (Asensio-Jimenez et al. 2013).

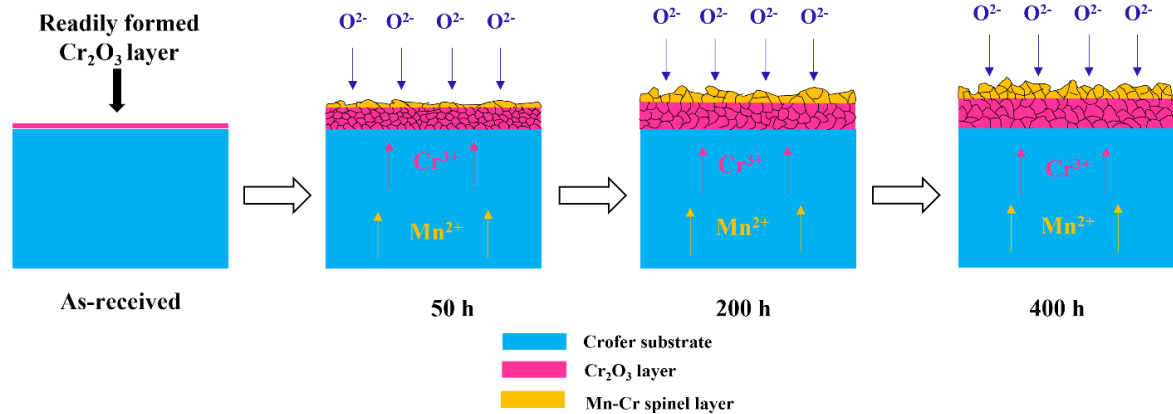
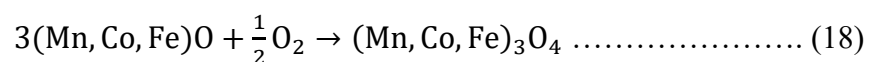


Figure 50: Proposed mechanism of two-layer oxide formation during oxidation in uncoated Crofer steel

5.5.7.2 Effect of MCF coating on the oxidation resistance of Crofer 22 APU

Achieving dense coating when spraying oxide ceramics is difficult, and the same has been seen in the microstructure of as-sprayed MCF spinel. MCF has been an interesting material that exhibits self-healing characteristics upon volume expansion during phase transformation (Grünwald et al. 2017). The oxidation of MCF coating at 850 °C for 50, 200, and 400 h revealed the formation of (Mn, Fe, Co)₃O₄ spinel as the major phase in the analysis of XRD data. Due to the low content of Fe in the coating, the coating system can be considered an Mn-Co-O system for better estimation (Back et al. 2020). Sintering of the coating is visible, and the micro-cracks are completely healed with a decrease in porosity substantially. However, larger globular pores are still seen even after 400 h oxidation. A crack-healing phenomenon studied in the annealing of APS-MCF coating showed that phase transformation of rock-salt configuration of as-sprayed coating to spinel phase led to porosity decrease and increase in the gas-tightness. This phase transformation is given by the equation (Grünwald et al. 2017):



The uptake of oxygen by the MCF coating surface during the heat treatment, which faces a high oxygen partial pressure, leads to volume expansion, decreasing the porosity. This phenomenon leads to the closure of the cracks in the coating. Self-healing cracks and

subsequent densification prevent the oxygen from reaching the substrate, reducing the alloying elements from diffusing out of the substrate. Once the tiny micro-cracks are closed, they block the flow of gas into the substrate, creating a significantly low oxygen partial pressure near the coating-substrate interface. Therefore, further oxidation proceeds via solid-state diffusion, reducing the oxidation speed (Grünwald et al. 2017). Hence, the APS-MCF coating on Crofer steel can act as an effective diffusion barrier for SOFC interconnect and diminish the Cr-evaporation from the steel. In the present study, the reduction in the average porosity of the MCF coating was analyzed from the cross-section images. Also, the line scan and elemental mapping clearly depict that the coating has successfully reduced the diffusion of Cr from the substrate.

The MCF-coated interface consists of oxides of Cr and Al, as confirmed from the line scan, and the growth of the interface oxide layer is due to the diffusion of Cr and Al from the steel substrate. The formation of alumina is due to the difference in partial pressure from the coating surface to the interface. When the uncoated Crofer substrate is exposed to an oxidation environment, due to high oxygen partial pressure, chromia and Mn-Cr spinel form with a faster growth rate; hence, alumina formation was not observed. But due to low partial pressure on the coated side of the substrate, Al diffuses near the coating-substrate interface, and alumina is formed adjacent to the substrate below the chromia layer. The formation of alumina was confirmed from the line scan where the signal of alumina and oxygen enriches adjacent to the substrate (Fig. 40h, 41h, 42h). Similar observations were found in a study of the oxidation behavior of alumina-forming austenitic and high entropy alloys at 1200 °C. The equilibrium oxygen partial pressures calculated for different oxides in the temperature range of 900-1300 °C show that at 900 °C, the partial pressure for the formation of Al₂O₃ is very low compared to Cr₂O₃ formation (Shi et al. 2020).

The self-healing mechanism of MCF coating is observed by the densification of the coating, where the micro-cracks present in the as-sprayed condition diminish with the increase in oxidation time. The crack-healing mechanism occurs in the coating due to the transformation of the CoO phase into Co₃O₄ and (Mn, Co)₃O₄ spinel on the coating surface. The transformation of CoO to spinel and the growth of the spinels can be observed in the Rietveld refinement of XRD data. The Rietveld refinement data (Table 16) shows a decrease in the phase fraction of the CoO phase and an increase in the phase fraction of the spinel phase. The phase fraction of spinel also stabilizes over the oxidation time, indicating the majority of the CoO phase is transformed into spinel.

The oxidation kinetics of Crofer 22 APU usually follow parabolic law/trend, which is also obvious in the present study. However, the oxidation rate is significantly higher in the grooved Crofer substrate with machined gas flow channels in this study than in the other reported earlier (Przybylski et al. 2014). It should be noted that the thickness of the substrate plays a crucial role in deciding the oxidation rate and kinetics. The lower the thickness of the sample, the higher the oxidation rate (Asensio-Jimenez et al., 2013). The thickness of the interconnect used in the present study is about 3 mm with the ridge and 2 mm without the ridge. As seen in Fig. 47, the initial oxidation of MCF-coated Crofer steel up to 50 h accelerates with a rate constant of $2.267 \times 10^{-11} \text{ g}^2 \text{ cm}^{-4} \text{ s}^{-1}$, followed by slower steady oxidation up to 400 h. In the study of Fe-Ni-Co spinel oxide coated on Crofer 22 APU by sol-gel method, a large weight gain was seen within the first 100 h (Saeidpour and Ebrahimifar 2021). The $(\text{Mn}, \text{Cr})_3\text{O}_4$ spinel and Mn_2O_3 scale formed on the alloys was expected to reduce the Cr-poisoning (Geng et al. 2006). The oxidation kinetics could be fitted to a near-parabolic relationship with time as the diffusion of the ions through the oxide scale controls the growth of the oxide scale (Chen et al. 2005). The oxide scale thickness measured with an increase in oxidation time (Fig. 48a) on the oxidized Crofer substrate and coating-substrate interface shows that the coating has efficiently reduced the diffusion of Cr from the substrate. Hence, the MCF coating successfully reduced the Cr-evaporation from the Crofer substrate.

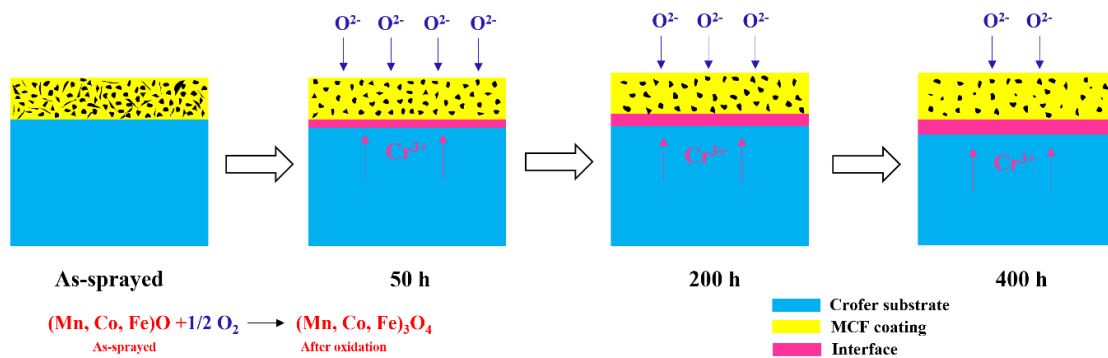


Figure 51: Proposed mechanism of oxidation in MCF-coated Crofer steel

Figure 51 shows the proposed oxidation mechanism for MCF-coated steel at 850 °C for varying oxidation times. The MCF coating substantially reduces the oxygen intake of the substrate. Therefore, the growth of the oxide at the coating-substrate interface is hindered. As per the EDS line scan, the thickness of the oxide layer is less in the substrate-coating interface than on the uncoated surface. This phenomenon is caused by the crack-healing tendency of the coating, which was seen to heal the micro-cracks as a function of time and reduce porosity. The crack-healing of the coating also induces densification of the coating.

The Raman spectra (Fig. 45) showed the formation of oxides of Cr and Mn-Cr spinel on the surface of Crofer steel and also detected mainly Co_3O_4 spinel on the MCF coating. As seen in the Raman spectra, a shift in the peaks can be observed in all the spectra. This peak shift is caused by changes in chemical composition (cation substitution) and structure variations (Chen et al. 2007). The intense Raman peak of chromia was observed at 555, 551, and 556 cm^{-1} for 50, 200, and 400 h, respectively. Small shifts in the main band observed at 555 cm^{-1} are due to the distortion of the chromia crystallite structure caused by the partial doping effect (Madern et al. 2018; Srisrual et al. 2009). The oxidation time increases the thickness of the oxide layers formed, increasing the Raman peak intensity. A similar observation was made in the study of Crofer steel interconnect extracted from SOFC stacks operated up to 20000 h (Ghiara et al. 2021).

The MCF has also been designed for good electrical conductivity while acting as a Cr-diffusion barrier. The MCF coating is known to exhibit crack-healing characteristics, which seem to be beneficial in increasing the electrical conductivity of the coating. The determined band gap (E_g) for MCF coating is 1.180, 1.761, 1.825, and 1.076 eV for as-sprayed, 50, 200, and 400 h oxidation conditions, respectively. The band gap in the coating can be attributed to the charge transfer process (valence to conduction band excitation) from oxygen to cobalt ions (Xu and Zeng 2004). Co_3O_4 is the most stable phase in the Co-O system, with a mixed-valence compound ($\text{Co}^{\text{II}}\text{Co}^{\text{III}}\text{O}_4$) having a normal spinel structure (Barreca et al. 2001). $\text{Co}^{\text{II}+}$ occupies tetrahedral sites, and $\text{Co}^{\text{III}+}$ occupies the octahedral sites. The electrical property of stoichiometric Co_3O_4 is due to a small exchange in the ion charge states among the two sites (Makhlouf et al., 2013). In the study of absorbance spectra of Cobalt oxide thin film, absorption at $\lambda=730$ nm and $\lambda<500$ nm was attributed to ligand-metal charge transfer (LMCT) (events $\text{O}(-\text{II}) \rightarrow \text{Co}(\text{III})$ and $\text{O}(-\text{II}) \rightarrow \text{Co}(\text{II})$). Here, the ligand is ions, and metal charges are $\text{Co}^{\text{II}+}$ and $\text{Co}^{\text{III}+}$ ions.

The conduction band has a contribution from mainly Co^{II} 3d orbitals. The Co^{III} centres present in Co_3O_4 induce a sub-band inside the energy gap. This phenomenon yields two-band gap energies (Barreca et al. 2001). In the present study, only one band gap energy could be evaluated. The band gap energy was sufficient for understanding the variation in the electrical conductivity of the coating. As the band gap energy decreases after 400 h oxidation, the growth of spinel oxides on the coating (estimated by Rietveld refinement) and the increase in the electrical conductivity of the coating can be confirmed. A thin film of Co_3O_4 deposited on a glass substrate by the sol-gel spin coating technique was studied

for its electrical conductivity and band gap energy. A decrease in the band gap energy and an increase in the electrical conductivity were observed. The effect of crystallite size on the band gap energy was studied on Co_3O_4 thin film for varying annealing times. It was observed that an increase in the crystallite size decreases the band gap (Patil et al. 2012). Therefore, an initial increase in the band gap can be attributed to the phase transformation of CoO to Co_3O_4 . The band gap increases from 1.761 to 1.825, where a decrease in the crystallite size of Co_3O_4 is seen. After 400 h oxidation, the band gap energy decreases to 1.076 eV, which could be ascribed to the growth of $(\text{Mn}, \text{Co})_3\text{O}_4$ spinel. A 'red shift' in the band gap energy was reported, which was attributed to an increase in the crystallite size of ZnSe films after annealing (Chaparro et al. 2000). As time progressed, most of the phase fraction was acquired by transforming CoO to Co_3O_4 and $(\text{Mn}, \text{Co})_3\text{O}_4$ spinels. In the present study, the UV-vis-NIR interpretation was found to be an effective approach for the oxidation resistance of Crofer 22 APU and the effect of plasma-sprayed MCF coating.

6. CONCLUSIONS

Atmospheric plasma sprayed $\text{Mn}_{1.0}\text{Co}_{1.9}\text{Fe}_{0.1}\text{O}_4$ spinel coating deposited on Crofer 22 APU ferritic stainless steel SOFC interconnect have been studied in detail to examine their structural, physio-thermal, and thermal integrity. The following conclusions were drawn:

1. The APS coating on the surface (line of sight) of the ridges/grooves of the substrate was uniform. However, the thickness was uneven on the side walls. The MCF coatings were comprised of micro-cracks and porosities. No variation in the microstructural features of the as-deposited surface and cross-sections was observed. The decrease in the electrical resistance of MCF coating as a function of temperature revealed its suitability for high-temperature operations of SOFC.
2. The adhesion strength of MCF coating on Crofer 22 APU steel was found to be in the range of 30 to 36 N, evaluated by scratch indentation test under progressive and constant loading conditions.
3. The early-stage oxidation of Crofer 22 APU revealed the formation of Cr_2O_3 and MnCr_2O_4 . The depth profiling has confirmed the two-layer oxide on the surface of Crofer steel, discontinuous top spinel layer MnCr_2O_4 was 100 nm, while the continuous subscale Cr_2O_3 layer had a thickness of 150 nm.
4. MCF coating exhibited comparable thermal expansion to the Crofer 22 APU steel; therefore, the thermal expansion mismatch is insignificant. Marginally higher thermal expansion of MCF coating than Crofer steel results in compressive stresses at the interface. The thermal mismatch between the Crofer substrate and MCF protective coating is significant, only above 700 °C.
5. The effect of MCF coating on the long term oxidation resistance of Crofer 22 APU steel at 850 °C showed the formation of a two-layer oxide scale on the Crofer steel consisting of a thin MnCr_2O_4 spinel top layer and an underlying thick and continuous fine-crystalline Cr_2O_3 layer. The phase transformation of CoO to Co_3O_4 and the increase in phase fraction of Co_3O_4 spinel over oxidation time leads to crack-healing and densification of MCF coating. The densification of MCF coating acts as an effective diffusion barrier to mitigate the chromium evaporation from the Crofer 22 APU steel.

6.1. Scope for future work

1. The effect of thermal spray coating processes like High velocity oxy-fuel (HVOF) and Detonation gun (D-Gun), can be attempted to achieve dense coatings.
2. The MCF coating thickness can be varied by APS process and assessed for its adhesion and long term oxidation exposure.
3. The long term oxidation up to 2000 h can be performed to study the microstructural changes, phase transformation, property changes of substrate and coating.
4. The potential alternative for Crofer 22 APU steel substrate, e.g. Ni-based superalloy, can be studied with MCF protective coating due to Crofer steel being expensive.
5. Surface remelting with laser remelting process of the MCF coating can be examined.

REFERENCES

- Achilli, E., Annoni, F., Armani, N., Patrini, M., Cornelli, M., Celada, L., Micali, M., Terrasi, A., Ghigna, P., and Timò, G. (2022). “Capabilities of Grazing Incidence X-ray Diffraction in the Investigation of Amorphous Mixed Oxides with Variable Composition.” *Materials*, 15(6), 2144.
- Advisor, M., and Aindow, M. (2012). “Evaluation of Solid Oxide Fuel Cell Interconnect Coatings : Reaction Layer Microstructure , Chemistry and Formation Mechanisms Neal Magdefrau.” *Thesis Proposal*, (May).
- Alvarez, E., Meier, A., Weil, K. S., and Yang, Z. (2011). “Oxidation kinetics of manganese cobaltite spinel protection layers on Sanergy HT for solid oxide fuel cell interconnect applications.” *Int J Appl Ceram Technol*, 8(1), 33–41.
- Amendola, R., Gannon, P., Ellingwood, B., Hoyt, K., Piccardo, P., and Genocchio, P. (2012). “Oxidation behavior of coated and preoxidized ferritic steel in single and dual atmosphere exposures at 800°C.” *Surf Coat Technol*, 206(8–9), 2173–2180.
- Antolino, G., Piotrkowski, R., José, R., Amado, C., Teresa, G.-H. M., and Enrique, C. (n.d.). “Acoustic Emission Technique To Assess Microfractures of Metallic Coatings With Scratch-Tests.” 2–7.
- Ariharan, S., and Maurya, R. (2021). “Assessment of plasma sprayed carbon nanotube reinforced Al₂O₃-based nanocomposite with micro-scratching.” *Surf Coat Technol*, 418(April), 127216.
- Asensio-Jimenez, C., Niewolak, L., Hattendorf, H., Kuhn, B., Huczowski, P., Singheiser, L., and Quadackers, W. J. (2013). “Effect of specimen thickness on the oxidation rate of high chromium ferritic steels: The significance of intrinsic alloy creep strength.” *Oxidation of Metals*, 79(1–2), 15–28.
- Atkinson, A., and Gardner, J. W. (1981). “The Diffusion of Fe³⁺ in amorphous SiO₂, and the protective properties of SiO₂ layers.” *Corros Sci*, 21, 49–58.
- Aukrust, E., and Muan, A. (1963). “Phase Relations in the System Cobalt Oxide-Manganese Oxide in Air.” *Journal of The American Ceramic Society*, 46(10), 511.

Back, H. C., Gibmeier, J., and Vaßen, R. (2020). “Phase Transformation-Induced Changes in Microstructure and Residual Stresses in Thermally Sprayed MnCoFeO₄ Protective Coatings.” *Journal of Thermal Spray Technology*, 29(6), 1242–1255.

Barletta, M., Tagliaferri, V., Gisario, A., and Venettacci, S. (2013). “Progressive and constant load scratch testing of single- and multi-layered composite coatings.” *Tribol Int*, 64, 39–52.

Barreca, D., Massignan, C., Daolio, S., Fabrizio, M., Piccirillo, C., Armelao, L., and Tondello, E. (2001). “Composition and microstructure of cobalt oxide thin films obtained from a novel cobalt(II) precursor by chemical vapor deposition.” *Chemistry of Materials*, 13(2), 588–593.

Basak, M., Rahman, M. L., Ahmed, M. F., Biswas, B., and Sharmin, N. (2022). “The use of X-ray diffraction peak profile analysis to determine the structural parameters of cobalt ferrite nanoparticles using Debye-Scherrer, Williamson-Hall, Halder-Wagner and Size-strain plot: Different precipitating agent approach.” *J Alloys Compd*, 895.

Bastidas, D. M. (2006). “High temperature corrosion of metallic interconnects in solid oxide fuel cells.” *Revista de Metalurgia (Madrid)*, 42(6), 425–443.

Bednarz, M., Molin, S., Bobruk, M., Stygar, M., Długoń, E., Sitarz, M., and Brylewski, T. (2019). “High-temperature oxidation of the Crofer 22 H ferritic steel with Mn_{1.45}Co_{1.45}Fe_{0.10}O₄ and Mn_{1.5}Co_{1.5}O₄ spinel coatings under thermal cycling conditions and its properties.” *Mater Chem Phys*, 225, 227–238.

Bejarano, M. L., Valarezo, A., Lara-Curzio, E., and Sampath, S. (2019). “Dilation Behavior of Thermal Spray Coatings.” *Journal of Thermal Spray Technology*, Springer.

Bi, Z. H., Zhu, J. H., Du, S. W., and Li, Y. T. (2013). “Effect of alloy composition on the oxide scale formation and electrical conductivity behavior of Co-plated ferritic alloys.” *Surf Coat Technol*, 228, 124–131.

Bianco, M., Linder, M., Larring, Y., Greco, F., and herle, J. Van. (2017). *Lifetime Issues for Solid Oxide Fuel Cell Interconnects. Solid Oxide Fuel Cell Lifetime and Reliability: Critical Challenges in Fuel Cells*, Elsevier Ltd.

Bianco, M., Tallgren, J., Hong, J. E., Yang, S., Himanen, O., Mikkola, J., herle, J. Van, and Steinberger-Wilckens, R. (2019). “Ex-situ experimental benchmarking of solid oxide fuel cell metal interconnects.” *J Power Sources*, 437, 226900.

Bik, M., Galetz, M., Dąbrowa, J., Mrocza, K., Zając, P., Gil, A., Jeleń, P., Gawęda, M., Owińska, M., Stygar, M., Zajusz, M., Wyrwa, J., and Sitarz, M. (2022). “Polymer Derived Ceramics based on SiAlOC glasses as novel protective coatings for ferritic steel.” *Appl Surf Sci*, 576(September 2021).

Boháč, P., Tomáščík, J., Čtvrtlík, R., Dráb, M., Koula, V., Cvrk, K., and Jastrabík, L. (2014). “Acoustic Emission Generated during Scratch Test of Various Thin Films.” *Journal of Nondestructive Testing*, Vol.19(12).

Bordeneuve, H., Tenailleau, C., Guillemet-Fritsch, S., Smith, R., Suard, E., and Rousset, A. (2010). “Structural variations and cation distributions in $Mn_{3-x}Co_xO_4$ ($0 \leq x \leq 3$) dense ceramics using neutron diffraction data.” *Solid State Sci*, 12(3), 379–386.

Brylewski, T., Molin, S., Marczyński, M., Mazur, Domaradzki, K., Kryshstal, O., and Gil, A. (2021). “Influence of Gd deposition on the oxidation behavior and electrical properties of a layered system consisting of Crofer 22 APU and $MnCo_2O_4$ spinel.” *Int J Hydrogen Energy*, 46(9), 6775–6791.

Bull, S. J. (1991). “Failure modes in scratch adhesion testing.” *Surf Coat Technol*, 50(1), 25–32.

Bull, S. J., and Berasetegui, E. G. (2006). “An overview of the potential of quantitative coating adhesion measurement by scratch testing.” *Tribol Int*, 39(2), 99–114.

Byon, E., Lee, S. W., Kitamura, J., and Holmberg, K. (2013). “Adhesion/cohesion strength of plasma sprayed ceramic coatings by scratch testing on cross-section.” *Proceedings of the International Thermal Spray Conference*, (January), 516–519.

Cernuschi, F., Lorenzoni, L., Ahmaniemi, S., Vuoristo, P., and Mäntylä, T. (2005). “Studies of the sintering kinetics of thick thermal barrier coatings by thermal diffusivity measurements.” *J Eur Ceram Soc*, 25(4), 393–400.

Chaparro, A. M., Martõ Ánez, M. A., Ân, C. G., Ân, R. B., Gutie Árez, M. T., and Herrero, J. (2000). “ SnO_2 substrate effects on the morphology and composition of chemical bath deposited ZnSe thin films.” *Thin Solid Films*, 361–362, 177–182.

- Chawla, K. K. (2012). "Interfaces." *Composite Materials, Science and Engineering*, Springer, 105–133.
- Chen, G., Xin, X., Luo, T., Liu, L., Zhou, Y., Yuan, C., Lin, C., Zhan, Z., and Wang, S. (2015). "Mn_{1.4}Co_{1.4}Cu_{0.2}O₄ spinel protective coating on ferritic stainless steels for solid oxide fuel cell interconnect applications." *J Power Sources*, 278, 230–234.
- Chen, H., Liu, Y., Gao, Y., Tao, S., and Luo, H. (2010a). "Design, preparation, and characterization of graded YSZ/La 2Zr₂O₇ thermal barrier coatings." *Journal of the American Ceramic Society*, 93(6), 1732–1740.
- Chen, L., Sun, E. Y., Yamanis, J., and Magdefrau, N. (2010b). "Oxidation Kinetics of Mn_{1.5}Co_{1.5}O₄-Coated Haynes 230 and Crofer 22 APU for Solid Oxide Fuel Cell Interconnects." *J Electrochem Soc*, 157(6), B931.
- Chen, X., Hou, P. Y., Jacobson, C. P., Visco, S. J., and Jonghe, L. C. de. (2005). "Protective coating on stainless steel interconnect for SOFCs: Oxidation kinetics and electrical properties." *Solid State Ion*, 176(5–6), 425–433.
- Chen, Y., Liu, Z., Ringer, S. P., Tong, Z., Cui, X., and Chen, Y. (2007). "Selective oxidation synthesis of MnCr₂O₄ spinel nanowires from commercial stainless steel foil." *Cryst Growth Des*, 2279–2281.
- Chiu, Y. T., Lin, C. K., and Wu, J. C. (2011). "High-temperature tensile and creep properties of a ferritic stainless steel for interconnect in solid oxide fuel cell." *J Power Sources*, 196(4), 2005–2012.
- Church, B. C., Sanders, T. H., Speyer, R. F., and Cochran, J. K. (2005). "Interconnect thermal expansion matching to solid oxide fuel cells." *J Mater Sci*, 40, 4893–4898.
- Corsepius, N. C., DeVore, T. C., Reisner, B. A., and Warnaar, D. L. (2007). "Using Variable Temperature Powder X-ray Diffraction To Determine the Thermal Expansion Coefficient of Solid MgO." *J Chem Educ*, 84(5), 818–821.
- Cox, M. G. C., McEnaney, B., and Scott, V. D. (1975). "Kinetics of initial oxide growth on Fe-Cr alloys and the role of vacancies in film breakdown." *Philosophical Magazine*, 31(2), 331–338.

Cruchley, S., Evans, H. E., Taylor, M. P., Hardy, M. C., and Stekovic, S. (2013). "Chromia layer growth on a Ni-based superalloy: Sub-parabolic kinetics and the role of titanium." *Corros Sci*, 75, 58–66.

Damage, M., During, M., Of, T., Coatings, H., and Hard, O. N. (1989). "Major damage mechanisms during scratch and wear testing of hard coatings on hard substrates." 181, 555–564.

Daniel, R., Holec, D., Bartosik, M., Keckes, J., and Mitterer, C. (2011). "Size effect of thermal expansion and thermal/intrinsic stresses in nanostructured thin films: Experiment and model." *Acta Mater*, 59(17), 6631–6645.

Das, B., Nath, A., and Bandyopadhyay, P. P. (2019). "Scratch resistance and damage mechanism of laser remelted thermally sprayed ceramic coating." *Surf Coat Technol*, 364(February), 157–169.

Das, D. K., Srivastava, M. P., Joshi, S. V., and Sivakumar, R. (1991). "Scratch adhesion testing of plasma-sprayed yttria-stabilized zirconia coatings." *Surf Coat Technol*, 46(3), 331–345.

Davis, J. R. (2004). *Handbook of Thermal Spray Technology. Technology (Singap World Sci)*.

Demeneva, N. v., Kononenko, O. v., Matveev, D. v., Kharton, V. v., and Bredikhin, S. I. (2019). "Composition-gradient protective coatings for solid oxide fuel cell interconnectors." *Mater Lett*, 240, 201–204.

Devendra, B. K., Praveen, B. M., Tripathi, V. S., Nagaraju, G., Nagaraju, D. H., and Nayana, K. O. (2021). "Highly corrosion resistant platinum-rhodium alloy coating and its photocatalytic activity." *Inorg Chem Commun*, 134, 109065.

Ding, X., Cui, C., and Guo, L. (2009). "Thermal expansion and electrochemical performance of La_{0.7}Sr_{0.3}CuO_{3-δ}-Sm_{0.2}Ce_{0.8}O_{2-δ} composite cathode for IT-SOFCs." *J Alloys Compd*, 481(1–2), 845–850.

Durda, E., Przybylski, K., and Matsuda, K. (2020). "High-temperature oxidation behavior of the Crofer 22 APU steel coated with (La,Sr)(Co,Fe)O₃ film prepared by pulsed laser deposition." *Thin Solid Films*, 712, 138316.

- Elmer, J. W., Palmer, T. A., Babu, S. S., and Specht, E. D. (2005). “Low temperature relaxation of residual stress in Ti-6Al-4V.” *Scr Mater*, 52(10), 1051–1056.
- Espallargas, N. (2015). *Introduction to thermal spray coatings. Future Development of Thermal Spray Coatings: Types, Designs, Manufacture and Applications*, Elsevier Ltd.
- Evans, H. E., Hilton, D. A., Holm, R. A., and Webster, S. J. (1980). “The Development of Localized Pits During Stainless Steel Oxidation.” *Oxidation of Metals*, 14(3), 235–247.
- Evans, H. E., and Lobb, R. C. (1984). “Alloy depletion profiles during non-protective oxidation.” *Corros Sci*, 24(3), 223–236.
- Falk-Windisch, H., Claquesin, J., Sattari, M., Svensson, J. E., and Froitzheim, J. (2017). “Co- and Ce/Co-coated ferritic stainless steel as interconnect material for Intermediate Temperature Solid Oxide Fuel Cells.” *J Power Sources*, 343, 1–10.
- Fergus, J. W. (2005). “Metallic interconnects for solid oxide fuel cells.” *Materials Science and Engineering A*, 397(1–2), 271–283.
- Fergus, J. W. (2007). “Effect of cathode and electrolyte transport properties on chromium poisoning in solid oxide fuel cells.” *Int J Hydrogen Energy*, 32(16), 3664–3671.
- Gan, L., Montero, X., Sheikh, S. A., Saeki, I., and Murakami, H. (2021). “Microstructure and area specific resistance of cathodic half cells for solid oxide fuel cells composed of perovskite-type cathodes and Co-alloy-coated ferritic stainless steel interconnects.” *Surf Coat Technol*, 406(November 2020), 126659.
- Garcia-Fresnillo, L., Niewolak, L., Quadackers, W. J., and Meier, G. H. (2018). “Influence of Alloying Elements on the Behavior of Different Ferritic Steels as Candidate Materials for SOFC Interconnect.” *Oxidation of Metals*, 89(1–2), 61–80.
- Gazdzicki, P., Morawietz, T., Hiesgen, R., Arnold, J., and Friedrich, K. A. (2016). “Protective coatings on stainless steel bipolar plates for proton exchange membrane (PEM) electrolyzers.” *J Power Sources*, 307, 815–825.
- Geng, S. J., Zhu, J. H., and Lu, Z. G. (2006). “Evaluation of several alloys for solid oxide fuel cell interconnect application.” *Scr Mater*, 55(3), 239–242.

- Geng, S., Zhao, Q., Li, Y., Mu, J., Chen, G., Wang, F., and Zhu, S. (2017). "Sputtered MnCu metallic coating on ferritic stainless steel for solid oxide fuel cell interconnects application." *Int J Hydrogen Energy*, 42(15), 10298–10307.
- Ghiara, G., Piccardo, P., Bongiorno, V., Repetto, L., Geipel, C., and Spotorno, R. (2021). "Characterization of metallic interconnects extracted from Solid Oxide Fuel Cell stacks operated up to 20,000 h in real life conditions: The fuel side." *Int J Hydrogen Energy*, 46(46), 23815–23827.
- Ghosh, S., Kumar, M. K., and Kain, V. (2013). "High temperature oxidation behavior of AISI 304L stainless steel - Effect of surface working operations." *Appl Surf Sci*, 264, 312–319.
- Gkanas, E. I., Damian, A., Ioannidou, A., Stoian, G., Lupu, N., Gjoka, M., and Makridis, S. S. (2019). "Synthesis, characterisation and hydrogen sorption properties of mechanically alloyed $Mg(Ni_{1-x}Mn_x)_2$." *Mater Today Energy*, 13, 186–194.
- Gomes, A. S. O., Yaghini, N., Martinelli, A., and Ahlberg, E. (2017). "A micro-Raman spectroscopic study of $Cr(OH)_3$ and Cr_2O_3 nanoparticles obtained by the hydrothermal method." *Journal of Raman Spectroscopy*, 48(10), 1256–1263.
- Grünwald, N., Sebold, D., Sohn, Y. J., Menzler, N. H., and Vaßen, R. (2017). "Self-healing atmospheric plasma sprayed $Mn_{1.0}Co_{1.9}Fe_{0.1}O_4$ protective interconnector coatings for solid oxide fuel cells." *J Power Sources*, 363, 185–192.
- Grünwald, N., Sohn, Y. J., Yin, X., Menzler, N. H., Guillon, O., and Vaßen, R. (2019). "Microstructure and phase evolution of atmospheric plasma sprayed Mn-Co-Fe oxide protection layers for solid oxide fuel cells." *J Eur Ceram Soc*, 39(2–3), 449–460.
- Hadad, M., Marot, G., Démarécaux, P., Chicot, D., Lesage, J., Rohr, L., and Siegmann, S. (2007). "Adhesion tests for thermal spray coatings: Correlation of bond strength and interfacial toughness." *Surface Engineering*, 23(4), 279–283.
- Hadjiev, V. G., and Vergilovs, I. v. (1988). "The Raman spectra of Co_3O_4 ." *Journal of Physics C Solid State Physics*, 21((7)), 199–201.
- Halvarsson, M., Langer, V., and Vuorinen, S. (1995). "Determination of the thermal expansion of $\kappa-Al_2O_3$ by high temperature XRD." *Surf Coat Technol*, 76–77, 358–362.

- Han, M., Peng, S., Wang, Z., Yang, Z., and Chen, X. (2007). "Properties of Fe-Cr based alloys as interconnects in a solid oxide fuel cell." *J Power Sources*, 164(1), 278–283.
- Hasegawa, M. (2013). *Ellingham Diagram. Treatise on Process Metallurgy*, Elsevier Ltd.
- Hassan, M. A., Mamat, O. bin, and Mehdi, M. (2020). "Review: Influence of alloy addition and spinel coatings on Cr-based metallic interconnects of solid oxide fuel cells." *Int J Hydrogen Energy*, Elsevier Ltd.
- Hazra, S., and Bandyopadhyay, P. P. (2012). "Scratch induced failure of plasma sprayed alumina based coatings." *Mater Des*, 35, 243–250.
- Horita, T. (2021). "Chromium poisoning for prolonged lifetime of electrodes in solid oxide fuel cells - Review." *Ceram Int*, 47(6), 7293–7306.
- Horita, T., Xiong, Y., Yamaji, K., Sakai, N., and Yokokawa, H. (2003). "Stability of Fe-Cr alloy interconnects under CH₄-H₂O atmosphere for SOFCs." *J Power Sources*, 118(1–2), 35–43.
- Hosseini, N., Abbasi, M. H., Karimzadeh, F., and Choi, G. M. (2015). "Development of Cu_{1.3}Mn_{1.7}O₄ spinel coating on ferritic stainless steel for solid oxide fuel cell interconnects." *J Power Sources*, 273, 1073–1083.
- Hosseini, S. N., Karimzadeh, F., Enayati, M. H., and Sammes, N. M. (2016). "Oxidation and electrical behavior of CuFe₂O₄ spinel coated Crofer 22 APU stainless steel for SOFC interconnect application." *Solid State Ion*, 289, 95–105.
- Hu, Y. Z., Su, Y. T., Li, C. X., Li, C. J., and Yang, G. J. (2020). "Dense Mn_{1.5}Co_{1.5}O₄ coatings with excellent long-term stability and electrical performance under the SOFC cathode environment." *Appl Surf Sci*, 499, 143726.
- Hua, B., Kong, Y., Zhang, W., Pu, J., Chi, B., and Jian, L. (2011). "The effect of Mn on the oxidation behavior and electrical conductivity of Fe-17Cr alloys in solid oxide fuel cell cathode atmosphere." *J Power Sources*, 196(18), 7627–7638.
- Hua, B., Lu, F., Zhang, J., Kong, Y., Pu, J., Chi, B., and Jian, L. (2009). "Oxidation Behavior and Electrical Property of a Ni-Based Alloy in SOFC Anode Environment." *J Electrochem Soc*, 156(10), B1261.

- Hua, B., Pu, J., Lu, F., Zhang, J., Chi, B., and Jian, L. (2010a). "Development of a Fe-Cr alloy for interconnect application in intermediate temperature solid oxide fuel cells." *J Power Sources*, 195(9), 2782–2788.
- Hua, B., Zhang, W., Wu, J., Pu, J., Chi, B., and Jian, L. (2010b). "A promising NiCo₂O₄ protective coating for metallic interconnects of solid oxide fuel cells." *J Power Sources*, 195(21), 7375–7379.
- Huang, W., Gopalan, S., Pal, U. B., and Basu, S. N. (2008). "Evaluation of Electrophoretically Deposited CuMn_{1.8}O₄ Spinel Coatings on Crofer 22 APU for Solid Oxide Fuel Cell Interconnects." *J Electrochem Soc*, 155(11), B1161.
- Hui, R., Wang, Z., Kesler, O., Rose, L., Jankovic, J., Yick, S., Maric, R., and Ghosh, D. (2007). "Thermal plasma spraying for SOFCs: Applications, potential advantages, and challenges." *J Power Sources*, 170(2), 308–323.
- Huntz, A. M., Maréchal, L., Lesage, B., and Molins, R. (2006). "Thermal expansion coefficient of alumina films developed by oxidation of a FeCrAl alloy determined by a deflection technique." *Appl Surf Sci*, 252(22), 7781–7787.
- Jacob, K. T., Kumar, A., and Waseda, Y. (2008). "Gibbs energy of formation of MnO: Measurement and assessment." *J Phase Equilibria Diffus*, 29(3), 222–230.
- Jamali, H., Mozafarinia, R., Shoja Razavi, R., and Ahmadi-Pidani, R. (2012). "Comparison of thermal shock resistances of plasma-sprayed nanostructured and conventional yttria stabilized zirconia thermal barrier coatings." *Ceram Int*, 38(8), 6705–6712.
- Jaworski, R., Pawlowski, L., Roudet, F., Kozerski, S., and Petit, F. (2008). "Characterization of mechanical properties of suspension plasma sprayed TiO₂ coatings using scratch test." *Surf Coat Technol*, 202(12), 2644–2653.
- Jian, P., Jian, L., Bing, H., and Xie, G. (2006). "Oxidation kinetics and phase evolution of a Fe-16Cr alloy in simulated SOFC cathode atmosphere." *J Power Sources*, 158(1), 354–360.
- Jiang, S. P., Zhang, J. P., and Zheng, X. G. (2002). "A comparative investigation of chromium deposition at air electrodes of solid oxide fuel cells." *J Eur Ceram Soc*, 22, 361–373.

Kamalan Kirubaharan, A. M., Kuppusami, P., Chakravarty, S., Ramachandran, D., and Singh, A. (2017). "Thermal expansion and residual stress behaviour of electron beam evaporated yttria stabilized zirconia films on Inconel-690 substrates." *J Alloys Compd*, 722, 585–592.

Kandeva-Ivanova, M., Vencl, A., and Karastoyanov, D. (2016). *Advanced Tribological Coatings For Heavy-Duty Applications: Case Studies*.

Kaschel, F. R., Vijayaraghavan, R. K., Shmeliov, A., McCarthy, E. K., Canavan, M., McNally, P. J., Dowling, D. P., Nicolosi, V., and Celikin, M. (2020). "Mechanism of stress relaxation and phase transformation in additively manufactured Ti-6Al-4V via in situ high temperature XRD and TEM analyses." *Acta Mater*, 188, 720–732.

Khalil, A. T., Ovais, M., Ullah, I., Ali, M., Shinwari, Z. K., and Maaza, M. (2020). "Physical properties, biological applications and biocompatibility studies on biosynthesized single phase cobalt oxide (Co₃O₄) nanoparticles via *Sageretia thea* (Osbeck)." *Arabian Journal of Chemistry*, 13(1), 606–619.

Khan, A. N., and Lu, J. (2007). "Thermal cyclic behavior of air plasma sprayed thermal barrier coatings sprayed on stainless steel substrates." *Surf Coat Technol*, 201(8), 4653–4658.

Khan, M. A., Anand, A. V., Duraiselvam, M., Rao, K. S., Singh, R. A., and Jayalakshmi, S. (2021). "Thermal shock resistance and thermal insulation capability of laser-glazed functionally graded lanthanum magnesium hexaluminate/yttria-stabilised zirconia thermal barrier coating." *Materials*, 14(14), 3865.

Khor, K. A., Dong, Z. L., and Gu, Y. W. (1999). "Plasma sprayed functionally graded thermal barrier coatings." *Mater Lett*, 38(6), 437–444.

Khor, K. A., and Gu, Y. W. (2000). "Thermal properties of plasma-sprayed functionally graded thermal barrier coatings." *Thin Solid Films*, 372(1–2), 104113.

Khorsand Zak, A., Abd. Majid, W. H., Abrishami, M. E., and Yousefi, R. (2011). "X-ray analysis of ZnO nanoparticles by Williamson-Hall and size-strain plot methods." *Solid State Sci*, 13(1), 251–256.

Kruk, A., Schabikowski, M., Mitura-Nowak, M., and Brylewski, T. (2020). "Magnetic and electrical properties of Mn₂CoO₄ spinel." *Physica B Condens Matter*, 596.

Kustov, S., Golyandin, S., Sapozhnikov, K., Vincent, A., Maire, E., and Lormand, G. (2001). "Structural and transient internal friction due to thermal expansion mismatch between matrix and reinforcement in Al-SiC particulate composite." *Materials Science and Engineering*, 313(1–2), 218–226.

Lech Pawlowski. (2008). *The Science and Engineering of Thermal Spray Coatings: Second Edition. Science and engineering of thermal spray coating*, John Wiley & Sons, Ltd.

Liu, Y., Fergus, J. W., Wang, K., and Cruz, C. dela. (2013). "Crystal Structure, Chemical Stabilities and Electrical Conductivity of Fe-Doped Manganese Cobalt Spinel Oxides for SOFC Interconnect Coatings." *J Electrochem Soc*, 160(11), F1316–F1321.

Lobnig, R. E., Schmidt, H. P., Hennesen, K., and Grabke, H. J. (1992). "Diffusion of cations in chromia layers grown on iron-base alloys." *Oxidation of Metals*, 37(1–2), 81–93.

Loghman-Estarki, M. R., Shoja Razavi, R., Edris, H., Pourbafrany, M., Jamali, H., and Ghasemi, R. (2014). "Life time of new SYSZ thermal barrier coatings produced by plasma spraying method under thermal shock test and high temperature treatment." *Ceram Int*, 40(1 PART B), 1405–1414.

Londoño-Restrepo, S. M., Herrera-Lara, M., Bernal-Alvarez, L. R., Rivera-Muñoz, E. M., and Rodríguez-García, M. E. (2020). "In-situ XRD study of the crystal size transition of hydroxyapatite from swine bone." *Ceram Int*, 46(15), 24454–24461.

Machkova, M., Zwetanova, A., Kozhukharov, V., and Raicheva, S. (2008). "Thermodynamic Treatment of Chromium Evaporation From Steel SOFC Interconnects." *Journal of the University of Chemical Technology and Metallurgy*, 43(1), 53–58.

Madern, N., Monnier, J., Baddour-Hadjean, R., Steckmeyer, A., and Joubert, J. M. (2018). "Characterization of refractory steel oxidation at high temperature." *Corros Sci*, 132, 223–233.

Magdefrau, N. (2013). "Evaluation of Solid Oxide Fuel Cell Interconnect Coatings: Reaction Layer Microstructure, Chemistry and Formation Mechanisms." *Doctoral Dissertations*, 106.

- Magdefrau, N. J., Chen, L., Sun, E. Y., and Aindow, M. (2013). "Effects of alloy heat treatment on oxidation kinetics and scale morphology for crofer 22 APU." *J Power Sources*, 241, 756–767.
- Mah, J. C. W., Muchtar, A., Somalu, M. R., and Ghazali, M. J. (2017). "Metallic interconnects for solid oxide fuel cell: A review on protective coating and deposition techniques." *Int J Hydrogen Energy*, 42(14), 9219–9229.
- Makhlouf, S. A., Bakr, Z. H., Aly, K. I., and Moustafa, M. S. (2013). "Structural, electrical and optical properties of Co₃O₄ nanoparticles." *Superlattices Microstruct*, 64, 107–117.
- Marra, W. C., Eisenberger, P., and Cho, A. Y. (1979). "X-ray total-external-reflection-Bragg diffraction: A structural study of the GaAs-Al interface." *J Appl Phys*, 50(11), 6927–6933.
- Masi, A., Bellusci, M., McPhail, S. J., Padella, F., Reale, P., Hong, J. E., Steinberger-Wilckens, R., and Carlini, M. (2017). "The effect of chemical composition on high temperature behaviour of Fe and Cu doped Mn-Co spinels." *Ceram Int*, 43(2), 2829–2835.
- Mazur, Ł., Ignaczak, J., Bik, M., Molin, S., Sitarz, M., Aleksander Gil, and Brylewski, T. (2022). "Effectiveness of a dual surface modification of metallic interconnects for application in energy conversion devices." *Int J Hydrogen Energy*, 47(9), 6295–6311.
- Meena, P. L., Kumar, R., and Sreenivas, & K. (2018). "Structural, elastic and magnetic properties of spinel Co₃O₄." *Indian Journal of Pure & Applied Physics*, 56, 890–895.
- Megel, S., Girdauskaite, E., Sauchuk, V., Kusnezoff, M., and Michaelis, A. (2011). "Area specific resistance of oxide scales grown on ferritic alloys for solid oxide fuel cell interconnects." *J Power Sources*, 196(17), 7136–7143.
- Miguel-Pérez, V., Martínez-Amesti, A., Nó, M. L., Larrañaga, A., and Arriortua, M. I. (2012). "Oxide scale formation on different metallic interconnects for solid oxide fuel cells." *Corros Sci*, 60, 38–49.
- Miguel-Pérez, V., Martínez-Amesti, A., Nó, M. L., Larrañaga, A., and Arriortua, M. I. (2013). "The effect of doping (Mn,B)₃O₄ materials as protective layers in different metallic interconnects for Solid Oxide Fuel Cells." *J Power Sources*, 243, 419–430.
- Mitchell, D. R. G., Young, D. J., and Kleemann, W. (1998). "Caburisation of heat-resistant steels." *Materials and Corrosion - Werkstoffe und Korrosion*, 49(4), 231–236.

Mohamed, S. M., Sanad, M. M. S., Mattar, T., El-Shahat, M. F., Rossignol, C., Dessemond, L., Zaidat, K., and Obbade, S. (2022). “The structural, thermal and electrochemical properties of $\text{MnFe}_{1-x-y}\text{Cu}_x\text{Ni}_y\text{CoO}_4$ spinel protective layers in interconnects of solid oxide fuel cells (SOFCs).” *J Alloys Compd*, 923.

Mohammad taheri, M., Yang, Q., Li, Y., and Corona-Gomez, J. (2018). “The effect of deposition parameters on the structure and mechanical properties of chromium oxide coatings deposited by reactive magnetron sputtering.” *Coatings*, 8(3).

Molin, S., Chen, M., and Hendriksen, P. V. (2014). “Oxidation study of coated Crofer 22 APU steel in dry oxygen.” *J Power Sources*, 251, 488–495.

Molin, S., Jasinski, P., Mikkelsen, L., Zhang, W., Chen, M., and Hendriksen, P. v. (2016). “Low temperature processed MnCo_2O_4 and $\text{MnCo}_{1.8}\text{Fe}_{0.2}\text{O}_4$ as effective protective coatings for solid oxide fuel cell interconnects at 750 °C.” *J Power Sources*, 336, 408–418.

Montero, X., Tietz, F., Sebold, D., Buchkremer, H. P., Ringuede, A., Cassir, M., Laresgoiti, A., and Villarreal, I. (2008). “ $\text{MnCo}_{1.9}\text{Fe}_{0.1}\text{O}_4$ spinel protection layer on commercial ferritic steels for interconnect applications in solid oxide fuel cells.” *J Power Sources*, 184(1), 172–179.

Morán-Ruiz, A., Vidal, K., Larrañaga, A., Porrás-Vázquez, J. M., Slater, P. R., and Arriortua, M. I. (2015). “Evaluation of using protective/conductive coating on Fe-22Cr mesh as a composite cathode contact material for intermediate solid oxide fuel cells.” *Int J Hydrogen Energy*, 40(14), 4804–4818.

Mortalò, C., Santoru, A., Pistidda, C., Rebollo, E., Boaro, M., Leonelli, C., and Fabrizio, M. (2019). “Structural evolution of $\text{BaCe}_{0.65}\text{Zr}_{0.20}\text{Y}_{0.15}\text{O}_{3-\delta}\text{-Ce}_{0.85}\text{Gd}_{0.15}\text{O}_{2-\delta}$ composite MPEC membrane by in-situ synchrotron XRD analyses.” *Mater Today Energy*, 13, 331–341.

Mougin, J., Bihan, T. le, and Lucazeau, G. (2001). “High-pressure study of Cr_2O_3 obtained by high-temperature oxidation by X-ray diffraction and Raman spectroscopy.” *Journal of Physics and Chemistry of Solids*, 62(3), 553–563.

N. Manjunath, and B. Rajasekaran. (2022). “Surface Characterization of $\text{Mn}_{1.0}\text{Co}_{1.9}\text{Fe}_{0.1}\text{O}_4$ (MCF) spinel coating on metallic interconnect used in solid oxide

fuel cells.” *Proceedings of Fifth International Conference on Inventive Material Science Applications*, 277–284.

Naka, S., Inagaki, M., and Tanaka, T. (1972). *On the Formation of Solid Solution in Co₃M_nxO₄ System*. *J Mater Sci*, 441–444.

Nakajo, A., Stiller, C., Härkegård, G., and Bolland, O. (2006). “Modeling of thermal stresses and probability of survival of tubular SOFC.” *J Power Sources*, 158(1), 287–294.

Naoumidis, A., Schulze, H. A., Jungen, W., and Lersch, P. (1991). “Phase studies in the chromium-manganese-titanium oxide system at different oxygen partial pressures.” *J Eur Ceram Soc*, 7(1), 55–63.

Nasser A. M. Barakat, Myung Seob Khil, Faheem A. Sheikh||, and Hak Yong Kim. (2008). “Synthesis and Optical Properties of Two Cobalt Oxides (CoO and Co₃O₄) Nanofibers Produced by Electrospinning Process.” *The Journal of Physical Chemistry C*, 112(32), 12225–12233.

Nelis, T., and Pallosi, J. (2006). “Glow discharge as a tool for surface and interface analysis.” *Appl Spectrosc Rev*, 41(3), 227–258.

Niewolak, L., Tietz, F., and Quadackers, W. J. (2016). “Interconnects.” *High-Temperature Solid Oxide Fuel Cells for the 21st Century: Fundamentals, Design and Applications: Second Edition*, 195–254.

Niewolak, L., Wessel, E., Singheiser, L., and Quadackers, W. J. (2010). “Potential suitability of ferritic and austenitic steels as interconnect materials for solid oxide fuel cells operating at 600°C.” *J Power Sources*, 195(22), 7600–7608.

Niewolak, L., Young, D. J., Hattendorf, H., Singheiser, L., and Quadackers, W. J. (2014). “Mechanisms of Oxide Scale Formation on Ferritic Interconnect Steel in Simulated Low and High pO₂ Service Environments of Solid Oxide Fuel Cells.” *Oxidation of Metals*, 82(1), 123–143.

“NIST-JANAF Thermochemical Tables.” (n.d.). <<https://janaf.nist.gov/janbanr.html>> (May 3, 2022).

Nohava, J., Bonferroni, B., Bolelli, G., and Lusvarghi, L. (2010). “Interesting aspects of indentation and scratch methods for characterization of thermally-sprayed coatings.” *Surf Coat Technol*, 205(4), 1127–1131.

- Ostwald, C., and Grabke, H. J. (2004). "Initial oxidation and chromium diffusion. I. Effects of surface working on 9-20% Cr steels." *Corros Sci*, 46(5), 1113–1127.
- Öztürk, B., Topcu, A., and Cora, Ö. N. (2021). "Influence of processing parameters on the porosity, thermal expansion, and oxidation behavior of consolidated Fe22Cr stainless steel powder." *Powder Technol*, 382, 199–207.
- Öztürk, B., Topcu, A., Öztürk, S., and Cora, Ö. N. (2018). "Oxidation, electrical and mechanical properties of Crofer®22 solid oxide fuel cell metallic interconnects manufactured through powder metallurgy." *Int J Hydrogen Energy*, 43(23), 10822–10833.
- Pan, J., Leygraf, C., Jargelius-Pet, R. F. A., and Lindeâ, J. (1998). "Characterization of High-Temperature Oxide Films on Stainless Steels by Electrochemical-Impedance Spectroscopy." *Oxidation of Metals*, 50(5), 431–455.
- Panicaud, B., Hmima, A., Rampelberg, C., Ngom, M., Lebel, F., Geandier, G., Maurer, T., Grosseau-Poussard, J. L., Guyot, E., Béal, J., Maraë-Djouda, J., Joncour, L. le, and Alhoussein, A. (2021). "Stress determination in a thermally grown oxide on Ni38Cr alloy by use of micro/nanogauge gratings." *Materials Science and Engineering A*, 812, 141079.
- Park, B. K., Lee, J. W., Lee, S. B., Lim, T. H., Park, S. J., Park, C. O., and Song, R. H. (2013). "Cu- and Ni-doped Mn1.5Co1.5O4 spinel coatings on metallic interconnects for solid oxide fuel cells." *Int J Hydrogen Energy*, 38(27), 12043–12050.
- Park, M., Shin, J. S., Lee, S., Kim, H. J., An, H., Ji, H. il, Kim, H., Son, J. W., Lee, J. H., Kim, B. K., Lee, H. W., and Yoon, K. J. (2018). "Thermal degradation mechanism of ferritic alloy (Crofer 22 APU)." *Corros Sci*, 134(September 2017), 17–22.
- Patil, V., Joshi, P., Chougule, M., and Sen, S. (2012). "Synthesis and Characterization of Co3O4 Thin Film." *Soft Nanoscience Letters*, 02(01), 1–7.
- Petric, A., and Ling, H. (2007). "Electrical conductivity and thermal expansion of spinels at elevated temperatures." *Journal of the American Ceramic Society*, 90(5), 1515–1520.
- Priyadharsini, R., ShyamalDas, Venkateshwarlu, M., Deenadayalan, K., and Manoharan, C. (2022). "The influence of reaction and annealing temperature on physical and magnetic properties of CuFe2O4 nanoparticles : Hydrothermal method." *Inorg Chem Commun*, 140, 109406.

Przybylski, K., Brylewski, T., Durda, E., Gawel, R., and Kruk, A. (2014). "Oxidation properties of the Crofer 22 APU steel coated with $\text{La}_{0.6}\text{Sr}_{0.4}\text{Co}_{0.2}\text{Fe}_{0.8}\text{O}_3$ for IT-SOFC interconnect applications." *J Therm Anal Calorim*, 116(2), 825–834.

Puranen, J., Lagerbom, J., Hyvärinen, L., Kylmälahti, M., Himanen, O., Pihlatie, M., Kiviaho, J., and Vuoristo, P. (2011). "The structure and properties of plasma sprayed iron oxide doped manganese cobalt oxide spinel coatings for SOFC metallic interconnectors." *Journal of Thermal Spray Technology*, 20(1–2), 154–159.

Qu, W., Jian, L., Ivey, D. G., and Hill, J. M. (2006). "Yttrium, cobalt and yttrium/cobalt oxide coatings on ferritic stainless steels for SOFC interconnects." *J Power Sources*, 157(1), 335–350.

Quadackers, W. J. (1987). "High temperature corrosion in the service environments of a nuclear process heat plant." *Materials Science and Engineering*, 87, 107–112.

Quadackers, W. J., Malkow, T., Piron Abellan, J., Flesch, U., Shemet, V., and Singheiser, L. (2000). "Suitability of Ferritic Steels for Application as Construction Materials for SOFC Interconnects."

R. Kenneth Marcus, J. A. C. B. (2002). *Glow Discharge Plasmas in Analytical Spectroscopy*. *Glow Discharge Plasmas in Analytical Spectroscopy*.

Rao, C. J., Ningshen, S., and Philip, J. (2020). "Atmospheric air oxidation of 9Cr-1Mo steel: Depth profiling of oxide layers using glow discharge optical emission spectrometry." *Spectrochim Acta Part B At Spectrosc*, 172(April), 105973.

Reena, R. S., Aslinjensipriya, A., Jose, M., and Das, S. J. (2020). "Investigation on structural, optical and electrical nature of pure and Cr-incorporated cobalt oxide nanoparticles prepared via co-precipitation method for photocatalytic activity of methylene blue dye." *Journal of Materials Science: Materials in Electronics*, 31(24), 22057–22074.

Rogers, K. D., and Daniels, P. (2002). "An X-ray diffraction study of the effects of heat treatment on bone mineral microstructure." *Biomaterials*, 23, 2577–2585.

Rueden, C. T., Schindelin, J., Hiner, M. C., DeZonia, B. E., Walter, A. E., Arena, E. T., and Eliceiri, K. W. (2017). "ImageJ2: ImageJ for the next generation of scientific image data." *BMC Bioinformatics*, 18(1).

Ruiz-Trejo, E., Atkinson, A., and Brandon, N. P. (2015). “Metallizing porous scaffolds as an alternative fabrication method for solid oxide fuel cell anodes.” *J Power Sources*, 280, 81–89.

Saeidpour, F., and Ebrahimifar, H. (2021). “Effect of nanostructure Fe-Ni-Co spinel oxides/Y₂O₃ coatings on the high-temperature oxidation behavior of Crofer 22 APU stainless steel interconnect.” *Corros Sci*, 182, 10928-.

Sakai, N., Yokokawa, H., Horita, T., and Yamaji, K. (2005). “Ceramic Product Development and Commercialization Lanthanum Chromite-Based Interconnects as Key Materials for SOFC Stack Development.” *Int. J. Appl. Ceram. Technol.*, 23(30), 1–1.

Scherzer, M., Girgsdies, F., Stotz, E., Willinger, M. G., Frei, E., Schlögl, R., Pietsch, U., and Lunkenbein, T. (2019). “Electrochemical Surface Oxidation of Copper Studied by in Situ Grazing Incidence X-ray Diffraction.” *Journal of Physical Chemistry C*, 123(21), 13253–13262.

Sekler, J., Steinmann, P. A., and Hintermann, H. E. (1988). “The scratch test: Different critical load determination techniques.” *Surf Coat Technol*, 36(1–2), 519–529.

Shaigan, N., Qu, W., Ivey, D. G., and Chen, W. (2010). “A review of recent progress in coatings, surface modifications and alloy developments for solid oxide fuel cell ferritic stainless steel interconnects.” *J Power Sources*, 195(6), 1529–1542.

Sharma, G., and Singh, K. (2019). “Agro-waste ash and mineral oxides derived glass-ceramics and their interconnect study with Crofer 22 APU for SOFC application.” *Ceram Int*, 45(16), 20501–20508.

Shen, F., and Lu, K. (2016). “Co_xFe_{1-x} oxide coatings on metallic interconnects for solid oxide fuel cells.” *J Power Sources*, 330, 231–239.

Shen, Y. J., Zhang, Y. L., Gao, F., Yang, G. S., and Lai, X. P. (2018). “Influence of temperature on the microstructure deterioration of sandstone.” *Energies (Basel)*, 11(7), 1753.

Shi, H., Tang, C., Jianu, A., Fetzer, R., Weisenburger, A., Steinbrueck, M., Grosse, M., Stieglitz, R., and Müller, G. (2020). “Oxidation behavior and microstructure evolution of alumina-forming austenitic & high entropy alloys in steam environment at 1200 °C.” *Corros Sci*, 170, 108654.

Shindo, M., Quadackers, W. J., and Schuster, H. (1986). "Corrosion behaviour of high temperature alloys in impure helium environments." *Journal of Nuclear Materials*, 140(2), 94–105.

Shong, W. J., Liu, C. K., Chen, C. Y., Peng, C. C., Tu, H. J., Fey, G. T. K., Lee, R. Y., and Kao, H. M. (2011). "Effects of lanthanum-based perovskite coatings on the formation of oxide scale for ferritic SOFC interconnect." *Mater Chem Phys*, 127(1–2), 45–50.

Simner, S. P., Bonnett, J. F., Canfield, N. L., Meinhardt, K. D., Shelton, J. P., Sprenkle, V. L., and Stevenson, J. W. (2003). "Development of lanthanum ferrite SOFC cathodes." *J Power Sources*, 113(1), 1–10.

Singhal, S. C. (2000). "Science and technology of solid-oxide fuel cells." *MRS Bull*, 25(3), 16–21.

Singheiser, L., Huczkowski, P., Markus, T., and Quadackers, W. J. (2010). "High temperature corrosion issues for metallic materials in solid oxide fuel cells." *Shreir's Corrosion*, 482–517.

Song SH, and Xiao P. (2003). "An impedance spectroscopy study of oxide films formed during high temperature oxidation of an austenitic stainless steel." *Journal of Material Science*, 38, 499–506.

Srinivasa Rao, S., Reddy Parne, S., Nagaraju, P., Satya Chidambara Swamy Vaddadi, V., Vijayakumar, Y., and Reddy Edla, D. (2022). "Synthesis and characterization of spray deposited nanostructured WO₃ thin films for ammonia sensing applications." *Inorg Chem Commun*, 144, 109892.

Srisrual, A., Coindeau, S., Galerie, A., Petit, J. P., and Wouters, Y. (2009). "Identification by photoelectrochemistry of oxide phases grown during the initial stages of thermal oxidation of AISI 441 ferritic stainless steel in air or in water vapour." *Corros Sci*, 51(3), 562–568.

Stabrawa, I., Kubala-Kukuś, A., Banaś, D., Pepponi, G., Braziewicz, J., Pajek, M., and Teodorczyk, M. (2019). "Characterization of the morphology of titanium and titanium (IV) oxide nanolayers deposited on different substrates by application of grazing incidence X-ray diffraction and X-ray reflectometry techniques." *Thin Solid Films*, 671, 103–110.

Steinmann, P. A., Tardy, Y., and Hintermann, H. E. (1987). “Adhesion testing by the scratch test method: The influence of intrinsic and extrinsic parameters on the critical load.” *Thin Solid Films*, 154(1–2), 333–349.

Stygar, M., Kurtyka, P., Brylewski, T., Tajchman, W., and Staśko, R. (2013). “Physicochemical and mechanical properties of Crofer 22 APU ferritic steel applied in SOFC.” *Metallurgy and Foundry Engineering*, 39(2), 47–58.

Sun, Z., Gopalan, S., Pal, U. B., and Basu, S. N. (2017). “Cu_{1.3}Mn_{1.7}O₄ spinel coatings deposited by electrophoretic deposition on Crofer 22 APU substrates for solid oxide fuel cell applications.” *Surf Coat Technol*, 323, 49–57.

Swaminathan, S., Mallika, C., Krishna, N. G., Thinaharan, C., Jayakumar, T., and Kamachi Mudali, U. (2014). “Evolution of surface chemistry and morphology of oxide scale formed during initial stage oxidation of modified 9Cr-1Mo steel.” *Corros Sci*, 79, 59–68.

Takeda, Y., Shoji, T., Bojinov, M., Kinnunen, P., and Saario, T. (2006). “In situ and ex situ characterisation of oxide films formed on strained stainless steel surfaces in high-temperature water.” *Appl Surf Sci*, 252(24), 8580–8588.

Talic, B., Falk-Windisch, H., Venkatachalam, V., Hendriksen, P. V., Wiik, K., and Lein, H. L. (2017a). “Effect of coating density on oxidation resistance and Cr vaporization from solid oxide fuel cell interconnects.” *J Power Sources*, 354, 57–67.

Talic, B., Hendriksen, P. V., Wiik, K., and Lein, H. L. (2018). “Thermal expansion and electrical conductivity of Fe and Cu doped MnCo₂O₄ spinel.” *Solid State Ion*, 326, 90–99.

Talic, B., Molin, S., Wiik, K., Hendriksen, P. V., and Lein, H. L. (2017b). “Comparison of iron and copper doped manganese cobalt spinel oxides as protective coatings for solid oxide fuel cell interconnects.” *J Power Sources*, 372(November), 145–156.

Tao, S., Yang, J., Shao, F., Zhao, H., Zhong, X., Zhuang, Y., Sheng, J., Ni, J., Li, Q., and Tao, S. (2022). “Atmospheric plasma sprayed thick thermal barrier coatings: Microstructure, thermal shock behaviors and failure mechanism.” *Eng Fail Anal*, 131, 105819.

Tao, S., Yang, J., Zhai, M., Shao, F., Zhong, X., Zhao, H., Zhuang, Y., Ni, J., Li, W., and Tao, S. (2020). “Thermal stability of YSZ thick thermal barrier coatings deposited by suspension and atmospheric plasma spraying.” *Crystals (Basel)*, 10(11), 1–13.

Tiegel, M., Hosseinabadi, R., Kuhn, S., Herrmann, A., and Rüssel, C. (2015). “Young’s modulus, Vickers hardness and indentation fracture toughness of alumino silicate glasses.” *Ceram Int*, 41(6), 7267–7275.

Tomastik, J., Ctvrtlik, R., Bohac, P., Drab, M., Koula, V., Cvrk, K., and Jastrabik, L. (2015). “Utilization of acoustic emission in scratch test evaluation.” *Key Eng Mater*, 662(September), 119–122.

Vaßen, R., Grünwald, N., Marcano, D., Menzler, N. H., Mücke, R., Sebold, D., Sohn, Y. J., and Guillon, O. (2016). “Aging of atmospherically plasma sprayed chromium evaporation barriers.” *Surf Coat Technol*, 291, 115–122.

Velraj, S., Zhu, J. H., Painter, A. S., Du, S. W., and Li, Y. T. (2014). “Impedance spectroscopy of the oxide films formed during high temperature oxidation of a cobalt-plated ferritic alloy.” *J Power Sources*, 247, 314–321.

Vencl, A., Arostegui, S., Favaro, G., Zivic, F., Mrdak, M., Mitrović, S., and Popovic, V. (2011). “Evaluation of adhesion/cohesion bond strength of the thick plasma spray coatings by scratch testing on coatings cross-sections.” *Tribol Int*, 44(11), 1281–1288.

Waluyo, N. S., Park, S. S., Song, R. H., Lee, S. B., Lim, T. H., Hong, J. E., Ryu, K. H., Im, W. Bin, and Lee, J. W. (2018). “Protective coating based on manganese–copper oxide for solid oxide fuel cell interconnects: Plasma spray coating and performance evaluation.” *Ceram Int*, 44(10), 11576–11581.

Wang, K., Liu, Y., and Fergus, J. W. (2011a). “Interactions between SOFC interconnect coating materials and chromia.” *Journal of the American Ceramic Society*, 94(12), 4490–4495.

Wang, K., Liu, Y., and Fergus, J. W. (2011b). “Interactions between SOFC interconnect coating materials and chromia.” *Journal of the American Ceramic Society*, 94(12), 4490–4495.

Wang, Y., Wei, X., Hu, X., Zhou, W., and Zhao, Y. (2019). “Effect of Formic Acid Treatment on the Structure and Catalytic Activity of Co₃O₄ for N₂O Decomposition.” *Catal Letters*, 149(4), 1026–1036.

Wei, L., Zheng, J., Chen, L., and Misra, R. D. K. (2018). “High temperature oxidation behavior of ferritic stainless steel containing W and Ce.” *Corros Sci*, 142(May), 79–92.

- Wild, R. K. (1977). "High Temperature oxidation of Austenitic stainless steel in low oxygen pressure." *Corros Sci*, 17(2), 87–93.
- Wu, J., and Liu, X. (2010). "Recent development of SOFC metallic interconnect." *J Mater Sci Technol*, 26(4), 293–305.
- Xiao, J., Zhang, W., Xiong, C., Chi, B., Pu, J., and Jian, L. (2016). "Oxidation behavior of Cu-doped MnCo₂O₄ spinel coating on ferritic stainless steels for solid oxide fuel cell interconnects." *Int J Hydrogen Energy*, 41(22), 9611–9618.
- Xie, Y., and Hawthorne, H. M. (1999). "The damage mechanisms of several plasma-sprayed ceramic coatings in controlled scratching." *Wear*, 233–235, 293–305.
- Xu, H., and Zeng, H. C. (2004). "Self-generation of tiered surfactant superstructures for one-pot synthesis of Co₃O₄ nanocubes and their close-and non-close-packed organizations." *Langmuir*, 20(22), 9780–9790.
- Xu, Y., Wen, Z., Wang, S., and Wen, T. (2011). "Cu doped Mn-Co spinel protective coating on ferritic stainless steels for SOFC interconnect applications." *Solid State Ion*, 192(1), 561–564.
- Yamamoto, O. (2000). "Solid oxide fuel cells: Fundamental aspects and prospects." *Electrochim Acta*, 45(15–16), 2423–2435.
- Yang, Z., Guo, M., Wang, N., Ma, C., Wang, J., and Han, M. (2017). "A short review of cathode poisoning and corrosion in solid oxide fuel cell." *Int J Hydrogen Energy*, 42(39), 24948–24959.
- Yang, Z., Hardy, J. S., Walker, M. S., Xia, G., Simner, S. P., and Stevenson, J. W. (2004). "Structure and Conductivity of Thermally Grown Scales on Ferritic Fe-Cr-Mn Steel for SOFC Interconnect Applications." *J Electrochem Soc*, 151(11), A1825.
- Yang, Z., Xia, G. G., Li, X. H., and Stevenson, J. W. (2007). "(Mn,Co)₃O₄ spinel coatings on ferritic stainless steels for SOFC interconnect applications." *Int J Hydrogen Energy*, 32(16), 3648–3654.
- Yang, Z., Xia, G., Simner, S. P., and Stevenson, J. W. (2005). "Thermal Growth and Performance of Manganese Cobaltite Spinel Protection Layers on Ferritic Stainless Steel SOFC Interconnects." *J Electrochem Soc*, 152(9), A1896.

Young, D. J. (2016). “High Temperature Oxidation and Corrosion of Metals: Second Edition.” *High Temperature Oxidation and Corrosion of Metals: Second Edition*, 1–733.

Young, D. J., Zurek, J., Singheiser, L., and Quadakkers, W. J. (2011). “Temperature dependence of oxide scale formation on high-Cr ferritic steels in Ar–H₂–H₂O.” *Corros Sci*, 53(6), 2131–2141.

Zhang, H. H., and Zeng, C. L. (2014). “Preparation and performances of Co-Mn spinel coating on a ferritic stainless steel interconnect material for solid oxide fuel cell application.” *J Power Sources*, 252, 122–129.

Zhang, Y., Javed, A., Zhou, M., Liang, S., and Xiao, P. (2014). “Fabrication of Mn-Co spinel coatings on Crofer 22 APU stainless steel by electrophoretic deposition for interconnect applications in solid oxide fuel cells.” *Int J Appl Ceram Technol*, 11(2), 332–341.

Zhao, M., Geng, S., Chen, G., and Wang, F. (2020). “Thermal conversion and evolution behavior of surface scale on SOFC interconnect steel with sputtered FeCoNi coating.” *Corros Sci*, 168, 108561.

Zhu, B., and Lindbergh, G. (2001). “Corrosion behaviour of high-chromium ferritic steels in molten carbonate in cathode environment.” *Electrochim Acta*, 46(17), 2593–2604.

Zhu, W. Z., and Deevi, S. C. (2003). *Development of interconnect materials for solid oxide fuel cells. Materials Science and Engineering A*, 227–243.

Zhuyikov, S. (2018). “Nanostructured Semiconductor Composites for Solid Oxide Fuel Cells (SOFCs).” *Nanostructured Semiconductors*, Elsevier, 413–474.

List of Publications:

Accepted Publications:

1. Surface characterization of $Mn_{1.0}Co_{1.9}Fe_{0.1}O_4$ (MCF) spinel coating on metallic interconnect used in Solid Oxide Fuel Cells, published in Springer Series: Proceedings of Fifth International Conference on Inventive Material Science Applications, Scopus Indexed, doi:[10.1007/978-981-19-4304-1_25](https://doi.org/10.1007/978-981-19-4304-1_25)
2. Characterization of plasma sprayed $Mn_{1.0}Co_{1.9}Fe_{0.1}O_4$ coating on Crofer 22 APU ferritic stainless steel used for solid oxide fuel cell interconnect, Transactions of Indian Institute of Metals, Accepted, TIIM-D-22-01269R1, SCI Indexed, doi:[10.1007/s12666-022-02844-7](https://doi.org/10.1007/s12666-022-02844-7)
3. Thermal expansion of Crofer 22 APU steel used for SOFC interconnect using in-situ high temperature X-ray diffraction, 3rd Indo-Japan Bilateral Symposium on the Futuristic Materials and Manufacturing on Sustainable Development Goals – 2022, IIT Madras. Abstract accepted and published in ‘Book of Abstracts’. Published in Materials Today: Proceedings, doi:[10.1016/j.matpr.2023.03.113](https://doi.org/10.1016/j.matpr.2023.03.113).

Publications under review:

1. Understanding Interface Adhesion of Atmospheric Plasma Sprayed $Mn_{1.0}Co_{1.9}Fe_{0.1}O_4$ Coating on SOFC Metallic Interconnect using Correlative Scratch Indentation Test, Journal of Thermal Spray Technology.
2. Understanding early stage oxidation mechanism of Crofer 22 APU SOFC steel interconnect using GD-OES and GIXRD, Thin Solid Films.
3. The effect of strain induced phase transformation on the thermal expansion compatibility of plasma sprayed spinel coating on SOFC metallic interconnect – A study using in-situ high temperature X-ray Diffraction, International Journal of Hydrogen Energy.
4. Long term oxidation of plasma sprayed $Mn_{1.0}Co_{1.9}Fe_{0.1}O_4$ protective coating on Crofer 22 APU SOFC interconnect, Journal of European Ceramic Society.

CURRICULUM VITAE

Name : Manjunath

Father's name : Ananda Naik H

Date of birth : 09 Nov. 1991

Permanent Address : 304, Parjanya, Tellar Road, Karkala, Udupi District,
Karnataka, India.

Mobile : +91-8123585025

E-mail : manjunathnk91@gmail.com

Academic qualification:

Bachelor of Engineering (B.E.) in Mechanical Engineering from Alva's Institute of Engineering and Technology, Moodbidri (62.7 % out of 100 %)

Master of Technology (M.Tech.) in Materials Engineering from National Institute of Technology Karnataka, Surathkal (CGPA: 6.19 out of 10)